

Ab Initio and Finite Element Simulations of Material Properties in Multiphase Ceramics

Dissertation zur Erlangung
des naturwissenschaftlichen Doktorgrades
der Bayrischen Julius-Maximilians-Universität Würzburg

vorgelegt von
Maria Iuga

Würzburg 2007

Eingereicht am

bei der Fakultät für Chemie und Pharmazie

1. Gutachter:

2. Gutachter:

der Dissertation

1. Prüfer:

2. Prüfer:

des öffentlichen Promotionskolloquiums

Tag des öffentlichen Promotionskolloquiums:.....

Doktorurkunde ausgehändigt am:

Abstract

In the present study numerical methods are employed within the framework of multiscale modeling. Quantum mechanics and finite element method simulations have been used in order to calculate thermoelastic properties of ceramics. At the atomic scale, elastic constants of ten different ceramics (Al_2O_3 , α - and β -SiC, TiO₂-rutile and anatase, AlN, BN, CaF₂, TiB₂, ZrO₂) were calculated from the first principles (ab-initio) using the density functional theory with the general gradient approximation. The simulated elastic moduli were compared with measured values. These results have shown that the ab-initio computations can be used independently from experiment to predict elastic behavior and can provide a basis for the modeling of structural and elastic properties of more complex composite ceramics.

In order to simulate macroscopic material properties of composite ceramics from the material properties of the constituting phases, 3D finite element models were used. The influence of microstructural features such as pores and grain boundaries on the effective thermoelastic properties is studied through a diversity of geometries like truncated spheres in cubic and random arrangement, modified Voronoi polyhedra, etc. A 3D model is used for modeling the microstructure of the ceramic samples. The measured parameters, like volume fractions of the two phases, grain size ratios and grain boundary areas are calculated for each structure. The theoretical model is then varied to fit the geometrical data derived from experimental samples.

The model considerations are illustrated on two types of bi-continuous materials, a porous ceramic, alumina (Al_2O_3) and a dense ceramic, zirconia-alumina composite (ZA). For the present study, alumina samples partially sintered at temperatures between 800 and 1320°C, with fractional densities between 58.4% and 97% have been used. For ZA ceramic the zirconia powder was partially stabilized and the ratio between alumina and zirconia was varied. For these two examples of ceramics, Young's modulus and thermal conductivity were calculated and compared to experimental data of samples of the respective microstructure.

Comparing the experimental and simulated values of Young's modulus for Al_2O_3 ceramic a good agreement was obtained. For the thermal conductivity the consideration of thermal boundary resistance (TBR) was necessary. It was shown that for different values of TBR the experimental data lie within the simulated thermal conductivities. In the case of ZA ceramic also a good agreement between simulated and experimental values was observed. For smaller ZrO₂ fractions, a larger Young's modulus and thermal conductivity was observed in the experimental samples. The discrepancies have been discussed by taking into account the effect of pressure. Considering the dependence of the thermoelastic properties on the pressure, it has been shown that the thermal stresses resulting from the cooling process were insufficient to explain the discrepancies between experimental and simulated thermoelastic properties.

Zusammenfassung

In der vorliegenden Arbeit wurden im Rahmen einer Multiskalen-Modellierung quantenmechanische und Finite-Elemente-Simulationen verwendet, um thermoelastische Eigenschaften keramischer Materialien zu untersuchen. Auf atomarer Skala wurden die elastischen Konstanten von zehn unterschiedlichen Keramiken berechnet: Al_2O_3 , α - und β -SiC, TiO_2 -Rutil und Anatas, AlN, BN, CaF_2 , TiB_2 , ZrO_2 , wobei die Dichtefunktionaltheorie mit der verallgemeinerten Gradientennäherung verwendet wurde. Die simulierten elastischen Konstanten wurden mit gemessenen Werten verglichen. Diese Ergebnisse haben gezeigt, dass die quantenmechanischen Berechnungen unabhängig vom Experiment verwendet werden können, um elastisches Verhalten vorauszusagen. Außerdem stehen sie als Grundlage für das Modellieren der strukturellen und elastischen Eigenschaften der komplexeren keramischen Kompositen zur Verfügung.

Um makroskopische Eigenschaften keramischer Komposite aus den Eigenschaften der beteiligten Phasen zu simulieren, wurden 3D Finite Elemente Modelle benutzt. Der Einfluss von Mikrostrukturmerkmalen, wie Poren und Korngrenzen, auf die thermoelastischen Eigenschaften wurde in verschiedenen Geometrien wie z.B. abgeschnittene Kugeln in kubischer und zufälliger Anordnung oder Voronoi-Polyeder studiert. 3D-Modelle wurden auch für das Modellieren der Mikrostruktur experimenteller Proben benutzt. Parameter, wie der Volumenanteil der beteiligten Phasen, die Korngrößenverhältnisse und die Korngrenzflächenanteile wurden für jede Struktur gemessen. Das theoretische Strukturmodell wurde dann variiert, um es an die geometrischen Daten der experimentellen Proben anzupassen.

Das Modell wurde an zwei Materialtypen, einer porösen Keramik, Aluminiumoxid (Al_2O_3) und einer dichten Keramik, einem Komposit aus Aluminiumoxid und Zirkonoxid (ZA) angewendet. Für die vorliegende Arbeit wurden die Al_2O_3 Proben teilgesintert, bei Temperaturen zwischen 800 und 1320°C, mit Dichten zwischen 58.4% und 97%. Für die ZA Keramik wurde das ZrO_2 Pulver partiell stabilisiert und das Verhältnis zwischen Al_2O_3 und ZrO_2 verändert. Für diese zwei Keramiken wurden der Young Modul und die Wärmeleitfähigkeit errechnet und mit den experimentellen Daten verglichen.

Der Young Modul der Al_2O_3 Keramik zeigte eine gute Übereinstimmung zwischen experimentellen und simulierten Werten. Für die Wärmeleitfähigkeit wurde die Berücksichtigung des Wärmewiderstands an Korngrenzen notwendig. Es zeigte sich, dass die experimentellen Daten für den Wärmewiderstand mit dem simulierten Wert kompatibel sind. Im Fall der ZA-Keramik wurde bei höheren ZrO_2 -Volumenanteilen ebenfalls eine gute Übereinstimmung zwischen simulierten und experimentellen Werten des Young-Moduls und der Wärmeleitfähigkeit beobachtet. Bei kleineren ZrO_2 -Volumenanteilen wurden jedoch ein größerer Young-Modul und eine größere Wärmeleitfähigkeit in den experimentellen Proben beobachtet. Um diese Unterschiede zu erklären, wurde der Einfluss des Drucks auf die thermoelastischen Eigenschaften berechnet. Es wurde gezeigt, dass die thermischen Spannungen, die aus dem Abkühlungsprozess resultieren, nicht ausreichen, um die Unterschiede zwischen experimentellen und simulierten Eigenschaften zu erklären.

Contents

1	Introduction	1
1.1	Motivation	1
1.2	Outline	4
2	Theory	7
2.1	Thermoelastic properties of solids	7
2.1.1	Elastic properties	7
2.1.2	Thermal properties	11
2.1.3	Thermoelastic properties at atomic scale	11
2.2	QM simulations of material properties	14
2.2.1	Density functional theory (DFT)	14
2.3	Finite Element Method (FEM)	18
3	Numerical methods	21
3.1	Simulation of material properties using QM	21
3.1.1	Crystal structure of investigated materials	22
3.1.2	Convergence of simulations	24
3.2	Simulation of material properties using FEM	28
3.2.1	Theoretical microstructures	28
3.2.2	Finite element mesh and boundary conditions	35
3.2.3	Convergence and verification	37
3.3	Experimental procedure	39
3.3.1	Quantitative image analysis	39
3.3.2	Sample preparation	40
3.3.3	Experimental measurements of thermoelastic properties	45
4	Results and discussions	47
4.1	Quantum mechanics (QM) simulations	47
4.1.1	Equation of state	47
4.1.2	Elastic constants	47
4.2	Finite element simulations	52
4.2.1	Microstructure-property relations in synthetic structures	52
4.2.2	Microstructure-property relations in real structures	61
A	Stress calculation on a 3D element	75

Bibliography

80

List of symbols

Small letters

a	edge of the unit cell
a_c	total neck area
a_i	total pore-solid interface area
a_s	ratio of total contact area to total interface area
b	edge lengths at contact area
c	light velocity
c_a	auto-correlation parameter
c_i	chord lengths of particles
c'_i	component i of center of unit cell
c_{ij}	elastic constants
c_P	specific heat capacity at constant pressure
c_s^2	average squared solid chord length
d	interatomic distance
d_{shift}	displacement of particles (spheres)
f_E	Eulerian finite strain parameter
f_s	solid volume fraction
f_σ	stress concentration factor
g	Bridgeman parameter
h	height of the truncated pyramid
h_P	Planck's constant
k	wave vector
k_B	Boltzmann's constant
m	integer number
r	neck radius
r_i	coordinate of electron i
r'_i	component i of initial center position of particle
s_{ij}	elastic compliance constants
u_i	displacement vector
$u_i(r)$	periodic part of cell
v	sound velocity
v_i	volume of element i
v_P	longitudinal (compressional) sound wave velocity
v_S	transversal (shear) sound wave velocity

Capital letters

B	bulk modulus
B'	pressure derivative of bulk modulus
B_A	boundary area
C_V	specific heat capacity at constant volume
E	Young's modulus
E_s	scaled Young's modulus
E_{min}	minimum of energy
$E[\rho]$	universal functional of energy
$E_{xc}[\rho]$	exchange-correlation functional
G	shear modulus
\hat{H}	Hamiltonian operator
K	reciprocal lattice vector
L	lattice vector of crystal
L_L	lineal fraction
N_A	Avogadro's number
N_{P_o}	number of point interceptions of an object
N_P	total number of point interceptions on a test line
P	pressure
Q	heat flux
R	molar gas constant
R_c	cutoff radius
R_α	position of nucleus
S	quantity
T	temperature
\hat{T}	kinetic energy operator
$T[\rho]$	kinetic energy functional
$T_s[\rho]$	kinetic energy functional of non-interacting electrons
U	potential energy
U_{anh}	anharmonic potential energy
U_{eq}	equilibrium potential energy
U_{har}	harmonic potential energy
V	volume
\hat{V}_{ee}	electron-electron interaction operator
$V_{ee}[\rho]$	electron-electron interaction functional
\hat{V}_{ext}	operator of interaction with external potential
$V_{ext}[\rho]$	functional of interaction with external potential
$V_H[\rho]$	classical Coulomb interaction functional
Z_α	charge of nucleus

Greeks symbols

α	coefficient of thermal expansion
δ	small variations
δ_{ij}	Kronecker symbol
ϵ	strain
ϵ_i	eigenvalues of energy
$\epsilon_{ij}, \epsilon_j$	strain tensor
$\epsilon_{xc}(\rho)$	exchange and correlation energy density
ϵ_{xx}	small deformation in x direction
ϵ_{yy}	small deformation in y direction
ϵ_{zz}	small deformation in z direction
γ	Grüneisen parameter
ℓ	mean free path of phonons
λ	thermal conductivity
λ_s	scaled thermal conductivity
λ'	wavelength associated with the phonon
λ_{ij}	components of thermal conductivity tensor
λ_L	first Lamè constant
μ_{ch}	electronic chemical potential
μ_L	second Lamè constant
ν	Poisson' s ratio
ν_s	scaled Poisson' s ratio
$\nu_{xc}(\rho)$	functional derivative of the exchange correlation energy
ω_{max}	maximal vibrational frequency
π	constant
∂	partial derivative
φ	shear angle
ρ	density
$\rho(r)$	electron density
σ	stress
σ_{ij}, σ_i	stress tensor
σ_{1max}	maximum principal tensile stress
σ_p	thermal expansion mismatch stress
θ	opening angle between two truncated pyramids based on the sides of a cube
θ_D	Debye temperature
τ	shear stress
∇	gradient operator
Δ_c	cubic dilatation
$\Delta\epsilon_L$	longitudinal strain
$\Delta\epsilon_T$	transversal strain
ΔV	volume change
Ψ_i	wave function of electron i
Ψ_{pseudo}	pseudopotential wave function
χ	thermal diffusivity

Abbreviations

sc	simple cubic
bcc	body centered cubic
fcc	face centered cubic
CASTEP	Cambridge Serial Total Energy Package
CPU	Central Processing Unit
DOF	Degrees of Freedom
DFT	Density Functional Theory
EOS	Equation of State
FEM	Finite Element Method
GGA	General Gradient Approximation
GR	Grid Refinement
LDA	Local Density Approximation
MSA	Minimum Solid Area
NC	Norm-Conserving
PS	Pseudopotential
QM	Quantum Mechanics
RVE	Representative Volume Element
SEM	Scanning Electron Micrograph
TBR	Thermal Boundary Resistance
US	Ultrasoft
XRD	X-Ray Diffraction
ZA	Zirconia-Alumina

Constants:

$$k_B = 1.3806503 \times 10^{-23} \text{ m}^2 \text{ kg s}^2 \text{ K}^{-1}$$

$$h_P = 6.626068 \times 10^{-34} \text{ m}^2 \text{ kg s}^{-1}$$

$$N_A = 6.022 \times 10^{23}$$

$$\pi = 3.14159265$$

$$R = 8.314472 \text{ J K}^{-1} \text{ mol}^{-1}$$

Chapter 1

Introduction

1.1 Motivation

As a result of their brittleness and difficulty of manufacturing, ceramic materials were useful for millennia only in the making of pottery and other artworks. However, the demand for microelectronics and structural composite components have created a high request for ceramics. Modern ceramics offer a wide range of mechanical, thermal and chemical properties with applications from combustion engines to artificial teeth. Further progress has followed as the behavior of ceramics was better understood. Physical mechanisms which govern the behavior of these materials can be better understood with the aid of computational modeling. Once having gained such knowledge it can be utilized for design of materials and improvement of properties.

Generally, the microstructure of a ceramic is characterized by grains, grains boundaries, pores and glass phases. In order to simulate the material properties, it is therefore necessary to construct a representative geometry - a representative volume element (RVE) - that incorporates overall features of the real structures, like volume fraction of different phases, interfaces between different phases, etc. For the accuracy of the results, validation of the models is an important issue in material modeling. The predictive capabilities of the model should be validated by recourse to other simulation approaches and/or by recourse to experimental data. Here it is worth mentioning that experimental characterization often yields an incomplete picture of the material's behavior. If the agreement between experiment and predictions is not satisfactory, identification of the causes is of high interest.

The present thesis is devoted to computational simulations of ceramics. The modeling of the entire behavior is far beyond the scope of this work, which would require the treatment of a huge number of different properties, mechanisms and phenomena. Considerations are focused on the thermoelastic behavior as response to mechanical and temperature loading. Numerical methods are employed within the framework of *multiscale* modeling. In multiscale modeling, the goal is to predict the performance and behavior of complex materials across relevant length and time scales, starting from fundamental physical principles and experimental data. At the *atomistic scale* (nanometer), electrons govern the interactions of atoms in a solid, and therefore a precise quantum

mechanical description is required to characterize the collective behavior of atoms in a material. However, at the engineering scale, forces arising from macroscopic stresses and temperature gradients may be the controlling elements of materials performance. At intermediate scales, defects such as dislocations, grain boundaries etc. control mechanical and thermal behavior on the *microscale* (tens of micrometers), while large collections of such defects, grain boundaries and other microstructural elements, like grains govern *mesoscopic* properties (hundreds of micrometers). The net outcome of these interactions is often in the form of a constitutive law that ultimately governs continuum behavior on the *macroscale* (centimeters).

For the present study quantum mechanics and finite element method simulations have been employed in order to calculate thermoelastic properties of materials. At the atomic scale, elastic constants of different ceramics were calculated from the first principles. These results could be used further as input properties for finite element simulations of microstructure properties at the mesoscale. For purposes of computation, some models of microstructures must be assumed. At the microscale the thermal resistance at grain boundaries was derived. Fig. 1.1 summarizes the different scales and indicates the domain to which they apply.

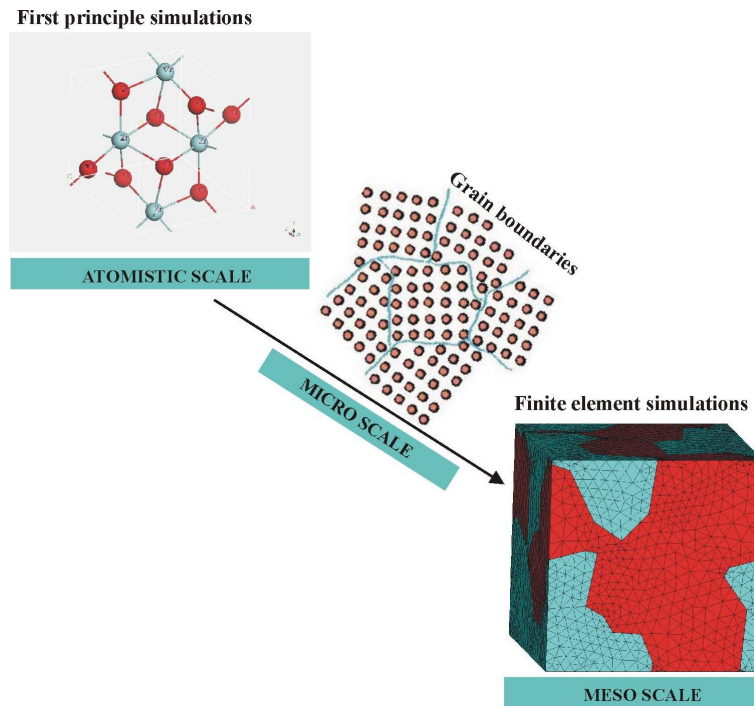


Figure 1.1: Modeling of materials at different scales

Atomistic simulations. Ab-initio quantum mechanical (QM) calculations take into account the electronic structure by solving, at some level of approximation, the Schrödinger equation [Sch26]. Despite the remarkable array of techniques available, calculations are typically performed within two computational frameworks. Hartree-Fock theory [Har28], [Foc30], [Sla51] is the older of the two, and describes the system in

terms of atomic orbitals, with the many-body wave function approximated as the product of one-electron wave functions. The second approach is based on Density Functional Theory (DFT) usually within either the Local Density Approximation (LDA) [Hed71], [Cep80] or Generalized Gradient Approximation (GGA) [Per92], [Per96] in which the energy of the system is a function of its total electron density. DFT is computationally easier to apply to solid state systems, and so it has become increasingly important in the study of ceramics over the last years. This method was developed by W. Kohn and co-workers [Hoh64], [Koh65]. For this work W. Kohn has received the Nobel prize for Chemistry in 1998. Several academic and commercial software packages are available for performing QM calculations, some of the better known being CRYSTAL, GAUSSIAN, CASTEP, WIEN2k. These methods have the disadvantage that they are computationally expensive; even with modern computers, calculations are confined to at most a hundred or so atoms. Since many ceramic phases have large unit cells, this places limits on the range of structures and phenomena to which these methods can be usefully applied. Nevertheless, these methods are vital for the accurate determination of the fundamental physics and chemistry of ceramics, and are used to solve problems where knowledge of electronic structure is important.

Mesoscale simulations. Most ceramics are used in polycrystalline form, and it has long been recognized that the microstructure of ceramics has a profound influence on their properties. A major goal of current research is therefore the development of simulation methods that can reliably reproduce the time-evolution of microstructures. Many processes, such as those involved in the formation and use of ceramic components, have been successfully modeled using Finite Element Methods (FEM). This is one of the earliest techniques applied to materials modeling, and is used throughout industry today. Many powerful commercial software packages are available for calculating 2D and 3D thermomechanical, electromechanical and optical processes, like ANSYS, FLUENT, ABAQUS, etc. FEM is the simulation method closest to real ceramic applications and usually relies on a large database of measured materials properties as input. In this respect, first principles calculations provide the ideal complement to experiments, as calculations can supply critical information which may be difficult to measure experimentally.

Thermal and mechanical properties such as thermal conductivity, elastic moduli, thermal expansion and thermal stresses are basic properties, which are crucial in development of ceramics. Some thermoelastic properties, like density, heat capacity or coefficient of thermal expansion, in porous or two phase materials are simply determined by a rule of mixtures [Has62]. However, thermal conductivity and elastic coefficients are strongly related to microstructure and therefore, when predicting the thermoelastic properties of materials, one should take into account the microstructure resulting from the manufacturing of ceramics. To estimate the effective material properties of porous and bi-continuous ceramics many analytical methods have been developed over the years. Most of them are essential variants of the composite cylinder model [Has62a] or self-consistent models [Hil63], [Mil88]. Many studies have investigated the relation between total pore volume and thermoelastic properties of porous compacts [Mar71], [Muk98], [Kov01], [Mun01], [Jef02], [Pab03]. In the last decades theories of effective media, which sufficiently describe microstructures with inclusions or closed pores have

been widely used [Dea83], [Boc93], [Chu96], [Boc97], [Pet02]. If the pore fraction is small, the composite properties can be calculated with high accuracy for ellipsoidal pores [Ond74]. Another class of studies have concentrated on derivation of different bounds. Variational principles have been used to obtain rigorous upper and lower bounds for the properties of composites with given properties of the participating phases [Has63], [Hal76], [Tor91]. The analytical models represent two-phase or multiphase materials only approximately, as they ignore specific details of the microstructure. To overcome this serious problem, numerical methods were developed using the increasing computer power, like random walk [Tob90], [Rae98], finite difference methods [Hah96] and finite element methods. FEM are easily available and can be used for the calculation of thermal as well as mechanical properties [Ram93], [Bis97], [Gou00], [Gus00], [Gus01], [Rob00], [Bir01], [Kar01], [Par01], [She01], [Jef02], [Rob02]. Although two-dimensional models are still used, many topological features, e.g. particle connectivity, cannot be adequately described in two dimensions and generally 3-D models are preferred. There are two types of 3-D models: periodic lattices and random structures. The periodic lattices are calculated with spherical particles or pores in a simple cubic (sc), body centered cubic (bcc) or face centered cubic (fcc) arrangement [Jef02]. Sintering necks are simulated using truncated spheres [Jef02] or sometimes overlapping cylinders [Sch98]. Random microstructures are produced in different ways. Often ellipsoidal particles or pores with randomly chosen centers and more or less overlap are generated [Jef02], [Rob02]. The random structures have the advantage that resemble much more the real microstructures.

The disadvantage of both types of geometric models is that fundamental phenomena cannot be described using simple particle shapes. Therefore, in this study, other particle shapes like truncated octahedron, overlapping spheres and cylinders, truncated square pyramids, Voronoi polyhedra, etc. were considered. Their influence on the thermal and elastic properties was investigated. The arrangement of the particles within a 3D unit cell plays also an important role as described in this study. In order to validate the models and for an improved understanding of the ceramic's mechanical and thermal properties, some real systems were investigated: a porous alumina (Al_2O_3) and a zirconia-alumina composite ($\text{Al}_2\text{O}_3\text{-ZrO}_2$) ceramic.

1.2 Outline

This thesis is focused on simulations of thermal and elastic properties of different materials using two approaches: quantum mechanics and finite element based method. Therefore the outline of the thesis is as follows:

Chapter 2 presents the **theory** and starts with a summary about the basics of the elastic and thermal properties of solids. Some thermoelastic properties, like elastic constants and thermal conductivity are described at the macroscopic as well as the atomistic scale. The theoretical background concerning the two approaches, ab-initio (first principles) and finite element methods, are presented in the next subchapters.

Chapter 3, which refers to the **methods** developed in order to perform the simulations, is divided in three parts. The first part contains the method applied in the

quantum mechanical calculations. Convergence studies are also included. The second part describes the method used to perform FEM calculations. Theoretical microstructures used in FE analysis together with the convergence and validation of simulations are presented here. The last part contains experimental details. Microstructure of the ceramic samples as well as measurements of their thermal and mechanical properties are presented. Some basics of quantitative image analysis used to investigate the real microstructures are also given.

Chapter 4 titled **results and discussions** illustrates the results of the simulations by applying the two approaches (ab-initio and FEM) to various ceramics. First, the results of QM simulations for ten ceramic systems (Al_2O_3 , α - and β -SiC, TiO_2 rutile and anatase, AlN, BN, TiB_2 , CaF_2 and ZrO_2) are presented and discussed. In the following FEM simulations results concerning the theoretical and real microstructures are outlined. In every subchapter conclusions concerning the results of QM and FEM simulations were drawn.

Chapter 2

Theory

2.1 Thermoelastic properties of solids

2.1.1 Elastic properties

The elasticity of materials is important for the understanding of processes, ranging from brittle failure to the propagation of elastic waves. The elastic constants of solids provide information about the bonding characteristic between the atoms, the anisotropic character of the bonding and structural stability.

The elastic constants relate an applied external force described by the stress tensor to the resulting deformation described by the strain tensor. Assuming that a crystal is a homogeneous, anisotropic medium and that stress and strain are homogeneous, the Hook's approximation states that the strain, ϵ_{kl} is proportional to the applied stress, σ_{ij} and depends on the material properties, described by the constants of elasticity, c_{ijkl} :

$$\sigma_{ij} = c_{ijkl}\epsilon_{kl}. \quad (2.1)$$

Here the four rank tensor of elasticity c_{ijkl} consists of 81 components. The three dimensional stress and strain tensors, σ_{ij} and ϵ_{kl} are defined as:

$$\sigma_{ij} = \begin{bmatrix} \sigma_{11} & \tau_{12} & \tau_{13} \\ \tau_{21} & \sigma_{22} & \tau_{23} \\ \tau_{31} & \tau_{32} & \sigma_{33} \end{bmatrix} \quad (2.2)$$

and

$$\epsilon_{kl} = \begin{bmatrix} \epsilon_{11} & \gamma_{12} & \gamma_{13} \\ \gamma_{21} & \epsilon_{22} & \gamma_{23} \\ \gamma_{31} & \gamma_{32} & \epsilon_{33} \end{bmatrix} \quad (2.3)$$

where σ_{11} , σ_{22} , σ_{33} are tensile (or compressional) stresses in x , y and z direction respectively. The other components of the stress tensor are shear stresses. ϵ_{11} , ϵ_{22} , ϵ_{33} represents the strain in x , y and z directions respectively. Like in case of stress tensor, the other components of the strain tensor are shear strains.

To calculate the principal stresses σ_1 , σ_2 and σ_3 the three invariants of stress tensor must be calculated:

$$\begin{aligned} I_1 &= \sigma_{11} + \sigma_{22} + \sigma_{33} \\ I_2 &= \sigma_{11}\sigma_{22} + \sigma_{22}\sigma_{33} + \sigma_{33}\sigma_{11} - \tau_{12}^2 - \tau_{23}^2 - \tau_{13}^2 \\ I_3 &= \sigma_{11}\sigma_{22}\sigma_{33} + 2\tau_{12}\tau_{23}\tau_{13} - \sigma_{11}\tau_{23}^2 - \sigma_{22}\tau_{13}^2 - \sigma_{33}\tau_{12}^2 \end{aligned} \quad (2.4)$$

Then the characteristic equation of 3D principal stresses is expressed as:

$$\sigma^3 - I_1\sigma^2 + I_2\sigma - I_3 = 0 \quad (2.5)$$

The three roots of this equation are principal stresses σ_1 , σ_2 and σ_3 .

In the case of a solid, the hydrostatic (or isostatic) pressure P is defined as one third of the trace of the stress tensor, i.e. the mean of the diagonal terms:

$$P = \frac{\text{Tr}(\sigma_{ij})}{3} = \frac{\sigma_{11} + \sigma_{22} + \sigma_{33}}{3} \quad (2.6)$$

Because of the symmetry of both the stress and strain tensor (6 independent components each) and due to the reversibility of elastic deformation the numbers reduce to 21 independent components. Voigt introduced a simplification notation known as Voigt notation. The pairs of indices are replaced by a single index according to the matrix scheme,

$$\begin{pmatrix} 11 & 12 & 13 \\ 21 & 22 & 23 \\ 31 & 32 & 33 \end{pmatrix} \rightarrow \begin{pmatrix} 1 & 6 & 5 \\ 6 & 2 & 4 \\ 5 & 4 & 3 \end{pmatrix} \quad (2.7)$$

Finally, the relationship between stress and strain can be written as:

$$\sigma_i = c_{ij}\epsilon_j. \quad (2.8)$$

The elastic constants can now be summarized readily:

$$c_{ij} = \begin{bmatrix} c_{11} & & & & & & \\ c_{12} & c_{22} & & & & & \\ c_{13} & c_{23} & c_{33} & & & & \\ c_{14} & c_{24} & c_{34} & c_{44} & & & \\ c_{15} & c_{25} & c_{35} & c_{45} & c_{55} & & \\ c_{16} & c_{26} & c_{36} & c_{46} & c_{56} & c_{66} & \end{bmatrix} \quad (2.9)$$

They can be further reduced depending on the symmetry of the medium (see [Nye57]). If the solid has orthorhombic, hexagonal, tetragonal or cubic symmetry it will be described by 9, 6, 5 and 3 independent elastic constants, respectively.

In the simplest case of an isotropic elastic solid two elastic moduli are sufficient to describe the elastic behavior of the materials, e. g. the *Lamè constants* λ_L and μ_L , whereby λ_L is the *first Lamè constant* and μ_L is the *second Lamè constant*. In this case Eq. (2.8) reduces to:

$$\sigma_{ij} = \lambda_L \cdot \Delta_c \cdot \delta_{kl} + 2 \cdot \mu_L \cdot \epsilon_{kl} \quad (2.10)$$

with the Kronecker symbol δ_{kl} equal to 1 for $k = l$ and 0 for $k \neq l$, respectively. Δ_c represents the cubic dilatation and for small deformations: $\Delta_c = \epsilon_{xx} + \epsilon_{yy} + \epsilon_{zz}$. Other elastic moduli can be derived from the *Lamè constants*:

- *bulk modulus*, B is a measure for the resistance of the medium to volumetric change (see Fig. 2.1a) and is given by:

$$B = \lambda_L + \frac{2}{3}\mu_L, \quad (2.11)$$

- *Young's modulus*, E is defined as the resistance to elongation and is given by:

$$E = \frac{(3\lambda_L + 2\mu_L)}{(\lambda_L + \mu_L)}\mu_L, \quad (2.12)$$

- *shear modulus*, G (also known as *modulus of rigidity*) is a measure of the resistance of the medium to shear (see Fig. 2.1b). The second Lamè constant is identical to shear modulus:

$$G = \mu_L, \quad (2.13)$$

- *Poisson's ratio*, ν is defined as the ratio between the fractional lateral contraction and the fractional longitudinal extension (see Fig. 2.1c) and is given by:

$$\nu = \frac{\lambda_L}{2(\lambda_L + \mu_L)}. \quad (2.14)$$

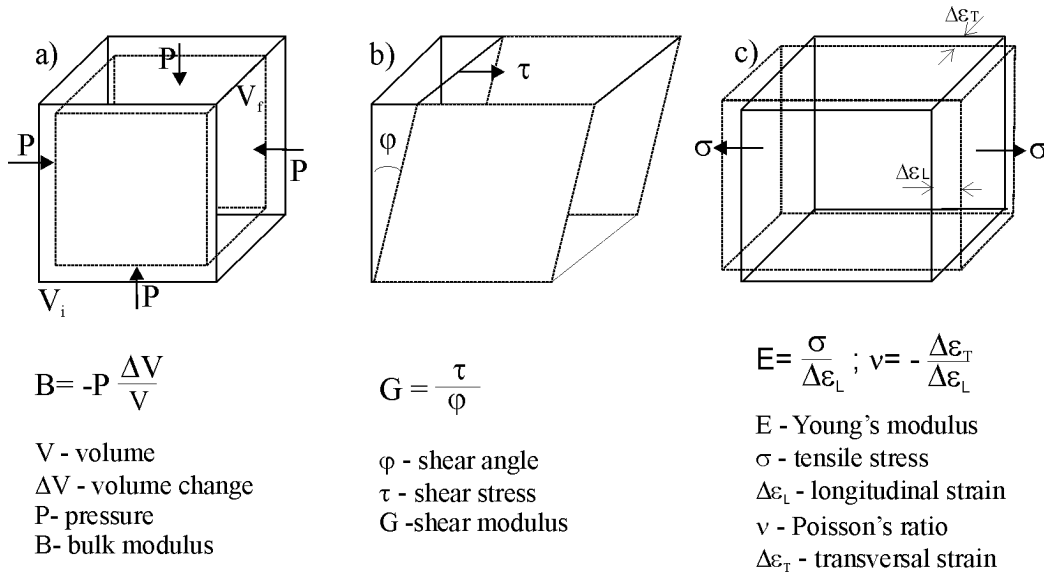


Figure 2.1: Illustration of (a) bulk modulus, (b) shear modulus, (c) Young's modulus and Poisson's ratio

Solving the equations of motion through an isotropic elastic medium and using Eq. (2.10) the velocities for the two types of waves can be derived. The velocities for *longitudinal* or *compressional waves* (P) are:

$$v_P = \sqrt{\frac{\lambda_L + 2\mu_L}{\rho}} = \sqrt{\frac{B + \frac{4}{3}G}{\rho}}. \quad (2.15)$$

In *transversal* or *shear waves* (S), the particle oscillation is perpendicular to the propagation direction and involves shearing motions without any volume change:

$$v_S = \sqrt{\frac{G}{\rho}}. \quad (2.16)$$

Calculation of elastic constants for polycrystalline aggregates

Considering a crystalline aggregate which consists of single phase monocrystals having a random orientation, the determination of the stress or strain distribution with respect to an external load can be established for two extreme cases: by equating the uniform strain in the polycrystalline aggregate to the external strain or alternatively the uniform stress to the external stress. The former scheme is called the Voigt approximation [Voi28] and the latter is called the Reuss approximation [Reu29]. It is evident that the Voigt and Reuss approximations are true only when the aggregate considered is composed of isotropic crystals. If one wants to calculate the average isotropic elastic moduli from the anisotropic single crystal elastic constants, one finds that the Voigt and Reuss assumptions result in the theoretical maximum and minimum values of the isotropic elastic moduli, respectively.

For specific cases of orthorhombic solids, the Reuss shear modulus (G_R) and the Voigt shear modulus (G_V) are:

$$G_R = \frac{15}{4(s_{11} + s_{22} + s_{33}) - 4(s_{12} + s_{13} + s_{23}) + 3(s_{44} + s_{55} + s_{66})}, \quad (2.17)$$

and

$$G_V = \frac{1}{15}(c_{11} + c_{22} + c_{33} - c_{12} - c_{13} - c_{23}) + \frac{1}{3}(c_{44} + c_{55} + c_{66}), \quad (2.18)$$

and the Reuss bulk modulus (B_R) and the Voigt bulk modulus (B_V) are defined as:

$$B_R = \frac{1}{(s_{11} + s_{22} + s_{33}) + 2(s_{12} + s_{13} + s_{23})}, \quad (2.19)$$

and

$$B_V = \frac{1}{9}(c_{11} + c_{22} + c_{33}) + \frac{2}{9}(c_{12} + c_{13} + c_{23}). \quad (2.20)$$

In equations (2.17) and (2.19), the s_{ij} are the elastic compliance constants. Note that the stress-strain relationships can be also written in the matrix form:

$$\epsilon_i = s_{ij}\sigma_j, \quad (2.21)$$

where s_{ij} is the compliance matrix and $s_{ij} = c_{ij}^{-1}$. Using energy considerations Hill [Hil52] proved that the Voigt and Reuss equations represent upper and lower limits of the true polycrystalline constants, and recommended that a practical estimate of the bulk and shear moduli were the arithmetic means of the extremes. Hence, the elastic moduli of the polycrystalline material can be approximated by Hill's average and for shear moduli it is $G = \frac{1}{2}(G_R + G_V)$ and for bulk moduli it is $B = \frac{1}{2}(B_R + B_V)$. The Young's modulus, E , and Poisson's ratio, ν , can be then calculated using the following formula:

$$E = \frac{9BG}{3B + G} \quad \text{and} \quad \nu = \frac{3B - 2G}{2(3B + G)} \quad (2.22)$$

2.1.2 Thermal properties

In addition to the elastic behavior of materials, the thermal behavior is also important. To describe the heat transfer in solids, the conduction equation is applied. A temperature gradient, ∇T , causes a heat flux Q [W/m^2], which is described by Fourier's law:

$$Q = -\lambda \cdot \nabla T \quad (2.23)$$

where λ is a positive coefficient, the **thermal conductivity**. The heat thus flows in the direction of the greatest difference in temperature and the rate of flow is directly proportional to the temperature gradient. If the medium is anisotropic, i. e. if the conductivity depends upon direction, λ represent the conductivity tensor and has the following form:

$$\lambda = \begin{pmatrix} \lambda_{11} & & \\ \lambda_{12} & \lambda_{22} & \\ \lambda_{13} & \lambda_{23} & \lambda_{33} \end{pmatrix} \quad (2.24)$$

where, for example, λ_{12} denotes the thermal conductivity in the x direction across a surface with normal in the y direction, λ_{13} denotes the thermal conductivity in the x direction across a surface with normal in the z direction, etc. Then the heat flux becomes a vector quantity.

Transient heat transfer problems occur when the temperature distribution changes with the time. The fundamental quantity that enters into heat transfer situations not at steady state is the **thermal diffusivity**. It is related to the steady-state thermal conductivity, λ , through the equation:

$$\chi = \frac{\lambda}{c_P \rho} \quad (2.25)$$

where χ is the thermal diffusivity, c_P is the specific heat at constant pressure and ρ is the density. The diffusivity is a measure of how quickly a body can change its temperature. It increases with the ability of the body to conduct heat, λ and it decreases with the amount of heat needed to change the temperature of a body, c_P .

2.1.3 Thermoelastic properties at atomic scale

It is well known that in a crystal the atoms vibrate. Harmonic approximation assume that the atoms will not deviate substantially from their equilibrium positions. In this case the potential energy is written as:

$$U = U_{eq} + U_{harm} \quad (2.26)$$

where U_{eq} is the equilibrium potential energy and U_{harm} is the harmonic potential and usually has a quadratic form. In reality the harmonic approximation neglects important physical phenomena. In an harmonic crystal there will be no thermal expansion, the elastic constants will not depend on temperature and pressure, the elastic waves will not interact and an elastic wave will not be damped in time [Kit96]. If, for example, the thermal expansion of an harmonic oscillator is considered, it can be seen from the

form of an harmonic potential (Fig. 2.2a) that the distance $d_1 - d_0$ is the same as the distance $d_0 - d_2$. This means that the equilibrium separation is always d_0 for all temperatures, i.e. the coefficient of thermal expansion will be zero. If a potential energy with an asymmetric curve is considered (Fig. 2.2b), the center of the oscillation is at a separation which is greater than d_0 . As the temperature increases the equilibrium separation increases. The inclusion of the anharmonic terms is therefore very important when calculating thermal expansion of a solid. Further corrections to U especially those

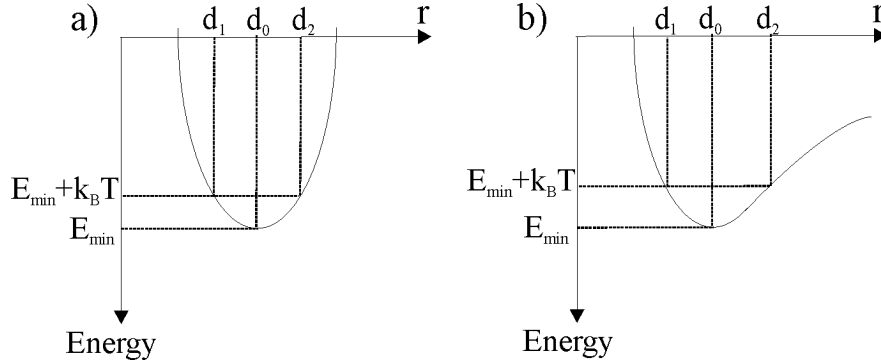


Figure 2.2: Thermal expansion can be explained using a typical potential energy. At temperature $T = 0$ K the energy of the system is E_{min} . At finite temperatures the finite energy is $E_{min} + k_B T$ corresponding to an atomic separation between d_2 and d_1 , i.e. d_0 : (a) harmonic potential; (b) anharmonic potential

of third and fourth order known as anharmonic terms are of considerable importance in understanding the physical phenomena mentioned above. The potential energy in this case is given by [Ash71]:

$$U = U_{eq} + U_{harm} + U_{anh} \quad (2.27)$$

Real crystals exhibit thermal resistance which can also be explained through the anharmonicity effect. Thermal resistance appears as a result of interchange of energy between lattice waves (phonons), that is, scattering. Scattering can be caused by static imperfections and anharmonicity. The static imperfections include grain boundaries, impurities, vacancies, interstitials, dislocations and their associated strain fields. At low temperatures the thermal energies are not so high, and there are few phonons. That means the probability of phonons interacting strongly with one another is low. The energy of the phonons is given by: $E = h_{pc}/\lambda'$, where λ' represents the wavelength associated with the phonon. In this case the energy of phonons is low and therefore the wavelength is large. As a consequence, the phonons are not easily scattered by the impurities and imperfections. With increasing temperatures, there are a large number of phonons and so the probability of interactions with other phonons is much higher. The wavelength becomes shorter, which means that the phonons interact strongly with impurities and imperfections. Elastic strains in the crystals scatter because of the strain dependence of the elastic properties, a nonlinear and anharmonic effect.

From the kinetic theory of gases, the following expression of the thermal conductivity

was derived [Kit96]:

$$\lambda = \frac{1}{3}C_V v \ell \quad (2.28)$$

where C_V is the specific heat at constant volume, v the average velocity of the phonons and ℓ the average free path of phonons. Knowing that the sound is transmitted by the vibrations of the atoms, it can be assumed that the velocity of the phonons is approximately equal to the velocity of sound. The appropriate average of the sound velocities is given, in Debye theory by:

$$v = \left[\frac{1}{3} \left(\frac{1}{v_P^3} + \frac{2}{v_S^3} \right) \right]^{-1/3}, \quad (2.29)$$

where v_P and v_S are longitudinal and transversal average sound velocities. In Debye theory, the specific heat capacity at low temperature is given by:

$$C_V = \frac{12R\pi^4}{5} \left(\frac{T}{\Theta_D} \right)^3 \quad (2.30)$$

where R is the molar gas constant, T is the temperature and Θ_D is the Debye temperature: $\Theta_D = h_P \omega_{max} / k_B$ with h_P being the Planck's constant, ω_{max} the maximal vibrational frequency and k_B the Boltzmann's constant. Therefore at low temperature a temperature dependence of C_V on T^3 is predicted, as observed in experiments. At high temperatures C_V is limited by the value for the classical harmonic solid: $C_V = 3N_A k_B = 3R$. The mean free path of the phonons can be estimated as:

$$\ell \approx \frac{d}{\alpha \gamma T}, \quad (2.31)$$

where d is the interatomic distance, α the thermal expansion coefficient and γ the thermodynamic Grüneisen parameter. That means, the calculation of λ from kinetic theory requires the calculation of C_V , v , α , and γ at the pressure and temperature conditions of interest.

The coefficient of thermal expansion and Grüneisen parameter are given by:

$$\alpha = \frac{1}{V} \left(\frac{\partial V}{\partial T} \right)_P = \frac{1}{B} \left(\frac{\partial P}{\partial T} \right)_V \quad (2.32)$$

and

$$\gamma = \frac{VB\alpha}{C_V} \quad (2.33)$$

where $B = -V(\partial P/\partial V)_T$ is the isothermal bulk modulus. Therefore, Eq. (2.28) becomes:

$$\lambda = \frac{\frac{1}{3} \left(\frac{1}{v_P^3} + \frac{2}{v_S^3} \right)^{-1/3} \alpha B}{\rho \gamma^2 T} \quad (2.34)$$

Equation (2.34) gives the expression of thermal conductivity and it can be seen that it depends on properties like, bulk modulus, coefficient of thermal expansion and Grüneisen parameter.

2.2 Quantum mechanics simulations of material properties

Quantum mechanics (QM) (called also first principles) methods, such as Density Functional Theory (DFT) and Hartree-Fock, require only the positions and atomic numbers of each atom as input in the calculation. A pre-defined methodology, containing no adjustable parameters, approximates a solution to the Schrödinger equation [Sch26]. These methods work for every element in the periodic table, and a vast literature demonstrates their accuracy. DFT [Hoh64], [Koh65] is based on functions that describe the electron density. The results of these calculations usually include the position of all of the atoms concerned, the forces on them, the electronic structure and the energy of the system. From these basic data, and how they develop over time, most other key properties can be derived. In the last years DFT became a very powerful tool in computational condensed matter physics and therefore, in the present study, this method is employed.

2.2.1 Density functional theory (DFT)

The energy may be computed by solution of Schrödinger equation, which in time-dependent, non-relativistic, Born-Oppenheimer approximation is:

$$\hat{H}\Psi(r_1, r_2, \dots, r_N) = E\Psi(r_1, r_2, \dots, r_N) \quad (2.35)$$

Here r_i is the coordinate of electron i . The Hamiltonian operator, \hat{H} , consists of a sum of three terms: the kinetic energy, \hat{T} , the interaction with the external potential, \hat{V}_{ext} and the electron-electron interaction, \hat{V}_{ee} :

$$\hat{H} = \hat{T} + \hat{V}_{ext} + \hat{V}_{ee} = -\frac{1}{2} \sum_i^N \nabla_i^2 - \sum_\alpha^{Nat} \frac{Z_\alpha e^2}{|r_i - R_\alpha|} + \frac{1}{2} \sum_{i < j}^N \frac{e^2}{|r_i - r_j|} \quad (2.36)$$

where the external potential represents simply the interaction of the electrons with the atomic nuclei (the charge of the nucleus at R_α is Z_α) and the electron-electron interaction, is the Coulomb potential between electrons, with e being the electron charge.

Kohn and Sham theorems [Hoh64], [Koh65] lead to the fundamental statement of the density functional theory:

$$\delta \left[E[\rho] - \mu_{ch} \left(\int \rho(r) dr - N \right) \right] = 0 \quad (2.37)$$

The ground state energy and density correspond to the minimum of functional $E[\rho]$, subject to the constraint that the density contains the correct number of electrons. The Lagrange multiplier of this constraint is the electronic chemical potential μ_{ch} . $E[\rho]$ is a universal functional. If its form is known, it could be inserted into the above equation and minimized to obtain the exact ground state density and energy.

From the form of the Schrödinger equation (Eq. (2.35)) it can be seen that the energy functional contains three terms: the kinetic energy, the interaction with the external potential and the electron-electron interaction, and so we may write the functional as:

$$E[\rho] = T[\rho] + V_{ext}[\rho] + V_{ee}[\rho] \quad (2.38)$$

The interaction with the external potential is given by:

$$V_{ext}[\rho] = \int \hat{V}_{ext} \rho(r) dr, \quad (2.39)$$

but the kinetic and electron-electron functionals are unknown.

Kohn and Sham proposed the following approach to approximating the kinetic and electron-electron functionals. They introduced a fictitious system of N non-interacting electrons to be described by a single determinant wave function in N orbitals Ψ_i . In this system the kinetic energy and electron density are known exactly from the orbitals:

$$T_s[\rho] = -\frac{1}{2} \sum_i^N \langle \Psi_i | \nabla^2 | \Psi_i \rangle \quad (2.40)$$

Here the suffix s emphasizes that this is not the true kinetic energy but that of a system of non-interacting electrons, which reproduce the true ground state density: $\rho(r) = \sum_i^N |\Psi_i|^2$. If it is also noted that a significant component of the electron-electron interaction will be the classical Coulomb interaction written in terms of density as:

$$V_H[\rho] = \frac{1}{2} \int \frac{\rho(r_1)\rho(r_2)}{|r_1 - r_2|} dr_1 dr_2 \quad (2.41)$$

then the energy functional can be rearranged:

$$E[\rho] = T_S[\rho] + V_{ext}[\rho] + V_H[\rho] + E_{xc}[\rho] \quad (2.42)$$

Here the exchange-correlation functional $E_{xc}[\rho]$ was introduced and is given by:

$$E_{xc}[\rho] = (T[\rho] - T_S[\rho]) + (V_{ee}[\rho] - V_H[\rho]) \quad (2.43)$$

$E_{xc}[\rho]$ is simply the sum of the error made in using a non-interacting kinetic energy and the error made in treating the electron-electron interaction classically. Writing the functional Eq. (2.42) explicitly in terms of density and applying the variational theorem Eq. (2.37), the orbitals, which minimize the energy, satisfy the following set of equations:

$$\left[-\frac{1}{2} \nabla^2 + \nu_{ext}(r) + \frac{\rho(r')}{|r - r'|} dr' + \nu_{xc}(r) \right] \Psi_i(r) = \epsilon_i \Psi_i(r) \quad (2.44)$$

in which a local multiplicative potential was introduced: the functional derivative of the exchange correlation energy with respect to the density,

$$\nu_{xc}(r) = \frac{\delta E_{xc}[\rho]}{\delta \rho} \quad (2.45)$$

This set of non-linear equations (the Kohn-Sham equations) describes the behavior of non-interacting electrons in an effective local potential.

The local exchange correlation energy per electron might be approximated as a simple function of the local charge density ($\epsilon(\rho)$). That is, an approximation of the form:

$$E_{xc}[\rho] \approx \rho(r) \epsilon_{xc}(\rho(r)) dr, \quad (2.46)$$

where ϵ_{xc} will be the exchange and correlation energy density of the uniform electron gas of the density ρ - this is the local density approximation (LDA). Within LDA, ϵ_{xc} is a function of only the local value of the density. It can be separated into exchange and correlation contributions:

$$\epsilon_{xc}(\rho) = \epsilon_x(\rho) + \epsilon_c(\rho) \quad (2.47)$$

A natural progression beyond the LDA is thus to the general gradient approximation (GGA). In the GGA a functional form is adopted which ensures the normalization condition and that the exchange hole is negative definite. This leads to an energy functional that depends on both the density and its gradient but retains the analytic properties of the exchange correlation hole inherent in the LDA. The typical form for a GGA functional is:

$$E_{xc} \approx \int \rho(r) \epsilon_{xc}(\rho, \delta\rho) dr \quad (2.48)$$

For a better understanding of the way that simulations are performed a short description of some important concepts is presented in the following.

The supercell approach assumes that simulations must be performed on a periodic system, even when the periodicity is superficial. For example, if one wants to study molecules it is necessary to assume that they are in a box and treat them as **periodic systems**.

The periodic boundary conditions are related to Bloch's theorem, which uses the periodicity of a crystal to reduce the infinite number of one electron wave functions to be calculated to simply the number of electrons in the unit cell of the crystal. The wave function is written as the product of a wavelike part and a cell periodic part:

$$\Psi_i(r) = u_i(r) e^{(ik \cdot r)}, \quad (2.49)$$

where k is the wave vector. The cell periodic part, $u_i(r)$ can be expanded using a **basis set** consisting of a discrete set of **plane waves**, whose wave vectors are reciprocal lattice vectors (K) of the crystal:

$$u_i(r) = \sum_K C_{i,K} e^{(iK \cdot r)}. \quad (2.50)$$

The reciprocal lattice vectors K are defined by $K \cdot L = 2\pi m$ for all L , where L is a lattice vector of the crystal and m is an integer. Therefore, each electronic wave function, Ψ is expressed as a sum of plane waves which differ by reciprocal lattice vectors:

$$\Psi_i^k(r) = \sum_K C_{i,k+K} e^{(i(k+K) \cdot r)}. \quad (2.51)$$

By use of Bloch's theorem, the problem of the infinite number of electrons has now been mapped onto the problem of expressing the wave functions in term of an infinite number of reciprocal space vectors within the **first Brillouin zone** of the periodic cell, k . This problem is dealt with by sampling the Brillouin zone at special set of **k-points**. The first Brillouin zone can be mapped out by a continuous set of k -points $\{k : (k_x, k_y, k_z)\}$, throughout the region of the reciprocal space (k -space). Since k set is dense, there are an infinite number of k -points in the Brillouin zone at which the wave functions must be

calculated. Therefore if a continuum of plane wave basis sets are required, the basis set for any calculation will still be infinite, no matter how small the plane wave energy cutoff was chosen. For this reason the electronic states are only calculated at a set of k -points determined by the shape of the Brillouin zone. The reason that this can be done is that the electronic wave functions at k -points that are very close together will almost be identical. It is therefore possible to represent the electronic wave functions over a region of reciprocal space at a single k -point. This approximation allows the electronic potential to be calculated at a finite number of k -points and hence determine the total energy of solid. In order to obtain very accurate approximations to the electronic potential there are a number of methods which choose the set of k -points within the Brillouin zone, the Monkhorst and Pack scheme [Mon76] being the most commonly used.

The valence electrons of an atom are responsible for the chemical bonding and most physical properties. The core electrons are affected little by the atomic environment, i.e. only the valence electrons are considered in the calculations. The real potential, arising from the nuclear charge and the core electrons, is replaced with an effective potential, within a core region of radius R_c . This requires fewer plane waves. Fig. 2.3 illustrate a schematic representation of a **pseudopotential**. Thus, the pseudopotential is required

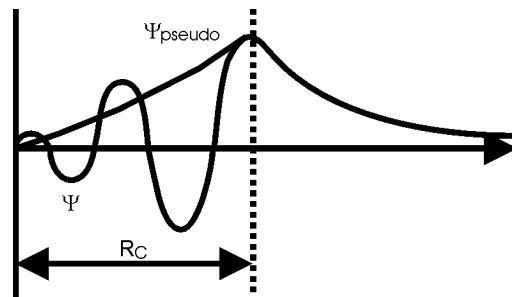


Figure 2.3: Schematic representation of a pseudopotential

to reproduce the behavior and properties of the valence electrons in the all-electron calculation. There are two types of pseudopotentials:

- *norm-conserving pseudopotential*: the total valence electron density within the core radius equals that in the all-electron situation;
- *ultrasoft pseudopotential*: relaxation of the norm-conservation requirement, only fewer plane waves are required.

The **electronic relaxation** is also important because it involves the minimization of the total energy. The electronic wave functions are expanded using a plane-wave basis set, and the expansion coefficients are varied so as to minimize the total energy. This minimization can be achieved either by using a band-by-band technique, where each wave function is optimized independently, or by a modern all-bands method that allows simultaneous update of all wave functions. Another alternative is based on density mixing [Kre96]. In this scheme the sum of electronic relaxation electronic eigenvalues is minimized in the fixed potential. The new charge density at the end of the step is mixed with the initial density and the process is repeated until convergence.

2.3 Finite Element Method (FEM)

It is already known that the material properties can be calculated starting from first principles (quantum mechanics) by using only the coordinates of the atoms in the unit cell. The method has the advantage to provide high-quality quantitative predictions but has the disadvantage to be very time consuming when large systems are considered. For larger systems at a large scale the finite element method can be employed.

The finite element method has a long history of success in diverse applications ranging from civil engineering to material science. The first applications in engineering date back to the '50s. FEM is a numerical technique for solving problems which are described by partial differential equations or can be formulated as functional minimization [Zie71]. A domain of interest is represented as an assembly of finite elements. Approximating functions in finite elements are determined in terms of nodal values of a physical field which is sought. A continuous physical problem is transformed into a discretized finite element problem with unknown nodal values. For a linear problem a system of linear algebraic equations should be solved. Values inside finite elements can be recovered using nodal values.

Fig. 2.4 shows the sequences of a finite element simulation. In the following, some

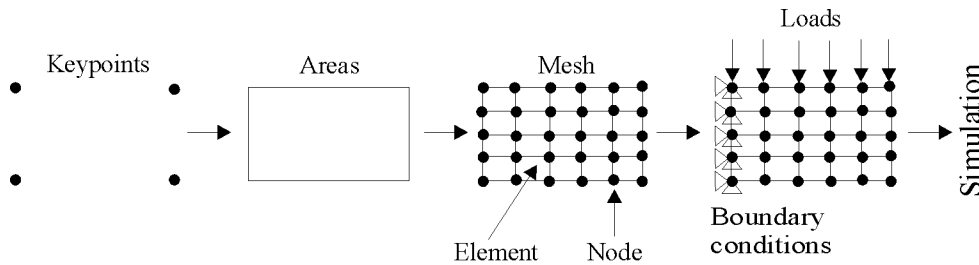


Figure 2.4: Principle of FEM

important steps which summarize how the FEM is working are presented:

1. *Discretization.* The first step is to divide a solution region into finite elements. First the geometry of the domain must be generated. In the work presented here the software package ANSYS was used. In ANSYS some geometrical objects like keypoints, lines, areas, volumes are available. After the geometry was obtained the mesh must be performed. The finite element mesh is typically generated by a preprocessor program. The elements can be one, two or three dimensional, depending on the problem to be solved. Volumes can be meshed with 3D elements, areas with 2D elements, like shell elements and lines with beam, link or pipe elements. The elements are connected through nodes, which can have different degrees of freedom (DOF), like displacements, temperature, potentials, etc. and they are the unknown in FE simulations (see Fig. 2.5). In principle, the mesh consists of several arrays which are nodal coordinates and element connectivities.

2. *Interpolation functions.* Interpolation functions are used to interpolate the field variables over the element. Often, polynomials are selected as interpolation functions. The degree of the polynomial depends on the number of nodes assigned to the element.

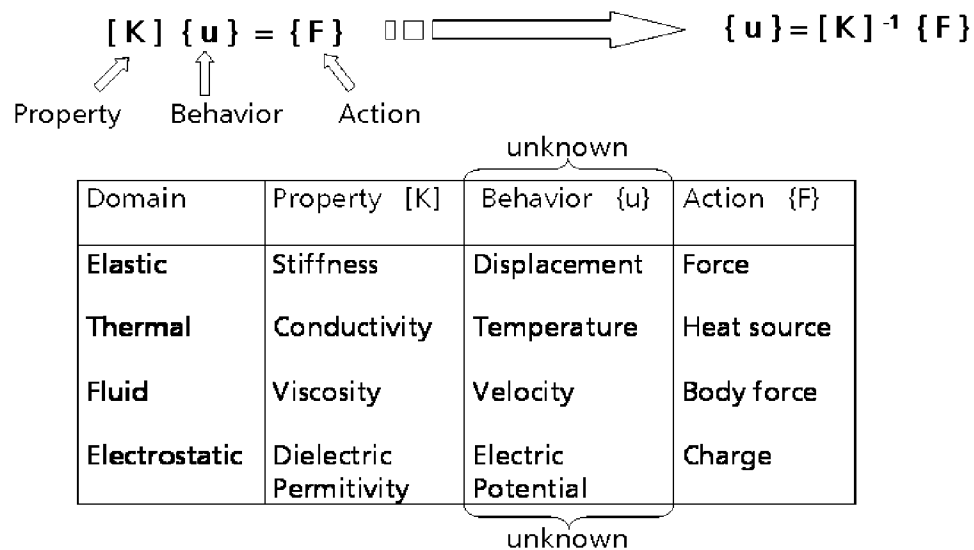


Figure 2.5: DOFs of various problems

The elements can also have middle nodes (see Fig. 2.6).

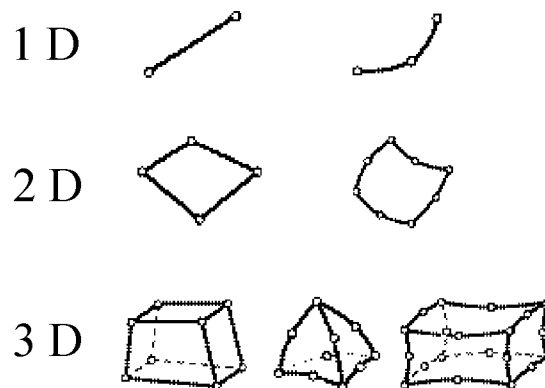


Figure 2.6: Different element types

3. *Element properties.* The matrix equation for the finite element, which relates the nodal values of the unknown function to the other parameters, should be established. For this task different approaches can be used. The most convenient are the variational approach [Mit71] and the Galerkin method [Mit71], [Coo81].

4. *Assembly of the element equations.* To find the global equation system for the whole solution region, the all element equations must be assembled, i.e. the local element equations for all elements must be combined by using element connectivity. Before solution, boundary conditions (which are not accounted in element equations) should be imposed.

5. *Solving the global equation system.* The global finite element equation system is typically sparse, symmetric and positive definite. Direct and iterative methods can be used for solution.

6. *Computation of additional results.* In many cases one needs to calculate additional parameters. For example, in mechanical problems strain and stress are of interest in addition to displacements, which are obtained after solution of the global equation system.

In Appendix A, an example which contains the calculation of stresses for a 3D element using FEM is presented.

Chapter 3

Numerical methods

3.1 Simulation of material properties using QM

For the present study calculations of the elastic constants for a wide range of ceramic materials: Al_2O_3 , SiC , TiO_2 , AlN , BN , TiB_2 , CaF_2 and ZrO_2 were performed. The simulations based on quantum mechanics method have been employed, by using CASTEP (Cambridge Serial Total Energy Package) [Seg02], which is a program designed specifically for solid state material science. It employs density functional theory which allows to perform first principles (ab-initio) quantum mechanics calculations that explore the properties of crystals in materials like ceramics, semiconductors, metals, minerals etc. In Fig. 3.1 a flow diagram shows the steps of a simulation.

In order to perform the simulations, a plane wave basis set was used for expanding electronic states in the pseudopotential approximation. Plane waves are included with energies up to a cutoff energy (Table 3.2). The norm-conserving (NC) and ultrasoft (US) pseudopotentials from the CASTEP database have been employed for the computations. Exchange-correlation effects were taken into account using the generalized gradient approximation, GGA [Per92] in the formulation of Perdew, Burke and Ernzerhof [Per96], [Per96a]. Reciprocal space integration in the Brillouin zone is performed by summation over k -points. Here the Monkhorst-Pack method [Mon76] was used, whereby the k -points are distributed homogeneously throughout space in rows and columns that follow the shape of the Brillouin zone. The number of k -points necessary for converged results differs between structures due to symmetry and the degree of dispersion in electronic states (Table 3.2). With the computational parameters applied here a very high level of convergence of elastic parameters is achieved.

In this study two types of calculations have been carried out. The first set of simulations was performed to obtain the static equation of state (EOS) of above mentioned ceramic materials. Internal and external degrees of freedom were optimized for a number of structures (at constant volume), typically covering a compression range from 0.8 to 1.06 relative to the experimental zero pressure volume (see Table 3.2). In order to obtain the zero pressure volume, V_0 , the bulk modulus, B and its pressure derivative, B' , the energies were computed and then used to fit a finite strain equation of state [Bir52]:

$$P = 3B_0 f_E (1 + 2f_E)^{7/2} \left[1 + \frac{3}{2}(B'_0 - 4)f_E + \dots \right], \quad (3.1)$$

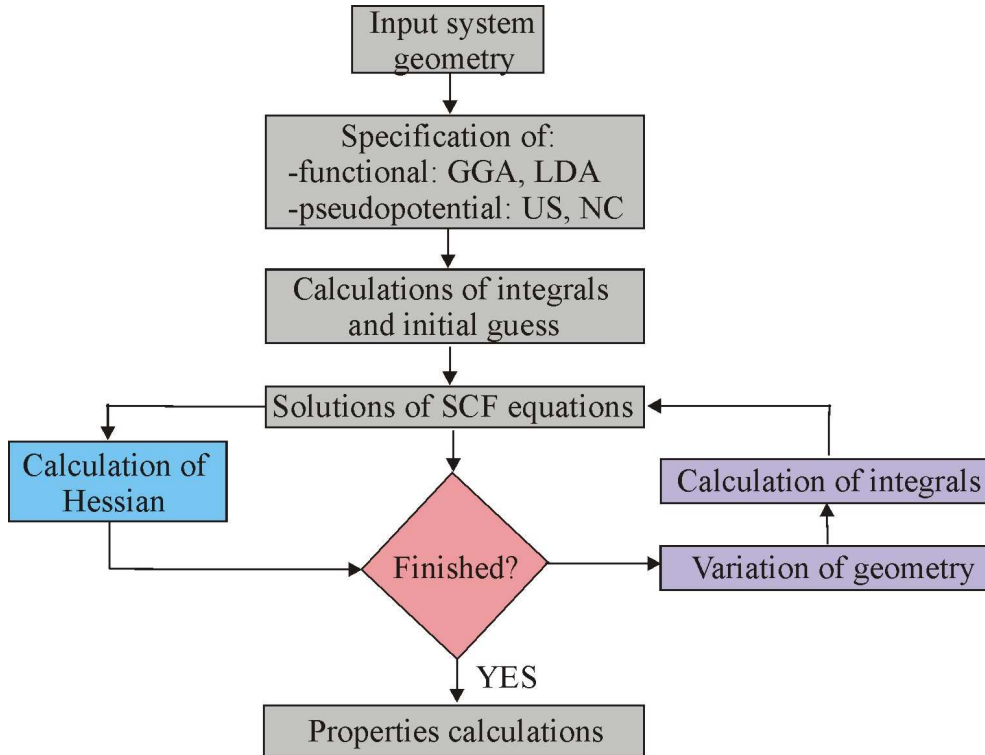


Figure 3.1: Flow diagram of quantum mechanics simulations

where f_E is the Eulerian finite strain parameter and is given by:

$$f_E = \frac{1}{2} \left[\left(\frac{V_0}{V} \right)^{2/3} - 1 \right].$$

Another set of simulations was performed in order to obtain the elastic coefficients of ceramic materials. The calculation of the elastic constants from first principles is based on applying small strains to the ground state structure, followed by the relaxation of the atomic positions and a subsequent computation of the stress tensor. Elastic coefficients are then determined from a linear fit of the computed stress to the applied strain, where 3 – 6 amplitudes up to a maximum of 0.003 have been used.

3.1.1 Crystal structure of investigated materials

The unit cells of some materials investigated are shown in Fig. 3.2. In Table 3.1 the crystal structures of the ceramic phases are presented. For rhombohedral crystals, like Al_2O_3 , there are six independent elastic constants c_{11} , c_{33} (which represent the longitudinal distortions in x -(or y -) and z -directions), c_{44} (shear distortion in the x - or y -direction), and the off-diagonal constants c_{12} , c_{13} and c_{14} . Hexagonal structures, i.e. α -SiC, AlN and TiB_2 have also six elastic constants, but only five of them (c_{11} , c_{33} , c_{44} , c_{12} and c_{13}) are required to describe their elastic behavior, since $c_{66} = (c_{11} - c_{12})/2$. Table 3.1 shows the crystal structure of TiO_2 rutile and anatase phases, both structures

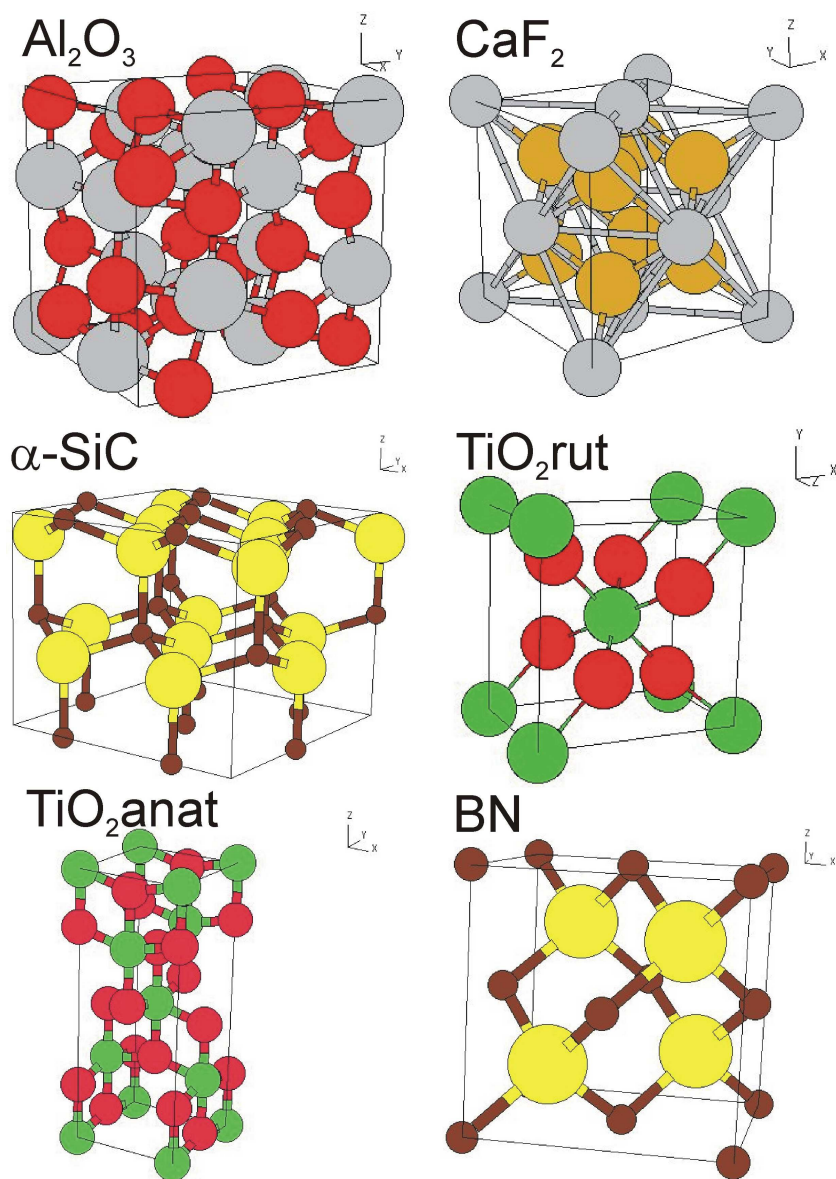


Figure 3.2: Unit cell of Al₂O₃, CaF₂, α – SiC, TiO₂ rutile, TiO₂ anatase and BN

having a tetragonal symmetry with six unique elastic constants (c_{11} , c_{33} , c_{44} , c_{66} , c_{12} and c_{13}). Because of the high symmetry cubic systems like, β -SiC, CaF₂ and BN, have only three elastic constants: c_{11} , c_{12} and c_{44} . The most complex structure in this study is the monoclinic ZrO₂ crystal, which has 13 elastic constants (c_{11} , c_{22} , c_{33} , c_{44} , c_{55} , c_{66} , c_{12} , c_{13} , c_{15} , c_{23} , c_{25} , c_{35} and c_{46}).

3.1.2 Convergence of simulations

Two important parameters that affect the accuracy of calculations are the kinetic cutoff energy, which determines the number of plane waves and the number of special k -points used for the Brillouin zone integration. Therefore, convergence of the simulations with respect to these parameters was studied. Here we present results on the cell volume as a function of these parameters allowing for the relaxation of internal and external degrees of freedom. For a given set of k -points and a cutoff energy a calculation was considered converged when the maximum force on atoms was below 0.03 eV/Å and the stress below 0.05 GPa.

In Fig. 3.3 the results of convergence simulations for two systems, Al₂O₃ and TiO₂ rutile are presented. Further results of the convergence study for every material are presented in Table 3.2.

The simulations mentioned above were performed on a PC cluster with eight CPUs (every CPU being a 2.4 GHz Pentium 4). The computational time for the calculation of the cell volumes through geometry optimization was not expensive (except for monoclinic ZrO₂), one to five hours. Concerning the calculation of elastic constants the computational time was different, depending on the complexity of the structures (for cubic symmetry some hours and for monoclinic symmetry about 72 hours).

Table 3.1: Crystal structures of the studied materials. Space group and lattice parameters are given in the first line for each material; the atomic positions in the following lines

Material	Space group		a (Å)	b (Å)	c (Å)	α°	β°	γ°
	Atom	Position	x	y	z			
Al ₂ O ₃	R-3cr (167)		5.129	5.129	5.129	55.29	55.29	55.29
	Al	4 c	0.145	0.145	0.145			
	O	6 e	0.947	0.553	0.250			
α -SiC	P63mc (186)		3.087	3.087	10.046	90	90	120
	Si	2 a	0	0	0.188			
	Si	2 b	0.333	-0.333	0.438			
	C	2 a	0	0	0			
	C	2 b	0.333	-0.333	0.250			
β -SiC	F43m (216)		4.384	4.384	4.384	90	90	90
	Si	4 a	0	0	0			
	C	4 c	0.25	0.25	0.25			
TiO ₂ r	P42/mmm (136)		4.594	4.594	2.959	90	90	90
	Ti	2 a	0	0	0			
	O	2 f	0.301	0.301	0			
TiO ₂ a	I41/amds (141)		3.776	3.776	9.486	90	90	90
	Ti	4 a	0	0	0			
	O	8 e	0	0	0.208			
CaF ₂	Fm-3m (225)		3.863	3.863	3.863	90	90	90
	Ca	4 a	0	0	0			
	F	8 c	0.25	0.25	0.25			
AlN	P63m (186)		3.11	3.11	4.98	90	90	120
	Al	2 b	-0.333	-0.666	0			
	N	2 b	0.333	-0.666	0.382			
BN	Fm-3m (225)		3.615	3.615	3.615	90	90	90
	B	4 a	0	0	0			
	N	4 c	0.25	0.25	0.25			
TiB ₂	P6/mmm (191)		3.024	3.024	3.220	90	90	120
	Ti	1 a	0	0	0			
	B	2 d	0.333	0.666	0.5			
ZrO ₂	P21/c (14)		5.145	5.208	5.311	90	99.23	90
	Zr	4 e	0.273	0.034	0.209			
	O	4 e	0.077	0.313	0.305			
	O	4 e	0.462	0.788	0.436			

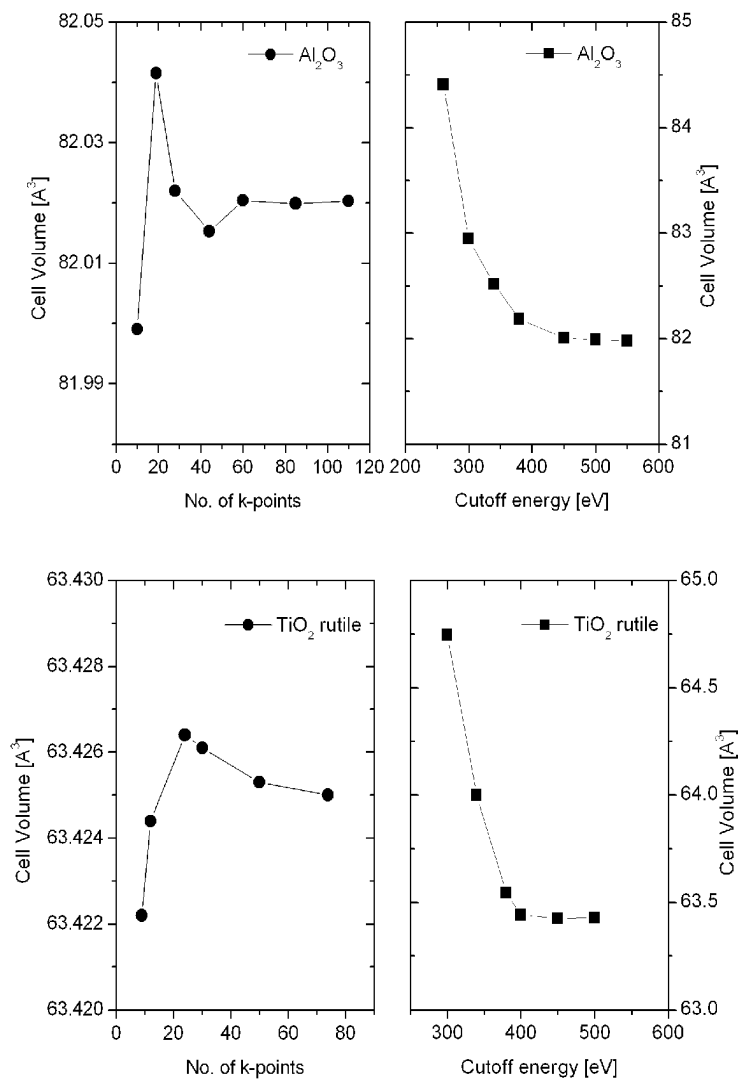
Figure 3.3: Convergence study for Al_2O_3 and TiO_2 rutile

Table 3.2: Computational parameters used in simulations for the elastic constants. Given are the k -point sampling for reciprocal space integration, the cutoff energy for the basis set, the type of pseudopotential (PS) used (norm-conserving NC and ultrasoft US) and the range of cell volume for EOS

	Al_2O_3	$\alpha - SiC$	$\beta - SiC$	$r TiO_2$	$a TiO_2$
kp	85	28	110	50	84
E_{cutoff} [eV]	500	400	400	450	550
PS	US	US	US	US	US
V_{range} [\AA^3]	76.4-90	69.3-87.4	64.9-87.1	59.4-66.1	113.6-148.7
	CaF_2	AlN	BN	TiB_2	ZrO_2
kp	60	84	120	162	39
E_{cutoff} [eV]	500	350	400	400	500
PS	US	US	US	US	US
V_{range} [\AA^3]	36.6-44.8	33.3-44.2	37.3-50	20.3-27	126.4-148.8

3.2 Simulation of material properties using FEM

The flow chart presented in Fig. 3.4 shows how the calculations of thermal and mechanical microstructure properties have been carried out. In the following sections the steps

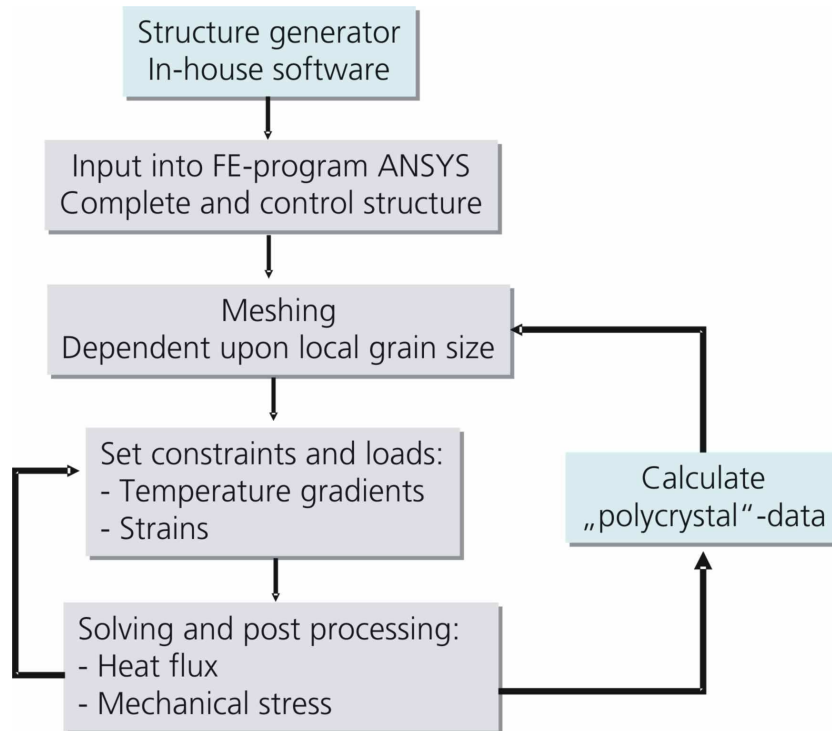


Figure 3.4: Flow diagram of microstructure simulation

are described in detail.

3.2.1 Theoretical microstructures

To simulate the macroscopic properties of polycrystalline ceramics three dimensional structures have been used. The various structures could be classified in two types of models, depending on the arrangement of the particles within the unit cell:

- *Cubic structures* - a periodic arrangement of truncated spheres or other particles with different shapes;
- *Random structures* - a random arrangement of truncated spheres or Voronoi polyhedra.

In this study two phenomena concerning the *cubic structures* have been investigated: the effect of different particle shapes as well as the effect of different arrangement of truncated spheres within the unit cell on thermoelastic properties.

Different particle shapes

Solid particles with different shapes have been used in simulations. Fig. 3.5 shows some elementary particle shapes within their simple cubic unit cell. Truncated spheres (Fig. 3.5a) were used in more complex particle arrangement. The truncated octahedron (Fig. 3.5b) was used to compare the effect of curved particle surfaces to flat surfaces as the latter can occur during sintering of crystalline particles with anisotropic surface energy. The overlapping spheres and cylinders (Fig. 3.5c) were considered since overlapping cylinders were introduced by other authors [Och03], [Sch98]. The sphere at the center of the cell has been added to be able to vary the radius r of the cylinders, which is identical to the particle contact radius, independently from the solid volume fraction.

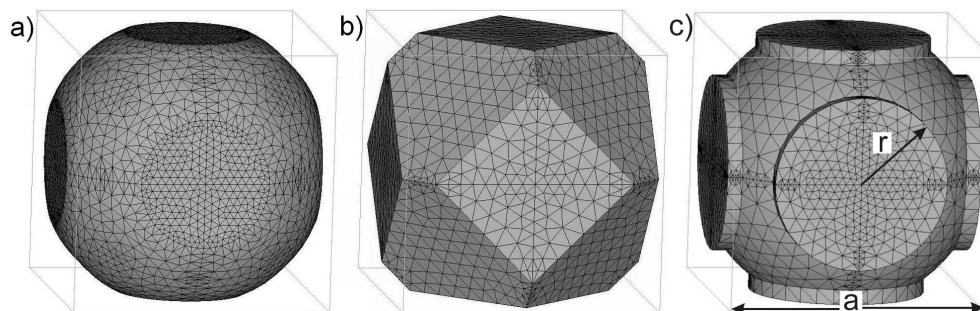


Figure 3.5: Simple cubic particles used in the FE simulations: (a) truncated sphere, (b) truncated octahedron and (c) overlapping sphere and cylinders. Grey lines indicate the unit cell

A solid volume fraction of 70% has been used in Figs. 3.5 - 3.8. It was calculated from the radii and edge lengths of the respective simple bodies using elementary geometry. The inverse problem of finding the radii and the edge lengths for given volume fractions has been solved numerically using an in-house developed software, *Geosphere* (F. Raether, Fraunhofer ISC).

In Fig. 3.6 a particle type which allows a much larger variation of neck area than the overlapping sphere and cylinders is presented. It is formed by a cube (with edge length b), which has 6 respectively 24 cylindrical contacts (with radius r) to its 6 neighbors. Although this particle type looks somewhat artificial, it was considered helpful in understanding microstructure in intermediate stage sintering. Those structures are frequently formed by dense agglomerates loosely connected by small elongated particles.

Fig. 3.7 shows a structure which is very flexible too, but looks more similar to an individual powder particle. It is formed by six truncated squared pyramids based on the sides of an enclosed cube. The lateral surfaces of the pyramids meet at a constant opening angle at the edges of the particle contacts. The structure is completely determined by the opening angle Θ and the volume fraction of solid phase f_s :

$$f_s = \frac{a^3 + 8h^2b + 8hb^2 - 12abh}{a^3}, \quad \text{with } h = b[1 + \tan(\Theta)^{-1}]^{-1} \quad (3.2)$$

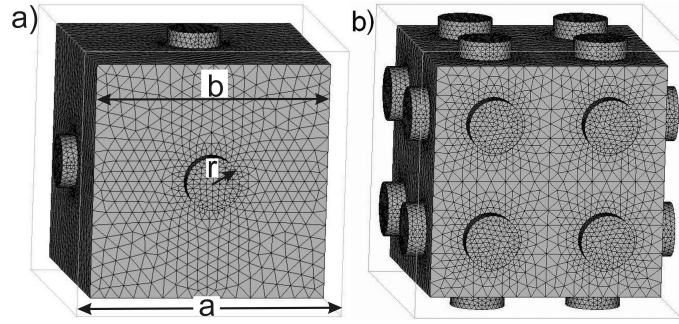


Figure 3.6: Extreme particle shapes used to describe microstructures with high solid volume fractions and small sintering neck areas: (a) cube with 6 cylindrical contacts and (b) cube with 24 cylindrical contacts

where b is the edge length at contact area of pyramids (particle contact area is b^2), h height of pyramids and a the edge length of the unit cell. Increasing the opening angle at constant volume fraction causes a drastic increase of the contact area.

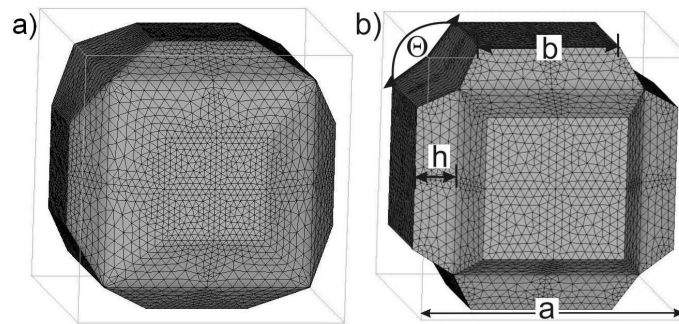


Figure 3.7: Particles formed by six truncated pyramids based on the sides of an enclosed cube with different opening angles Θ : (a) $\Theta = 60^\circ$ and (b) $\Theta = 120^\circ$

Since the plane faces of the structure with truncated square pyramids only reflect materials with anisotropic interface energy another microstructure has been generated by looking for the particle pore interface with minimum energy - assuming that the interface energy doesn't vary with crystal direction (Fig. 3.8). For given volume fractions of the two phases and given spherical neck areas the minimization was performed by the computer program Surface Evolver [Bra92]. It was started with a simple prescribed geometry of cubic symmetry and with correct volume fractions. Due to the high symmetry of the cubic structure only $1/48^{\text{th}}$ of the volume of the unit cell was actually minimized and the structures shown in Fig. 3.8 were constructed by symmetry operations. The interface was composed of small plane triangular facets defined by the coordinates of their vertices. The vertices were moved after subsequent iterations according to an individual force vector. The force vector was calculated locally for each vertex from the tensile stresses originating from the neighboring vertices. Appropriate constraints were

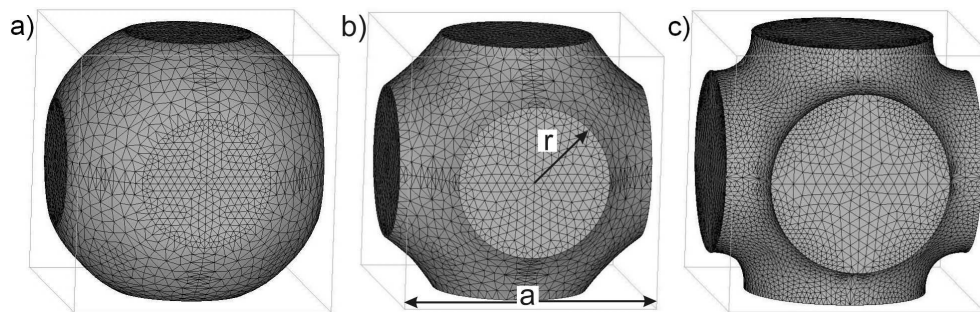


Figure 3.8: Particles formed by minimizing the interface energy at given ratio between neck radii r and edge length of the unit cell a : (a) $r/a = 0.5$, (b) $r/a = 0.6$, (c) $r/a = 0.7$

used to ensure that the cubic symmetry was maintained during the minimization. The mesh was successively refined, ending up with about 100 to 200 vertices. Convergence was achieved after a total of about 100 iterations. Computation time was less than one minute on a usual PC. From Fig. 3.8 it can be seen that curvature at the interface changed from convex to concave if the sintering neck radius, r was increased.

Different particle arrangement

Besides the different particle shapes, various particle arrangements of truncated spheres within the unit cell were considered. Super cells with cubic symmetry which contains some tens of particles have been used to investigate the influence of different particle size, displacement and coordination number on thermoelastic properties. Taking into account the requirement to maintain the cubic symmetry the allowed geometrical variations are reduced.

The displacement of the particles was introduced in order to investigate the effect of agglomeration or large pore formation during sintering. Considering cubic symmetry, a simple transformation was used which generates a constant gradient in mass. For that the centers of the particles were shifted by a displacement vector whose i -th component u_i was calculated according to:

$$u_i = \frac{r'_i - c'_i + a}{2}(c'_i - r'_i) \frac{d_{shift}}{a} \quad (3.3)$$

where r'_i is the component i of initial center position of particle, c'_i the component i of center of unit cell, a the edge length of unit cell and d_{shift} a dimensionless parameter which controls the amount of displacement. If d_{shift} was positive the particles were shifted towards the center of the unit cell which corresponded to agglomeration (Fig. 3.9b). If d_{shift} was negative the particles were shifted towards the sides of the unit cell which corresponded to pore formation (Fig. 3.9a).

The effect of particle size was studied using a bimodal distribution of the particles with two different sphere diameters. The arrangement of the particles was either homogeneous (smaller particles were surrounded by larger particles or vice versa), or inhomogeneous (the smaller particles were in the center of the super cell and the larger

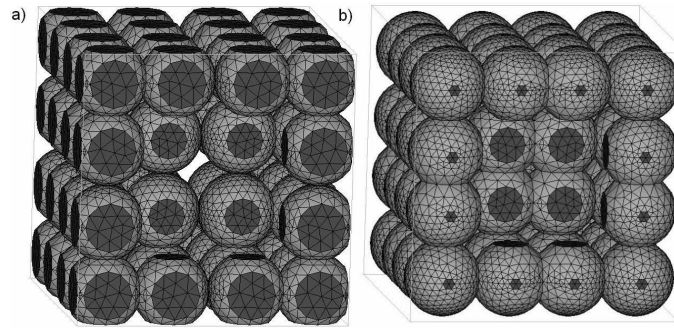


Figure 3.9: Cubic structures with truncated spheres shifted towards (a) the sides and (b) the center of the unit cell. Some particles were removed to get a better view of the microstructure and the contact areas are represented with the dark gray color

particles at the edges). In Fig. 3.10 two different super cells with 64 particles and homogeneous or inhomogeneous arrangement of particles are shown. The different arrangement is supposed to reflect different attractive and repulsive forces between the smaller and larger particles during the forming process.

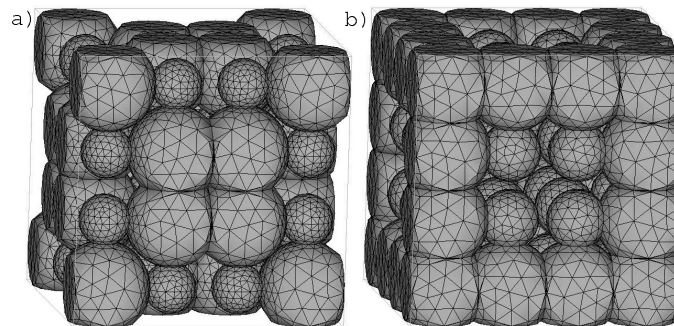


Figure 3.10: Cubic structures with (a) homogeneous and (b) inhomogeneous arrangement of small and large particles

All the structures mentioned up to now have 6 nearest neighbors. In the following, structures derived from bcc and fcc lattices with 8 and 12 nearest neighbors have been considered (Fig. 3.11). This way the influence of the coordination number on the material properties could be investigated. Therefore, the number of nearest neighbors used in simulation covered the range of nearest neighbors observed in green compacts (6–8) and sintered materials (12–14) [Ger96]. Particle size, displacement and number of nearest neighbors could be varied at the same time without violating the cubic symmetry of the super cell.

Random structures

Random structures were derived from a Poisson distribution of spheres centers within a cube. Initial center positions were obtained by a standard random number generator.

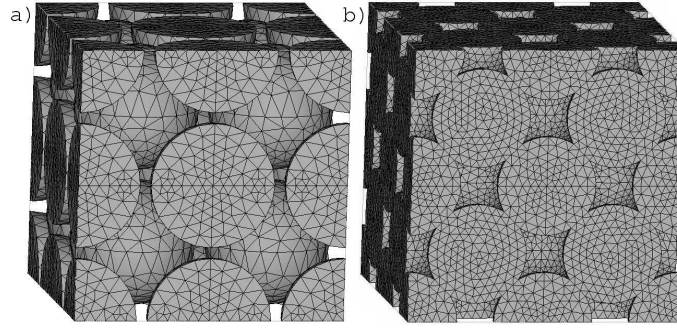


Figure 3.11: Cubic structures with (a) 8 and (b) 12 nearest neighbors (bcc and fcc structures, respectively)

Typically four to eight initial spheres were used for one microstructure. Particle compaction was considered by starting with a large unit cell and subsequently reducing its size by an affine transformation of the particle centers. The centers of contacting spheres were shifted by an individual displacement vector for each sphere, which was calculated from all its contacts, to prevent overlap with neighboring spheres. When density was high enough, the movement of the spheres was restricted by other contacts. Then overlapping of spheres was allowed and the total elastic energy of all spheres within the unit cell was minimized by applying a common scaling factor to the individual displacement vector. The scaling factor was between 0 (soft sphere limit) and 1 (hard sphere limit). Elastic energy was determined from the sum of the local energies determined by contact area and sphere radii [Wal87]. According to Gusev et al. [Gus00] periodic boundaries were introduced by shifting those parts of spheres, which lay outside the cube to the respective opposite sides of the cube (see Fig. 3.12a). This increased the total number of spheres to 14 – 30 within the unit cell.

In order to better describe two bi-continuous crystalline phases a *Voronoi model* is used. The microstructure is produced from a Poisson distribution of particle centers within the unit cell where the center positions are obtained by a standard random number generator. The two phases are attributed randomly to the center points according to their volume fractions and grain size ratios. The center points are periodically continued in the neighboring unit cells. Then the Voronoi tessellation is performed by constructing polyhedra which separate regions closest to each center point. Actually a modification of this procedure based on radial planes is used to consider different grain sizes of the two phases. The algorithm is described in Ref. [Gel82]. A typical Voronoi structure is presented in Fig. 3.12b.

The random structures were produced by using the *Geosphere* software. It enables the generation of structures with additional specified geometric properties, like a fixed average number of contacts per particle (see Fig. 3.13) or contact area, by generating and testing thousands of structures until the required properties were met. Since many structures had to be generated to find one valid structure the computational effort for generating the random structure was much higher than that for super cells. Sintering necks were constructed as planes defined by the circular edge of the overlap region of

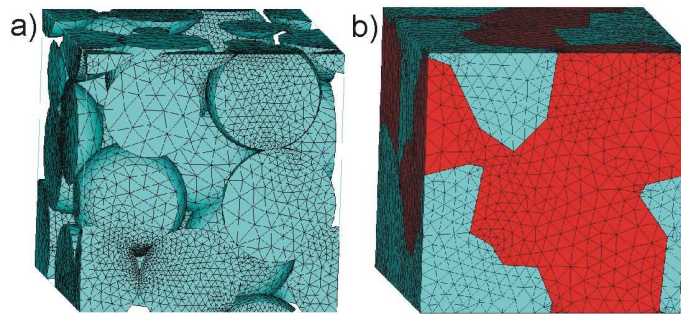


Figure 3.12: Random structures with periodic boundaries: (a) truncated spheres and (b) Voronoi polyhedra

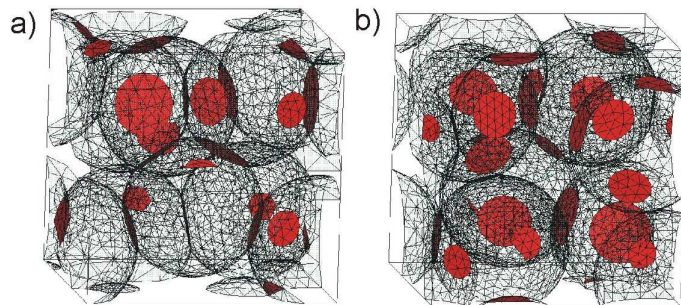


Figure 3.13: Random structure of spherical particles with (a) 4.75 and (b) 7.5 contacts per particle. Here the solid particles are transparent and the contact areas are represented with the grey/red color

two spheres. To avoid conflicts, the structures, where the center of a sphere lays within another sphere were not considered.

Some geometric data were derived from the microstructure. Most important were the interface areas between pores and solid phases, or between the two solid phases and the neck area at the particle contacts. Also the minimum solid area perpendicular to the flux or force direction was derived (according to the minimum solid area approach [Ric89]). Finally, a chord length analysis was performed by randomly selecting the starting point and direction of 10,000 test lines within the microstructure and determining the volume fractions of different phases, the number of interfaces and the mean value of the squared solid chord lengths. The volume fraction of the phases (solid-solid or solid-pores) and the number of interfaces from chord length analysis were used to control and match the microstructure to the experimental one. The mean value of the squared solid chord lengths c_{s^2} was used as a measure for the length of force transmission:

$$c_{s^2} = \frac{\sum_i c_i^2}{\sum_i c_i} \quad (3.4)$$

with c_i the chord length of individual particles. The homogeneity of the microstructure was measured by an auto-correlation parameter c_a , which was calculated by summing up the products of the chord lengths of neighboring particles:

$$c_a = \frac{\sum_i c_i c_{i-1}}{\sum_i c_i^2} \quad (3.5)$$

3.2.2 Finite element mesh and boundary conditions

In order to ensure that the regions with a fine structure (e.g. contact region at small sintering necks) are meshed with a sufficiently large number of elements, first a 2D grid was performed. Different areas, like contact areas, interface areas between solid and pore phase, side areas of the unit cell, were meshed applying a 2D surface element and using a fixed number of nodes (typically between 6 and 10) at line segments within the microstructure. The different phases were then discretized using 3D ANSYS elements, SOLID87 and SOLID187 for thermal and mechanical simulations, respectively. Contact (CONTA174) and target (TARG170) elements were used to take into account the thermal resistance at grain boundaries and to evaluate the normal stresses at the interfaces between different grains. The bulk material properties (thermal conductivity, Young's modulus, Poisson ratio etc.) were attributed to different phases.

In the cubic structures the calculations of the thermal properties have been performed by setting a temperature gradient at two opposite sides of the unit cell and applying adiabatic boundary conditions to the four remaining sides. The thermal conductivity λ was averaged at one side with fixed temperature and calculated from the heat flux Q by: $\lambda = Q/(a \cdot \nabla T)$. Here a is the edge length of the unit cell and ∇T is the temperature difference at the opposite sides of unit cell.

In order to obtain the elastic properties of structures with cubic symmetry an uniaxial tensile strain was applied. On the two opposite sides of the unit cell a small amount of strain ϵ is applied, whereas a constraint on the other sides ensured that they remained

plane during the tension. The Young's modulus, E , is calculated from the resulting stress σ determined at one of the two strained sides (see Fig. 2.1c). From the resulting strain at the perpendicular sides, the Poisson's ratio was calculated (see Fig. 2.1c). Always linear elastic behavior was considered as described by Hook's law (Eq. (2.8)). The shear modulus G was determined by applying a simple shear strain and calculating from the resulting shear stresses τ according to formula $G = \tau/\varphi$ (see Fig. 2.1b).

For the random microstructures, loads were applied in different directions. For heat flow the symmetric thermal conductivity tensor λ_{ij} was determined by applying temperature gradients parallel to the edges of the unit cell. In Fig. 3.14 one can see the cycle of a thermal simulation in one (of three) direction. For stress simulations both tensile

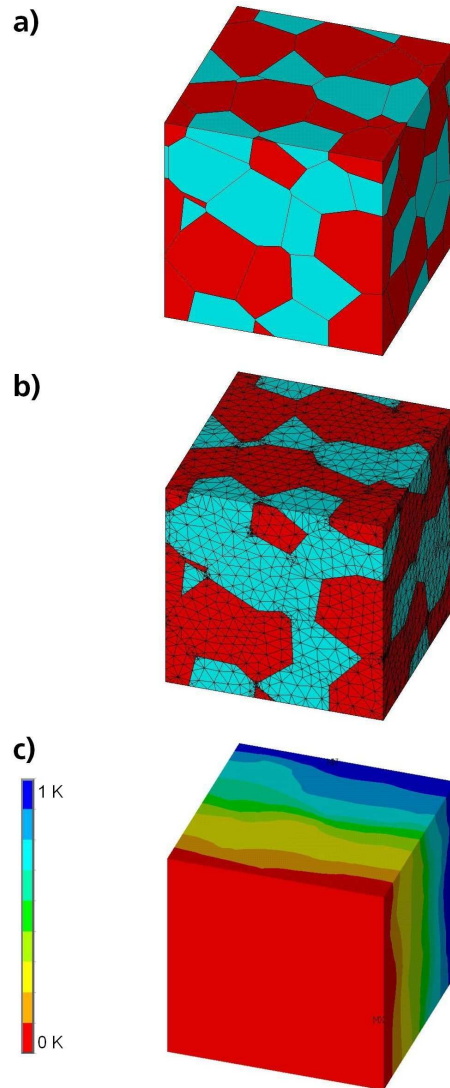


Figure 3.14: (a) The microstructure, (b) the mesh and (c) the temperature field as a result of simulation

and shear strains were applied in different directions to determine the 21 independent

elements c_{ij} (with $i \leq j, j \leq 6$) of the symmetric stiffness matrix.

Stress, strain, heat flow and temperature gradient were determined from the FE solution by calculating the weighted average over all elements within the unit cube:

$$S = \frac{\sum_i S_i v_i}{a^3}$$

with S the respective quantity, v_i the volume of element i , a the edge length of unit cell. The system of linear equations (2.8) was solved by an in-house developed software, *Crystal* (Raether, Fraunhofer ISC) using singular value decomposition SVD [Pre89]. A number of 3 and 6 simulations with different loads were required for each structure to determine all λ_{ij} and c_{ij} respectively. Using *Crystal* the elasticity and thermal conductivity tensor was diagonalized.

From the λ_{ij} and c_{ij} the polycrystalline material properties E and ν were estimated by performing an additional simulation: the unit cell was replaced by a single hexagonal element of a homogeneous anisotropic material (SOLID70 and SOLID185 for thermal and mechanical simulations respectively). Thermal or elastic material properties were set to the values obtained for the respective unit cell. Then a large cube was constructed from $10 \times 10 \times 10$ of such elements where the orientation of each element has been randomly chosen. The material properties of the large cube were determined by applying loads as described for the small unit cell. Nearly isotropic behavior was obtained and computation time was less than one minute for this last step of the simulation. All data obtained from this polycrystal simulation were within the range of the Hashin-Shtrikman and Voigt-Reuss-Hill approximation respectively.

The stress concentration factor f_σ was calculated from the ratio of the maximum principal tensile stress σ_{1max} within the unit cell of the applied tensile stress σ :

$$f_\sigma = \frac{\sigma_{1max}}{\sigma} \quad (3.6)$$

Since stresses were largest at the edge of the particle contacts, the stress concentration factor was actually determined by averaging the first principal stress at all nodes at the edges of individual contacts and selecting the maximum of these averaged values.

The FE solution was obtained by searching the minimum of the quadratic functional of the system using a Conjugate Gradient method, i.e. the solutions for the degrees of freedom (DOF) were calculated by iterating the system equations to convergence, starting with an assumed zero value for all DOFs and following orthogonal residual vectors. Computing time was about 5 minutes for one direction of applied strain or thermal gradient.

3.2.3 Convergence and verification

The simulations have been performed using ANSYS on a PC work station (Intel Pentium 4 Xeon 2.8 GHz). Fig. 3.15 shows the convergence of the FEM results when mesh size was decreased by increasing the number of nodes on the line segments of the model. A sufficient convergence for thermal conductivity, Young's modulus and Poisson's ratio was achieved within 2% with a mesh size corresponding to 6 to 10 nodes. The convergence

for the stress concentration factor was distinctly worse which was attributed to its local determination in regions showing a very high stress gradient. Consequently, in the following sections stress concentration factors should be considered as a rough estimate. Altogether convergence was much better than in simulations with hexagonal elements. Although hexagonal elements are widely used, they were not appropriate to represent the fine structures at the particle contacts in the present study.

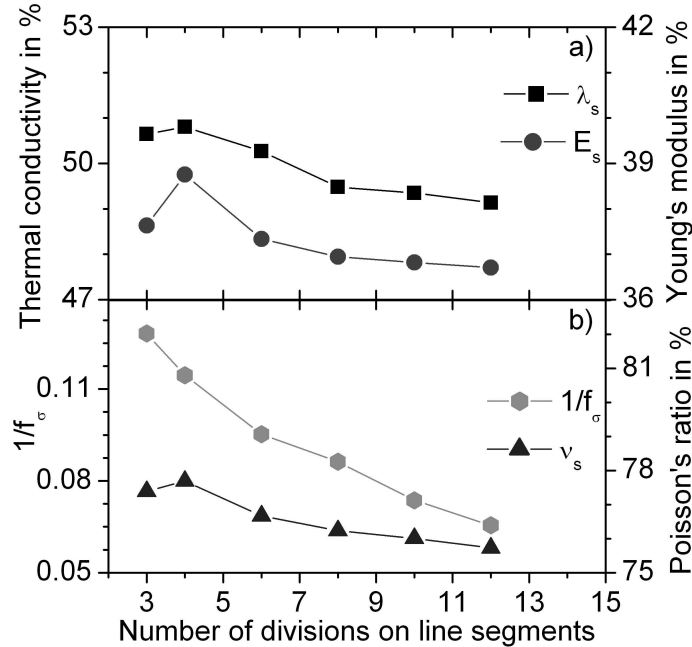


Figure 3.15: Convergence of FE simulations determined by variation of material properties with number of nodes on line segments for simple cubic arrangement of truncated spheres ($f_s = 70\%$): (a) scaled thermal conductivity λ_s and Young's modulus, E_s and (b) inverse stress concentration factor $1/f_\sigma$ and Poisson's ratio ν_s

In Fig. 3.16 the convergence of the FEM results for random structures is illustrated. In this case the mesh size was influenced by using another type of parameter, called grid refinement, GR. Here a linear trend for thermal conductivity, Young's modulus and Poisson's ratio was observed. The convergence was achieved within 2%, with a mesh size corresponding to $GR = 0.2$. Note that in Figs. 3.15 and 3.16 and the following figures, scaled material properties are used (given in %), which means that the respective property of the solid phase corresponds to 100%.

For spherical particles with very small contacts analytical solutions exist for thermal conductivity [Kav91] and elastic properties [Wal87], [Wal75]. Fig. 3.17 shows a comparison of our FE simulation with the analytical results. To be noticed that a scaled area was used which was calculated by dividing the two particle contact area by the side areas of the cube. The excellent agreement demonstrates that the FE model was appropriate for the simulation of structures with very small particle contacts. Unlike the other figures that show polycrystalline results obtained by the FE method described

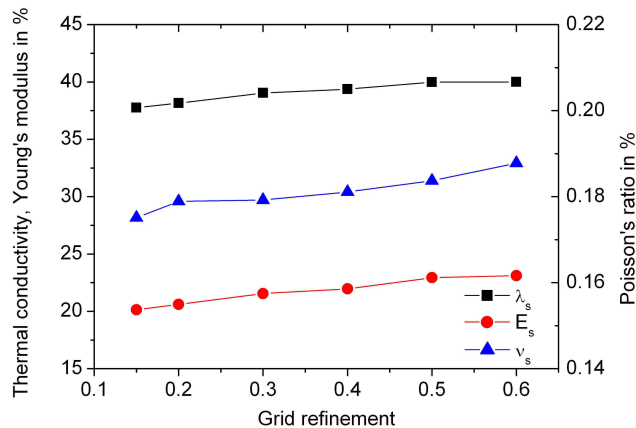


Figure 3.16: Convergence of FE simulations as a function of grid refinement, GR for random arrangement of truncated spheres ($f_s = 70\%$): scaled thermal conductivity λ_s and Young's modulus, E_s and Poisson's ratio ν_s

in the previous paragraph, Fig. 3.17 shows single crystal material properties in the [100] direction.

To avoid handling errors the simulations were performed completely in batch mode. Geometric properties of the model were controlled twice after generating the model and after meshing. If deviations were detected between solid volume fraction, particle contact areas or interface areas to those values determined by the independent computer program *Geosphere*, which had generated the structures, the simulation was automatically aborted.

3.3 Experimental procedure

3.3.1 Quantitative image analysis

In order to evaluate the microstructures, it is necessary to make a quantitative analysis that means to accumulate data needed to formulate a quantitative description of the properties from the microstructure. There are many methods to perform a quantitative image analysis, like point, lineal or area analysis [Exn88]. In this work, the samples were investigated using the lineal analysis (see Fig. 3.18). In lineal analysis, the intercept lengths are measured along randomly applied straight lines across the microstructure. The individual lengths intercepted by particles or two-phase regions are measured separately, added up, and compared to the total lengths of traverse. The ratio L_L is determined for a particular selected phase. The volume fraction of a phase can be determined from the data obtained by lineal analysis. Within the limit of scatter, the volume fractions are equivalent to the lineal fractions:

$$V = L_L$$

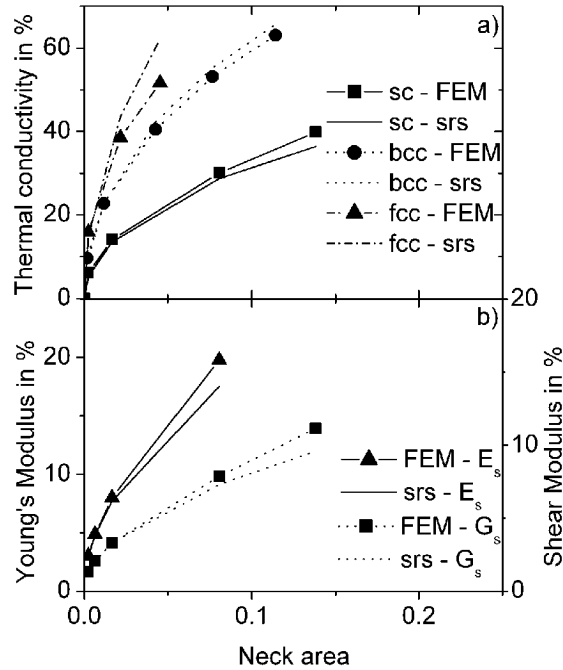


Figure 3.17: Comparison of material properties calculated by FE model and theoretical small radii solutions (srs): (a) scaled thermal conductivities for sc, bcc and fcc structures and (b) scaled Young's and shear moduli for simple cubic arrangement (srs) equations from [Kav91], [Wal87], [Wal75]

In order to determine the interface areas the number of intersections made by the traverse with phase boundaries or grain boundaries is counted. So, the fraction of boundary areas in a structure is given by:

$$B_A = \frac{N_{P_o}}{N_P}$$

where N_{P_o} represents the number of point interceptions of an object, N_P represents the total number of point interceptions on a test line. The term *object* is related in this case to grain boundaries or phase boundaries. This way volume fraction of component phases and interfaces between different grains could be determined and used as input for further simulations. A large contrast of the pictures is required to identify the grain boundaries. Therefore the sample preparation was carefully performed, i.e. the parameters for polishing and flame etching were always adjusted in order to obtain accurate micrographs.

3.3.2 Sample preparation

In Fig. 3.19 a general procedure concerning the sample preparation is presented.

As mentioned before, in this work we have concentrated on two types of systems, a porous Al_2O_3 ceramic and a dense ceramic, a zirconia-alumina (ZA) composite.

The starting powder used for the Al_2O_3 ceramic was Al_2O_3 powder of type Taimicron DAR (reported purity > 99.99%). The powder was equiaxed with an average particle diameter of $0.2 \mu\text{m}$. The green compacts were prepared by gel casting [Kre06]. For

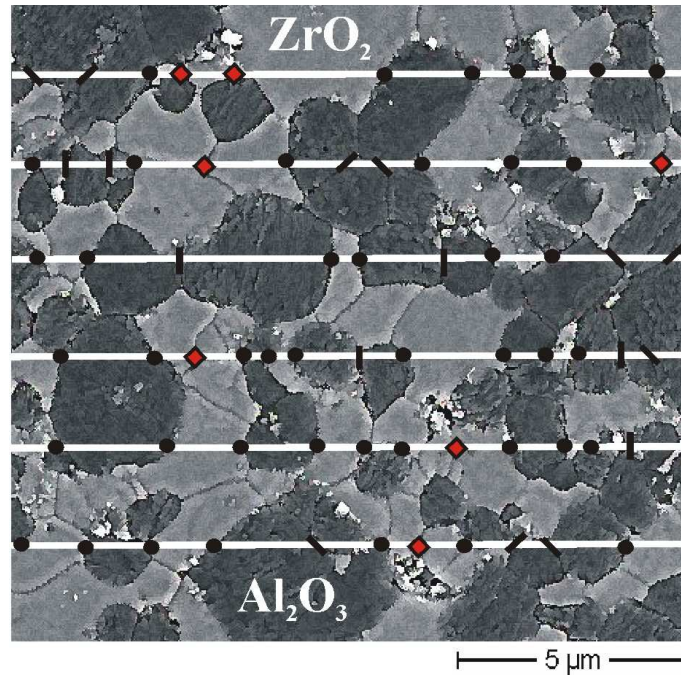


Figure 3.18: Microstructure of a ZA ceramic. Parallel lines along the structure is analyzed are indicated with white color. The circles mark the interfaces between alumina and zirconia grains, the segments the interfaces between alumina grains and the filled rhombus the interfaces between zirconia grains

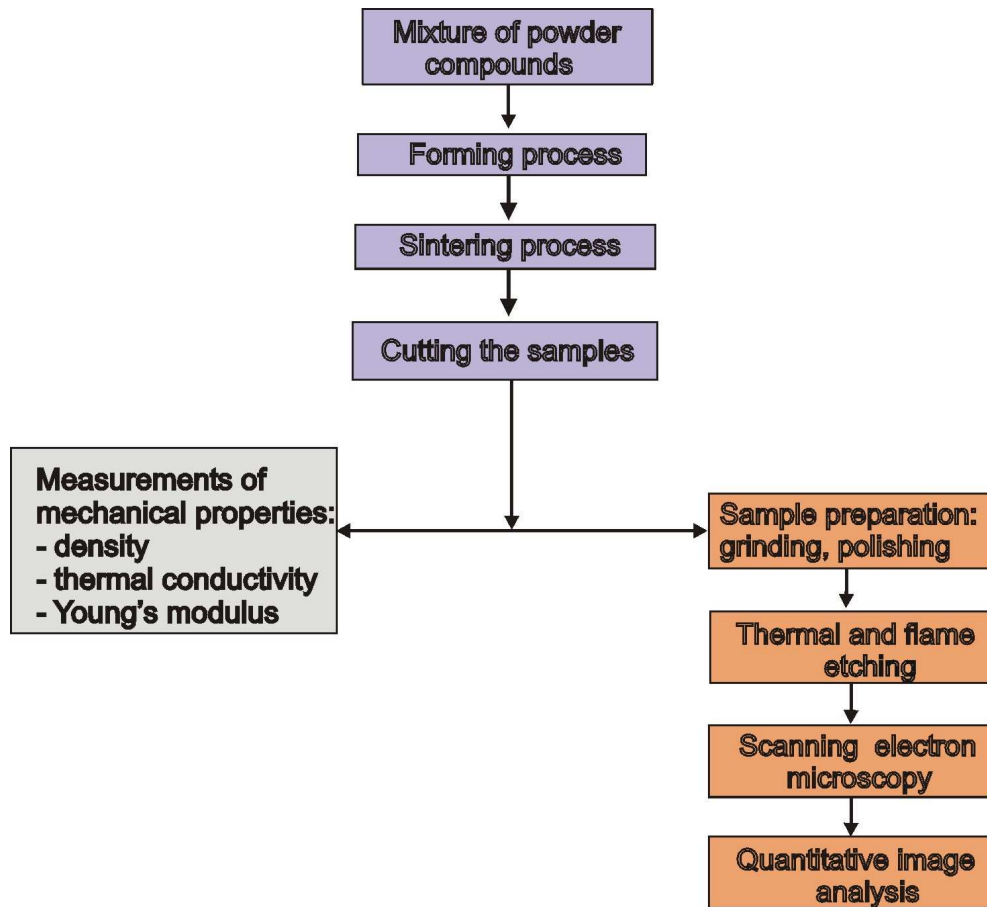


Figure 3.19: Flow chart describing experimental procedure of samples

the present study, samples partially sintered at temperatures between 800 and 1320°C with fractional densities between 58.4% and 97% have been used. For further steps, e.g. measurements of material properties and quantitative image analysis, the samples have been sawed, grounded and polished. In order to make the grain boundaries visible the samples were flame etched.

Fig. 3.20 illustrates the microstructure development of Al_2O_3 sintered at increasing temperatures (from 800 to 1350°C). Porosity decreased from 41.6% (Fig. 3.20a) to 3% (Fig. 3.20d) and at higher densities grain growth occurred. From the SEM images

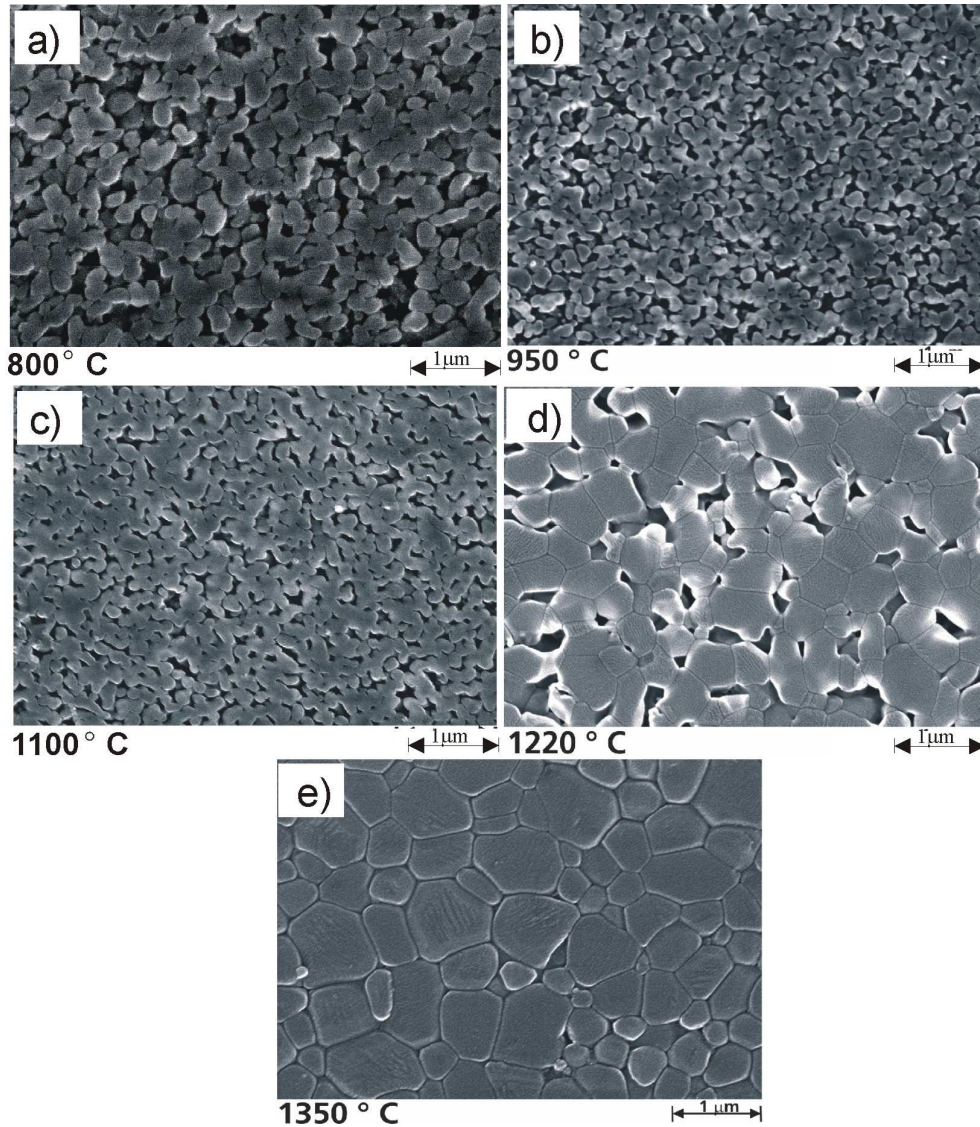


Figure 3.20: Aluminium oxide microstructure at different sintering stages

the interfaces between the Al_2O_3 grains and between Al_2O_3 grains and pores were determined from the number of intersections of random lines with the respective type of interfaces.

In case of ZA composite, the samples have been made by tape casting a slurry of alumina and zirconia powders. The zirconia powder was partially stabilized by 3 mol% Y_2O_3 and the ratio between zirconia and alumina was varied (e.g. 100 wt% Al_2O_3 , 98 wt% Al_2O_3 , 50 wt% Al_2O_3 , 2 wt% Al_2O_3 and 0 wt% Al_2O_3). The alumina and zirconia powders were equiaxed with an average particle diameter of about $0.83 \mu m$ and $0.8 \mu m$, respectively. The green compacts were dried and pressed cold isostatically (at 1500 kN), followed by sintering at temperatures between $1520^\circ C$ and $1550^\circ C$ for 2 hours. Finally the samples were prepared for SEM and measurements of material properties (sawing, grinding and polishing).

The microstructures of polished and flame etched sections of the ZA ceramic are shown in Fig. 3.21. Zirconia can be distinguished from alumina by its brighter coloring. In Fig. 3.21a, pure Al_2O_3 ceramic is presented. Fig. 3.21b and 3.21c show the 50 wt%

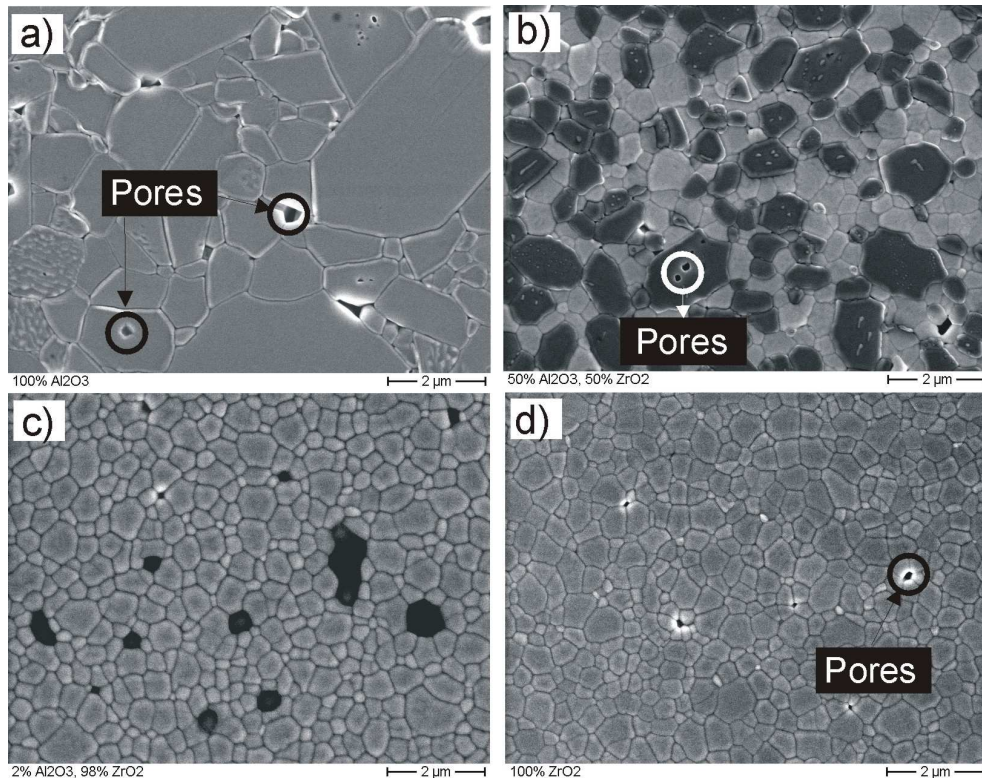


Figure 3.21: Microstructure of ZA ceramic with different alumina and zirconia volume fractions

Al_2O_3 - 50 wt% ZrO_2 and 2 wt% Al_2O_3 - 98 wt% ZrO_2 ceramics. Pure ZrO_2 is depicted in Fig. 3.21d. In all micrographs the interfaces between different grains (ZrO_2 - ZrO_2 , Al_2O_3 - Al_2O_3 and ZrO_2 - Al_2O_3) are readily recognized and could be measured using the chord length analysis. It can be observed that some of the pores are enclosed within the alumina grains (see 3.21a and b). Curvature of the grain boundaries is small. In 2 wt% Al_2O_3 - 98 wt% ZrO_2 sample the alumina grains are isolated and surrounded by zirconia grains. The same was observed in the case of 2 wt% ZrO_2 - 98 wt% Al_2O_3 sample,

alumina grains being surrounded by zirconia grains (not illustrated in Fig. 3.21). In the 50 wt% Al₂O₃- 50 wt% ZrO₂ the alumina and zirconia grains were homogeneously distributed, the alumina grains being larger than the zirconia grains.

3.3.3 Experimental measurements of thermoelastic properties

Thermal diffusivity of samples was measured by the laser-flash method [Rae98a] at room temperature. Usually disk shaped samples with a diameter between 11 and 20 mm and a thickness of 1 mm are used. The wavelength of the CO₂ used laser is 10.6 μm. The pyrometer filters, which measure the temperatures, have a wavelength above 11 μm. Therefore a special coating of the samples is avoided and thermal properties are measured completely non-contact. The thermal diffusivity values were determined by averaging 10 individual measurements. Measuring uncertainty (1 σ) was 4%. From thermal diffusivity χ, thermal conductivity λ is calculated according to following formula:

$$\lambda = \rho c_P \chi \quad (3.7)$$

with ρ being the density and c_P the specific heat of the sample. In case of composites c_P was calculated by a rule of mixtures:

$$c_P = c_{P_1} \cdot f_1 + c_{P_2} \cdot f_2, \quad (3.8)$$

where c_{P₁}, c_{P₂} and f₁, f₂ are the specific heat and fractional volume of component phases (1 and 2). Densities of the ceramic samples were measured using Archimedes principle. The samples with open pores were first degassed, then submerged in water under vacuum and weighted submerged to obtain the wet weight. The samples were then dried in a desiccator and the dry weight was determined with an analytical balance. Porosity was determined by the difference between theoretical density calculated from the density of the participating phases and measured density.

Young's modulus of the samples was determined by ultrasonic velocity measurement (USIP12, Krautkrämer, Hürth, Germany). Samples in the form of disks with 11 to 20 mm in diameter and 1 mm thick have been used. Young's modulus, E, was calculated according to formula:

$$E = \frac{(1 + \nu)(1 - 2\nu)}{(1 - \nu)} \rho v_P^2 \quad (3.9)$$

where ν represents the Poisson's ratio, ρ the sample density and v_P the longitudinal ultrasonic velocity. Measuring uncertainty of Young's modulus was about 1%.

Experimental data for pure Al₂O₃ and ZrO₂ doped with 3 mol% Y₂O₃ used to simulate the thermoelastic properties of alumina and ZA ceramics are summarized in Table 3.3. Note that the properties from Table 3.3 correspond to the dense (without pores) respective material.

Table 3.3: Experimental data for alumina and zirconia: density ρ , specific heat c_P , thermal conductivity λ , Young's modulus E , Poisson's ratio ν and coefficient of thermal expansion α

	ρ [g/cm ³]	c_P [J/g*K]	λ [W/m*K]	E [GPa]	ν	α [1/K*10 ⁶]
Al ₂ O ₃	3.989 ^a	0.78 ^a	29 ^a	390 ^a	0.22 ^a	9.1 ^a
ZrO ₂	6.081 ^b	0.46 ^b	3.1 ^b	220 ^b	0.3 ^b	12.2 ^b

^a Ref. [Dor84]; ^b Ref. [Gre89]

Chapter 4

Results and discussions

4.1 Quantum mechanics (QM) simulations

In this section, the results concerning the ab-initio computations based on density functional theory for ten ceramic systems are presented. Both, energy-volume equation-of-state computations to obtain the zero pressure equilibrium volume and bulk modulus as well as computations of the full elastic constant tensor of these ceramics at the experimental zero pressure volume have been performed.

4.1.1 Equation of state

DFT based computations using LDA typically overbond compounds and hence predict equilibrium volumes smaller than in experiment. GGA corrects from this and usually better agreement with experiment is obtained. Overall good agreement of the zero pressure volume computed with that in experiments (Table 4.1), was found within 4% of one another. Only the TiO_2 phases have a zero pressure volume that is larger than in experiment, with GGA overcorrecting the LDA shortcoming. The situation for the compression behavior and hence the bulk modulus is less satisfying (Table 4.1). While for most ceramics studied the computed bulk modulus (at computed zero pressure volume) is within 10% of ambient condition experiments the one for TiO_2 anatase is larger by almost 25% and for $\alpha\text{-SiC}$ by 16%. These values are considerably larger than computational results previously reported in the literature which use energy-volume relations to fit an equation of state [Arl00], [Kae94]. These studies, however, use a Hartree-Fock formalism or the LDA approximation to exchange and correlation, respectively. Due to the restricted volume range considered in the computations (Table 3.2) we find $B'_0 = 4.0$ in all computations. The consideration of a wider compression range would change this parameter.

4.1.2 Elastic constants

Individual elastic constants (evaluated at the experimental zero pressure volume) can differ significantly between computations and experiment, but these differences are hard

Table 4.1: Equation of state parameters of the ceramic compounds. The first line of the table gives fit parameters for the computational results for the zero pressure volume (V_0), the bulk modulus (B_0) at this pressure and its pressure derivative (B'). Calculated results (given in the first line of respective material) are compared with experimental equation-of-state parameters (see the second line written with italic characters)

	V_0 [Å ³]	B_0 [GPa]	B'_0
Al ₂ O ₃	82.0 <i>84.9</i>	241 <i>254^a</i>	4.0 <i>4.3^b</i>
α -SiC	79.6 <i>82.4</i>	260 <i>224^c</i>	4.0 -
β -SiC	79.4 <i>82.2</i>	220 <i>220^d</i>	4.0 -
TiO ₂ rut	63.4 <i>62.5</i>	235 <i>212^e</i>	4.0 <i>6.3^f</i>
TiO ₂ anat	138.3 <i>135.5</i>	221 <i>179^g</i>	4.0 <i>4.5^g</i>
CaF ₂	41.6 <i>41.6</i>	78 <i>81^h</i>	4.0 <i>5.2^h</i>
AlN	39.8 <i>40.8</i>	210 <i>211^{i,j}</i>	4.0 <i>6.3^{i,j}</i>
BN	46.3 <i>47.2</i>	362 <i>400^{k,j}</i>	4.0 <i>4.5^{k,j}</i>
TiB ₂	25.2 <i>25.5</i>	251 <i>237^{l,m}</i>	4.0 <i>2.0^{l,m}</i>
ZrO ₂	142.4 <i>140.5</i>	174 <i>187ⁿ</i>	4.0 -

^a Ref. [Got89]; ^b Ref. [Dam78]; ^c Ref. [Kam97]; ^d Ref. [Hea84]; ^e Ref. [Isa98]; ^f Ref. [Man69]; ^g Ref. [Arl00]; ^h Ref. [Ang93]; ⁱ Ref. [Mcn93]; ^j Ref. [Kim96]; ^k Ref. [Gri94]; ^l Ref. [Spo97]; ^m Ref. [Dan93], ⁿ Ref. [Cha91]

to quantify for all the materials studied (Table 4.2). Instead of considering them separately the results were quantified by computing the average moduli according to Hill (arithmetic means of the Voigt and Reuss bounds) [Voi28], [Reu29], [Hil52] from the individual elastic constants (Table 4.2). We obtain bulk and shear moduli for all materials considered (Fig. 4.1). In addition we have computed the anisotropy ratios for the longitudinal (c_{22}/c_{11} and c_{33}/c_{11}) and shear (c_{55}/c_{44} and c_{66}/c_{44}) elastic constants (Fig. 4.2). These ratios are a measure of the relative propagation of the longitudinal and transverse acoustic waves along the crystallographic axes, respectively.

For the bulk modulus derived from the elastic constant tensor (Fig. 4.1a, Table 4.2) we find much better agreement (within 5%) with experiment than for that from the equation of state. This better agreement justifies and suggests the use of the experimental zero pressure volume to evaluate elastic parameters of materials rather than the computational equilibrium volume. Similar to the bulk moduli, the shear moduli determined from the computations are in overall good agreement with experiment, with a maximum deviation of 10% (or 20 GPa) for the SiC polytypes (Fig. 4.1b, Table 4.2). Typically we find that the shear moduli of the stiffer materials are overpredicted, while those of the softer materials are underpredicted.

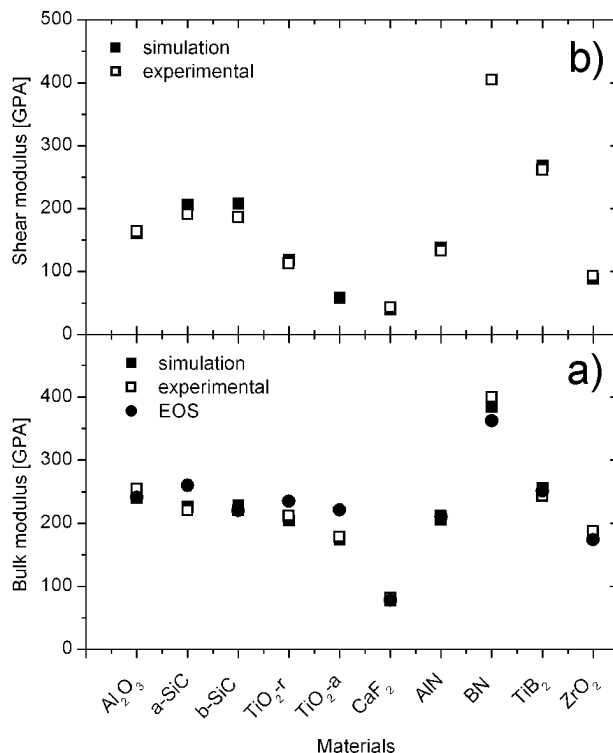


Figure 4.1: (a) Bulk and (b) shear moduli calculated from elastic constant tensor

The comparison of anisotropy ratios between experiments and computations provide a similarly good picture (Fig. 4.2). Regardless the anisotropy type of the system, the correct sense of anisotropy (fast vs. slow propagation direction of acoustic waves) was correctly predicted. Similarly, the materials that show strongest anisotropy in experiment, TiO₂ rutile and ZrO₂ for shear anisotropy and TiO₂ rutile and TiB₂ for

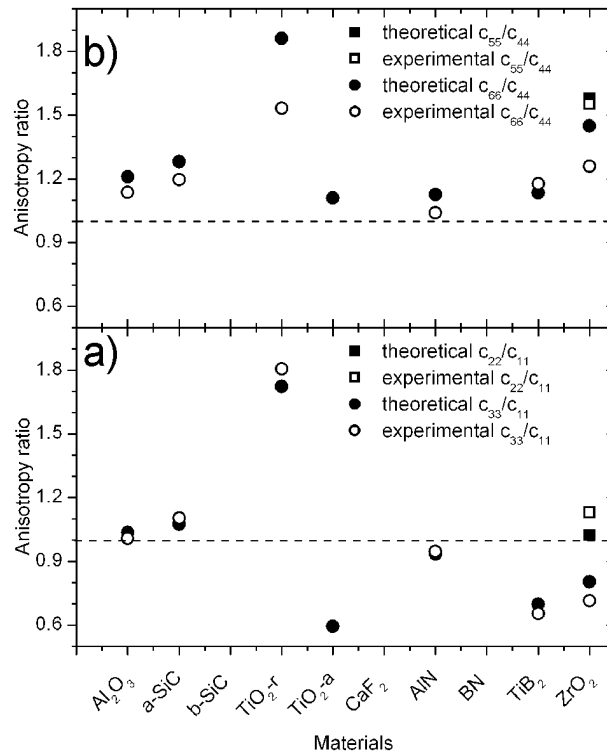


Figure 4.2: (a) Longitudinal and (b) shear anisotropy ratios

longitudinal anisotropy are predicted with the strongest anisotropy in the computations.

Conclusions

DFT based ab-initio calculations for elastic properties of a number of ceramic materials, Al_2O_3 , SiC, TiO_2 , AlN, BN, TiB_2 , CaF_2 , ZrO_2 have been carried out. The full elastic constant tensor at the experimental zero pressure volume was computed, and it was found that ab-initio methods with the GGA approximation are capable of reproducing the most important features in elastic behavior: the aggregate moduli as well as the general sense of anisotropy in longitudinal and shear moduli. These results show that modern ab-initio computations can be used independently from experiment to predict elastic stability, and can provide a basis for the modeling of structural and elastic properties of more complex composite ceramic materials.

Table 4.2: Elastic constants c_{ij} for studied ceramic materials. The first line of every material gives the computed data and the italic characters the experimental ones. The last two columns show the theoretical and experimental bulk and shear modulus

	c_{11}	c_{22}	c_{33}	c_{44}	c_{55}	c_{66}	c_{12}	c_{13}	c_{15}	c_{23}	c_{25}	c_{35}	c_{46}	B	G
Al ₂ O ₃	484 <i>497^a</i>		501 <i>501^a</i>	138 <i>147^a</i>		167 <i>167^a</i>	150 <i>163^a</i>	99 <i>116^a</i>	-27 <i>-22^a</i>					240 <i>254^a</i>	161 <i>164^a</i>
α -SiC	534 <i>501^b</i>		574 <i>553^b</i>	171 <i>163^b</i>		219 <i>195^b</i>	96 <i>111^b</i>	50 <i>52^b</i>						226 <i>220^b</i>	206 <i>191^b</i>
β -SiC	420 <i>379^c</i>			267 <i>252^c</i>			132 <i>141^c</i>							228 <i>220^c</i>	208 <i>186^c</i>
r-TiO ₂	278 <i>268^d</i>		479 <i>484^d</i>	115 <i>124^d</i>		214 <i>190^d</i>	153 <i>175^d</i>	149 <i>147^d</i>						204 <i>212^d</i>	118 <i>113^d</i>
a-TiO ₂	320 -		190 -	54 -		60 -	151 -	143 -						174 <i>178^e</i>	58 -
CaF ₂	155 <i>165^f</i>			31 <i>34^f</i>			39 <i>39^f</i>							78 <i>81^f</i>	40 <i>43^f</i>
AlN	413 <i>411^g</i>		386 <i>389^g</i>	126 <i>125^g</i>		142 <i>130^g</i>	129 <i>149^g</i>	96 <i>99^g</i>						205 <i>211^g</i>	138 <i>133^g</i>
BN	816 <i>820^h</i>			469 <i>480^h</i>			168 <i>190^h</i>							384 <i>400^h</i>	405 <i>405^h</i>
TiB ₂	671 <i>660ⁱ</i>		468 <i>432ⁱ</i>	269 <i>260ⁱ</i>		305 <i>306ⁱ</i>	62 <i>48ⁱ</i>	103 <i>93ⁱ</i>						256 <i>243ⁱ</i>	268 <i>262ⁱ</i>
ZrO ₂	341 <i>361^j</i>	349 <i>408^j</i>	274 <i>258^j</i>	80 <i>100^j</i>	73.4 <i>81.2^j</i>	116 <i>126^j</i>	158 <i>142^j</i>	88 <i>55^j</i>	29 <i>-21^j</i>	156 <i>196^j</i>	-4 <i>31^j</i>	2 <i>-18^j</i>	-14 <i>-23^j</i>	187 <i>187^j</i>	88 <i>93^j</i>

^a Ref. [Got89]; ^b Ref. [Kam97]; ^c Ref. [Hea84]; ^d Ref. [Isa98]; ^e Ref. [Swa01]; ^f Ref. [Cat78]; ^g Ref. [Mcn93]; ^h Ref. [Gri94]; ⁱ Ref. [Spo97]; ^j Ref. [Cha91]

4.2 Finite element simulations

In this section the results and discussions related to FEM simulations are illustrated. First, the investigation of the synthetic microstructures is depicted. Second, the results of structures adapted to two real ceramics, are presented and discussed.

4.2.1 Microstructure-property relations in synthetic structures

In Fig. 4.3 the resulting distribution of the heat flux and stress in a particle, which has been subjected to a thermal gradient and uniaxial tensile strain, respectively is presented. One can see that flux and stresses are largest in the contact region. Especially

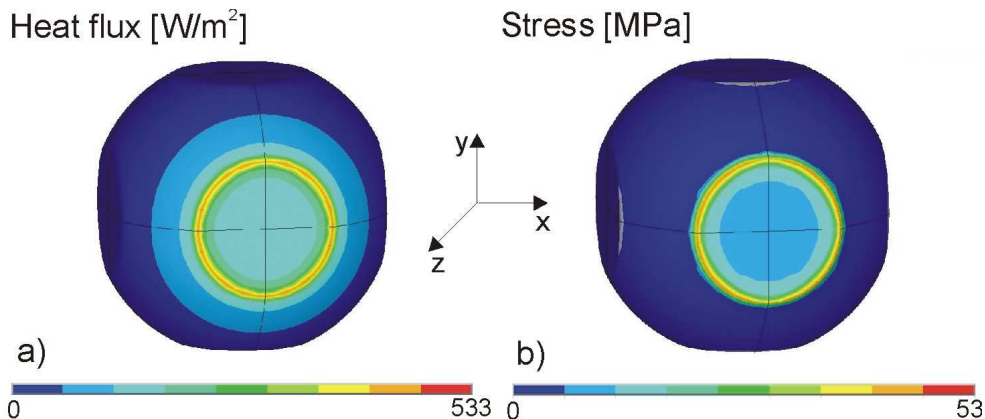


Figure 4.3: Contour maps of: (a) heat flux and (b) first principal stress. Temperature gradient and strain were applied in the z -direction

large values are observed at the edges of the sintering necks. This was already observed in previous work on the heat flow [Hah96]. The concentration of heat flux and mechanical stress at the edges of the particle contacts was observed for various particle shapes and arrangements investigated during this work.

Different particle shapes

As mentioned previously, different solid particle shapes have been considered in order to study the influence of various contact areas on material properties. The corresponding shapes are shown in Figs. 3.5-3.8.

Fig. 4.4 depicts simulated thermal conductivity, Young's modulus, Poisson's ratio and stress concentration factor for these particles. Here the solid volume fraction was always 70% and the arrangement of the particles within the unit cell was simple cubic. For comparison also a simple cubic microstructure with 30% closed spherical pores was considered. In this case the *contact area*, which corresponds to the *minimum solid area*, was much higher than for the other structures.

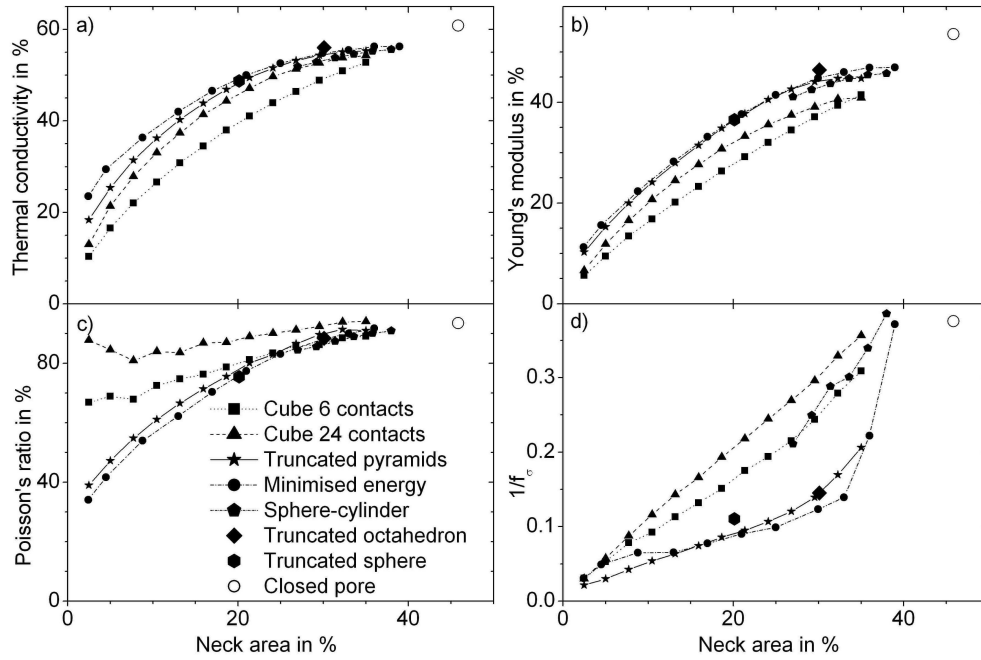


Figure 4.4: Material properties of different particle shapes at constant solid volume fraction of 70%: (a) scaled thermal conductivity, (b) scaled Young's modulus, (c) scaled Poisson's ratio, (d) inverse stress concentration factor

The differences in the thermoelastic properties of particles with different shapes (see Figure 3.5, 3.7 and 3.8) are very small. Only the structure depicted in Fig. 3.6a shows considerably lower thermal conductivity and Young's modulus than the others. However, from the convex curvature of the FEM curve it can be seen that there are quantitative differences (the minimum solid area approach would yield a straight line through the origin with slope 1). It can be explained looking at the concentration of the heat flux and stress at the edges of the particle contacts (see Fig. 4.3). This allows for a larger heat and force transfer (especially with small particle contacts) than it would be expected from purely geometrical considerations. One can see from Fig. 4.4a and 4.4b that the curvature of the Young's modulus is smaller than that of the thermal conductivity. The steeper increase at small particle contacts for thermal conductivity corresponded to the larger gradient in heat flux across the particle contact compared to the stress gradient.

From Fig. 4.4c it can be seen that the Poisson's ratio does not tend to zero with decreasing contact area. For the cube structure with 24 cylindrical contacts (3.6b) the Poisson's ratio is even nearly independent of contact area. Other groups have suggested a convergence of the Poisson's ratio to finite values with decreasing contact area [Ram93], [Rob00] which has been controversially discussed based on different experimental [Boc94] and theoretical [Ric94] results.

The stress concentration factor f_σ (Fig. 4.4d) has very high values at small contact areas. This corresponds to the inferior strength of porous compacts during the first sintering stage. For structures with cylindrical contacts (see Fig. 3.5c, 3.6a and 3.6b), a

distinctly smaller stress concentration at medium contact areas could be observed. This was attributed to the more homogeneous distribution of stress along the cylindrical contacts compared to the notched contact regions of the other particle shapes. The particle shapes with minimized energy show a steep increase of $1/f_\sigma$ when neck area exceeds 30%. This was correlated to a similar increase of the dihedral angle which leads to a smoothing of the particle surfaces in the contact region (see Fig. 3.8c).

Different particle arrangement

Besides the influence of particle shapes on thermoelastic properties the effect of different particle arrangements within the unit cell was also investigated. Aspects like agglomeration or large pore formation could be studied by applying a displacement to the centers of the truncated spheres (Fig. 3.9). The effect of different particle sizes was considered (see Fig. 3.10). The influence of the coordination number on material properties was investigated using structures with different number of nearest neighbors (Fig. 3.11).

Fig. 4.5 shows the effect of particle displacement in a cubic super cell with 64 spherical particles and a solid volume fraction of 70%. The corners and the center of the unit cell changed their role as nucleation center for agglomerates. In this way the displacement of the particles towards the center has the same effect as a displacement with the opposite sign. By increasing the displacement, thermal conductivity, Young's modulus and Poisson's ratio will decrease (Fig. 4.5a). This can be explained qualitatively by the formation of a matrix with weakly bonded particles in which the agglomerates of more strongly bonded particles were embedded.

Fig. 4.5b and 4.5c present various geometric properties of microstructures. The number of contacts per particle was six for all shown displacements. As a measure of the geometrical change the ratio, a_s , of total contact area to total interface area (i.e. $a_s = a_c/(a_c+a_i)$, where a_c is the total neck area and a_i the total pore-solid interface area) within the unit cell was used. In this case the particle contacts within one microstructure have different sizes and the scaled neck area could not be used. The parameter a_s is dimensionless and independent of the size of the unit cell. It showed a small increase of contact area with increasing particle displacement. This reflected the non-linear increase of contact area with decreasing center distance of spherical particles. In Fig. 4.5c also the squared solid chord lengths c_{s^2} , the auto-correlation parameter c_a and the minimum solid area (MSA) are shown. MSA decrease with increasing displacement and decreasing material properties according to the minimum solid area approach.

Fig. 4.6 shows the effect of different particle size ratios in the cubic super cell with 64 spherical particles and a solid volume fraction of 70%. The particle size ratio was defined as the ratio of the volumes of a large and a small particle, respectively. The thermoelastic properties for a homogeneous arrangement of large and small particles (see Fig. 3.10a) vs. the particle size ratio are depicted in Fig. 4.6a and the corresponding geometric parameters in Fig. 4.6b and c. At a size ratio between 1 and 2.5 a decrease of thermal conductivity and Young's modulus could be observed. The inverse stress concentration factor showed a pronounced decrease at this size ratio (Fig. 4.6b). This was correlated to a decrease in the average number of contacts per particle (see Fig. 4.6c), caused by vanishing particle contacts between neighboring particles of the small size category.

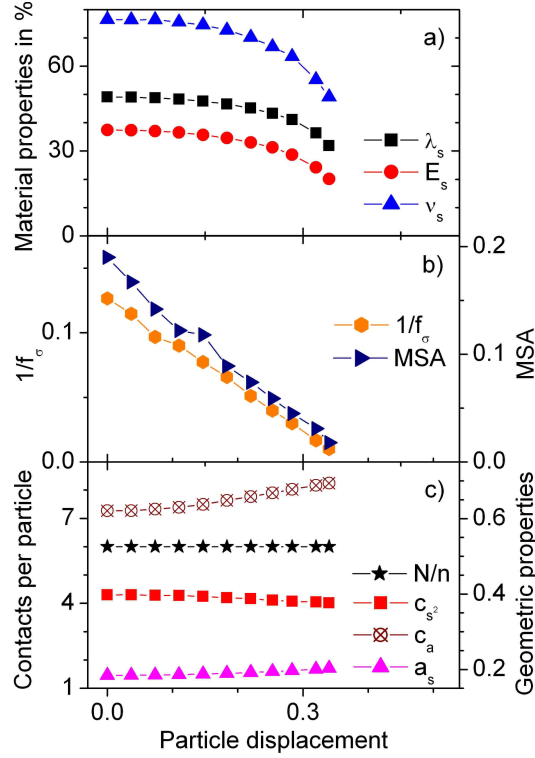


Figure 4.5: Properties of cubic structures at different displacements of truncated spherical particles and constant solid volume fraction 70%: (a) scaled thermal conductivity λ_s , Young's modulus E_s and Poisson's ratio ν_s , (b) related inverse stress concentration factor $1/f_\sigma$ and minimum solid area MSA, (c) contacts per particle N/n , average squared solid chord length c_{s^2} , auto-correlation parameter c_a and ratio between total contact area and total interface area a_s

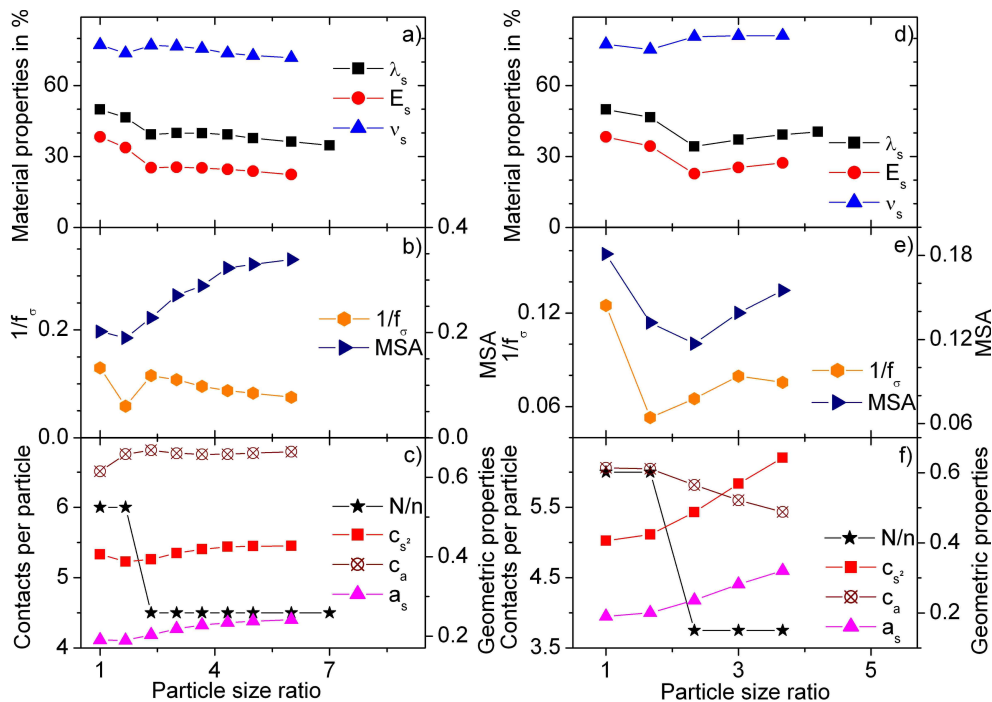


Figure 4.6: Properties of cubic structures at different size ratios of truncated spherical particles and constant solid volume fraction 70%: (a) scaled thermal conductivity λ_s , Young's modulus E_s and Poisson's ratio ν_s , (b) related inverse stress concentration factor $1/f_\sigma$ and minimum solid area MSA, (c) contacts per particle N/n , average squared solid chord length c_{s^2} , auto-correlation parameter c_a and ratio between total contact area and total interface area a_s , (d) material properties for particles arranged inhomogeneously, (e) related inverse stress concentration factor and MSA and (f) related geometric properties

The high stress concentration at this size ratio was attributed to the smallest particle contacts. Stress concentration decreased after these contacts were released.

In Fig. 4.6d, e and f the results for an inhomogeneous arrangement of large and small particles and the corresponding geometric parameters are shown. A similar correlation between the material properties and the average number of particle contacts as in the case of homogeneous arrangement was observed. In the inhomogeneous arrangement, an increase in Young's modulus and thermal conductivity for large size ratios can be seen (Fig. 4.6d). This was attributed to the load-bearing capability of the spatial structure shown in Fig. 3.10b, which was enhanced by the volume increase and the corresponding increase of contact area between the large particles at the edges. The increase of the Young's modulus was correlated to an increase in the squared solid chord lengths $c_{s,2}$, which was considered reasonable since $c_{s,2}$ was introduced as a measure for the length of force transmission that was very large at the edges of the unit cell. There was a close correlation between thermal conductivity and Young's modulus (Fig. 4.6a and d). Between the MSA and material properties a poor correlation was observed, especially in the homogeneous particle arrangement (Fig. 4.6a and b).

The effect of particles coordination on thermoelastic properties is shown in Fig. 4.7. The symmetry of the unit cell was varied from sc to bcc and fcc for a fixed volume fraction of solid phase of 80% (Fig. 4.7a). Additionally, the same structures have been calculated for a fixed area ratio $a_s = 0.09$ corresponding to a solid volume fraction f_s of 61.5, 76.7 and 80.1% for the sc, bcc and fcc structures, respectively (Fig. 4.7d). The geometric parameters related to these structures are shown in Fig. 4.7b and c, as well as 4.7e and f. Thermoelastic properties decreased when coordination number was increased with constant solid volume fraction (4.7a). This can be explained looking at the area ratio a_s of these structures (Fig. 4.7c), which was drastically decreased by 80% when the coordination number was increased from 6 to 12. In Fig. 4.7d the thermoelastic properties increased when the coordination number was increased at the same level of a_s . Also the stress concentration factor decreased which demonstrated that stress was distributed more homogeneously in the microstructures with more particles contacts. The increase in coordination number was related to an increase in the auto-correlation parameter for constant volume fractions (Fig. 4.7a and c) and the increase of the constant area ratio was correlated with the increase in the squared solid chord length (Fig. 4.7d and f). Like in case of Fig. 4.6 correlation between minimum solid area and material properties was poor, especially with fixed solid volume fraction f_s (Fig. 4.7a and b).

Random arrangement of particles

The results described above are related to a cubic arrangement of the truncated spheres within the unit cell. Because these type of structures do not give an accurate image of real structures, a random arrangement of the spheres is considered.

In Fig. 4.8 the solid volume fraction f_s was 70% and the contact area ratio a_s was about 0.09, but the coordination number (Fig. 4.8a), particle displacement (Fig. 4.8b) and particle size ratio (Fig. 4.8c) were changed. Each point in Fig. 4.8 represents the mean value of 10 independent runs for different random structures obtained with the

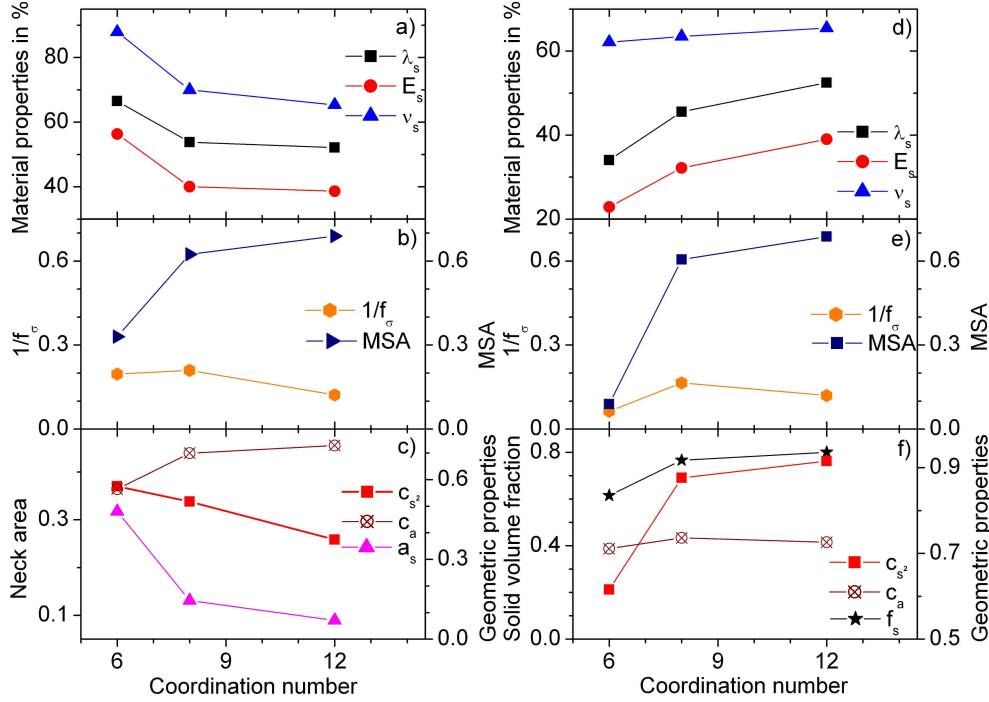


Figure 4.7: Properties of cubic structures at different number of nearest neighbors: (a) scaled thermal conductivity λ_s , Young's modulus E_s and Poisson's ratio ν_s for constant solid volume fraction 80%, (b) related inverse stress concentration factor $1/f_\sigma$ and minimum solid area MSA, (c) related contacts per particle N/n , average squared solid chord length c_{s^2} , auto-correlation parameter c_a and ratio of total contact area and total interface area a_s , (d) material properties for particles with constant scaled contact area $a_s = 0.09$ at different solid volume fractions f_s , (e) related inverse stress concentration factor and MSA and (f) related geometric properties

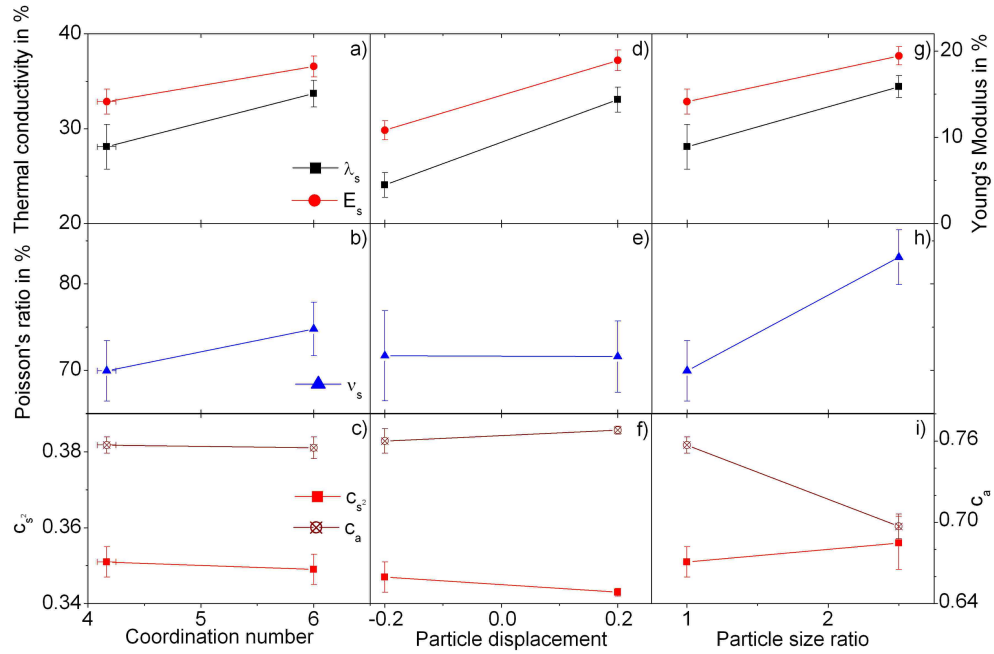


Figure 4.8: Properties resulting from random arrangement of truncated spheres (solid volume fraction 70% and scaled contact area $a_s = 0.09$): (a) scaled thermal conductivity λ_s and Young's modulus E_s , (b) scaled Poisson's ratio ν_s , (c) average squared solid chord length c_{s^2} and auto-correlation parameter c_a for different coordination number, (d-f) corresponding quantities for different particle displacement, (g-i) corresponding quantities for different particle size ratios

same boundary conditions. The error bars indicate uncertainty derived from statistical spread of results from different simulation runs. From Fig. 4.8a and b it can be seen that the thermoelastic properties increased with increasing coordination number. The result is consistent with the simulation result in case of the cubic structures if the area ratio was fixed (see Fig. 4.7d). A particle displacement to the center of the unit cell caused an increase and an outward displacement a decrease of the thermal conductivity and Young's modulus (Fig. 4.8d). This was attributed to a more efficient formation of a load-bearing frame by concentrating the spheres in the center compared to the less dense distribution on the surface of the unit cell. When the particles size increased an increase of the material properties was also observed. This could be explained by the improvement of the heat transfer and force transmission within the large spheres, which lead to higher temperature gradients and stresses at the particle contacts. Minimum solid area was not determined for the random structures. The other geometric properties that were calculated from chord length analysis did not show a clear correlation to the thermoelastic properties.

Conclusions

Different particle shapes allow for an independent variation of contact area and solid volume fraction and offer much more flexibility in modeling of microstructures than the widely used truncated spheres. For this reason additional particle shapes and arrangements were used to simulate porous ceramics. It was shown that phenomena related to particle arrangement could be simulated in cubic unit cells. These models were proposed to understand the effects which contribute to microstructure property relations.

Random structures have the advantage to reproduce the disorder of the real structures. It has been shown that they offer more flexibility to control simultaneously geometric parameters like solid volume fraction, contact area and coordination number than cubic structures. This makes them more appropriate to investigate the influence of one microstructure parameter without unwillingly changing other parameters. However, the use of random structures without such control has the disadvantage that interpretation of results is difficult, compared to cubic structures. Another disadvantage of the random microstructures was the computational effort, which was two or three order of magnitudes larger than for cubic structures.

Thermal conductivity and Young's modulus were closely correlated in all porous compacts investigated in the present study. Parameters like coordination number, particle size distribution and shape, agglomeration, pore volume and contact area affected both properties similarly. The largest changes were caused by the contact area between the particles. Therefore, in comparing porous ceramics with different microstructures, thermal conductivity as well as Young's modulus are a good measure for changes in contact area. Together with the measurement of total pore volume they can provide a valuable complement to ceramographic methods. Although the Young's modulus shows the same trend as the thermal conductivity, the scaled Young's moduli were always smaller by 20 – 50% than the respective scaled thermal conductivities. This was attributed to the larger capability of heat flux to bypass thermal barriers compared to force transmission, which is most efficient along straight lines. Microstructure parameters which were

determined in the present study by chord length and minimum solid area analysis, i. e. squared chord lengths, auto-correlation etc., did not show unambiguous correlation to the changes of thermoelastic properties. Some of the phenomena could not be correlated to a specific parameter; the unambiguous interpretation was obscured by other parameters, like number of particle contacts and size distribution.

Although the present results are considered helpful in understanding some basic relations between microstructure phenomena and material properties, the formation of the microstructures was not considered.

4.2.2 Microstructure-property relations in real structures

The microstructures studied in the previous section were used in order to understand the principal effects in porous structures. In the following we will concentrate on real structures, e.g. two types of ceramics, a porous and a bi-continuous system. The simulations of effective material properties are focused on aluminium oxide (Al_2O_3) and on zirconia-alumina composites.

Aluminium oxide ceramic

The microstructures of the sintered Al_2O_3 ceramic are presented in Chapter 3, section 3.3.2 (see Fig. 3.20). As mentioned, the scanning electron micrographs were evaluated using the mean intercept length technique. Fig. 4.9 shows some geometrical properties derived from image analysis of the experimental samples. The same properties obtained from the theoretical structure after fitting the model to the experimental data are also presented in Fig. 4.9. Fig. 4.9a shows the interfaces between Al_2O_3 grains for both,

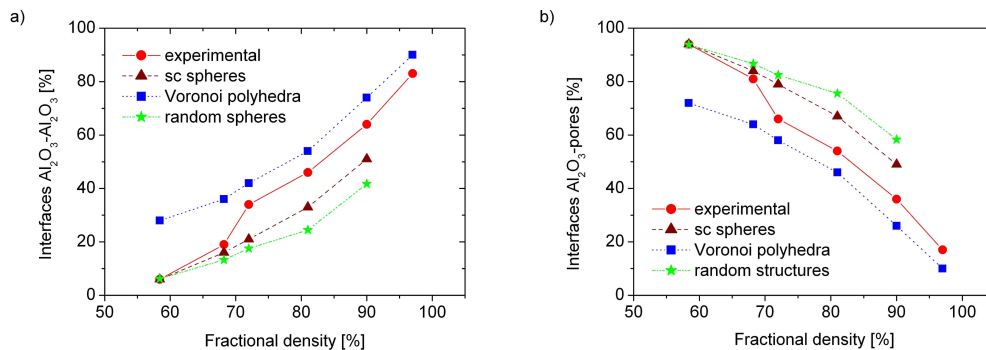


Figure 4.9: Geometrical properties of microstructures derived from experimental and model structures: (a) interfaces between Al_2O_3 particles, (b) interfaces between Al_2O_3 and pores

experimental and simulated structures. The particle interfaces were determined for the truncated spheres as well as for Voronoi model. In case of truncated spheres, a simple cubic (sc) as well as a random arrangement of particles within the unit cell was considered. Fig. 4.9b represents the same comparison for the interfaces between Al_2O_3

grains and pores. It can be seen that the experimental values are always lying in-between the theoretical values of the three models.

A combination of FEM simulations for the thermal conductivity and the experimental data for Al_2O_3 samples are presented in Fig. 4.10. It is well known that the thermal conductivity in a real crystal is influenced by the phonon-phonon interactions and by phonon interactions with impurities and/or imperfections of lattice (see Chapter 2, section 2.1.3). Grain boundaries in polycrystalline material will act as scattering sites and, hence, decrease the thermal conductivity. At the grain boundaries there is a change of the crystallite orientation, therefore in an anisotropic crystal this leads to a change in the velocity of the phonons in the direction of the heat flow. The grain boundaries are a disordered region which also leads to a local change of phonon velocity. Both aspects are important and must be considered, but Klemens [Kle94] has deduced that the latter one is more significant. Looking at earlier work concerning the role of grain boundaries on the thermal conductivity of single phase materials some contradictions can be observed. Berman [Ber52] has compared the difference between thermal conductivity of a single crystal sapphire and sintered alumina. It was shown that the polycrystalline material has a thermal conductivity which decreases from intrinsic behavior by a factor > 50 when the temperature is < 50 K. As the temperature increases (> 100 K) the divergence rapidly diminished and the mean free path is controlled by phonon-phonon scattering. Charvat and Kingery [Cha57] have investigated a dense alumina ceramic with different average grain sizes (9 and 17 μm) above 300 °C and have concluded that the influence of the grain boundaries is negligible in this temperature range, because the mean free path of phonons is much smaller than the grain size. The work of Smith et al [Fay00] on more conductive oxides (tin oxide) demonstrate the contrary. They reported for the thermal resistance of the grain boundaries a value of 0.04 $\text{mm}^2\text{K}/\text{W}$ at 300 K. From the literature a typical value for the thermal boundary resistance of 0.01 – 0.1 $\text{mm}^2\text{K}/\text{W}$ is suggested. But is not expected that all materials will have the same values.

In this work the influence of grain boundaries on heat transfer was taken into account according to the results of Smith et al [Smi03]. By comparison of various sintered alumina ceramics with different grain sizes they found that the average thermal resistance of a grain boundary in dense alumina at room temperature is ≈ 0.010 $\text{mm}^2\text{K}/\text{W}$. In partially sintered porous alumina a slightly higher value of 0.022 $\text{mm}^2\text{K}/\text{W}$ was observed. Therefore in the present simulations two values have been used for thermal boundary resistance (TBR): 0.01 and 0.02 $\text{mm}^2\text{K}/\text{W}$. The results of the calculated thermal conductivity for Voronoi polyhedra and truncated spheres are depicted in Fig. 4.10a and 4.10b, respectively. The graph shows that the experimental values are in the range of the simulated one for the applied TBRs. It can be observed that for Voronoi structures (Fig. 4.10a) at small and high densities the experimental and simulated data agree well. For the region in-between, the higher the values of TBRs (TBR = 0.01 and TBR = 0.02 $\text{mm}^2\text{K}/\text{W}$) the smaller the thermal conductivity values. The same tendency can be seen in case of sc truncated spheres (Fig. 4.10b). Here the simulation for the 97% density could not be performed because of geometry constrains reasons. As expected the curve which indicates the calculated conductivities for a very small TBR are situated above experimental data (the values being much larger).

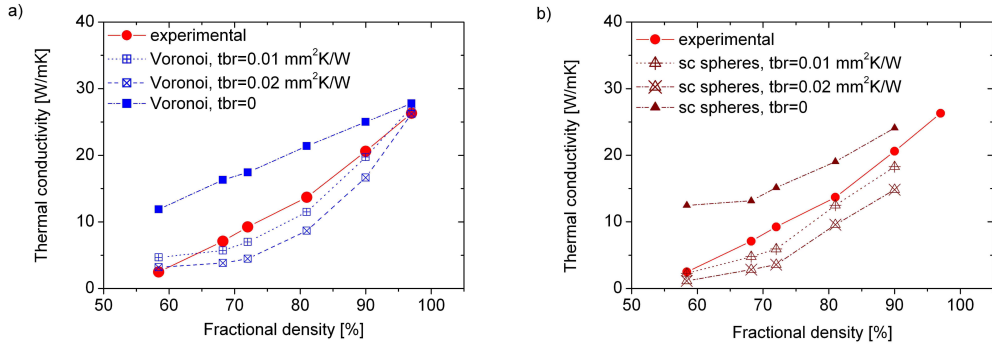


Figure 4.10: Experimental and simulated thermal conductivity of Al_2O_3 ceramic using different thermal boundary resistances: (a) Voronoi model, (b) sc truncated spheres

In Fig. 4.11a the Al_2O_3 grains as deduced from the experimental structures are presented. As the sintering temperature increases (and hence the Al_2O_3 volume fraction),

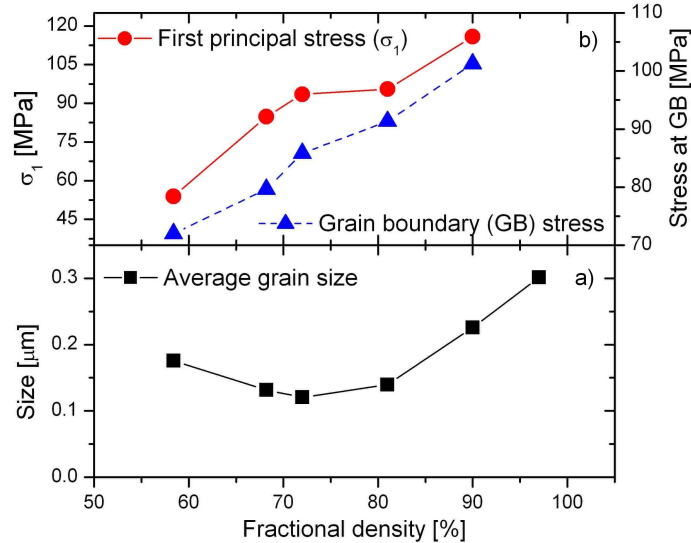


Figure 4.11: (a) Al_2O_3 grains and (b) first principal stress (σ_1) in Al_2O_3 and the stress at Al_2O_3 grain boundaries

the grains becomes larger. It can be observed that the first two values in Fig. 4.11a are too high. This can be explained looking at the SEM pictures of Al_2O_3 samples (compare Fig. 3.20a and 3.20b). In both cases the boundaries between Al_2O_3 grains are not visible. Therefore it is possible that the quantitative image analysis is erroneous because some of the grains were not considered. In Fig. 4.11b the first principal stress (σ_1) as a function of Al_2O_3 volume fraction is presented. The stress was calculated by cooling the system from the following temperatures: 750, 1100, 1130, 1170, 1250 and 1270 °C (where a stress free state was considered) to room temperature. The anisotropy

of the thermal expansion coefficient for the Al_2O_3 was taken into account: $\alpha_a = 8.62$ and $\alpha_c = 9.38 \times 10^{-6}/\text{K}$ [Mer62]. As expected the stresses increase as the sintering temperature increases. Fig. 4.11b illustrates also the stresses calculated at Al_2O_3 grain boundaries. This was possible by using contact and target elements for meshing the contact areas. The same tendency as for the first principal stress is observed, namely the stress at grain boundaries increases with higher density.

It was already mentioned that the different grain sizes influence the thermal conductivity, i.e. the smaller the grains (that means the larger the number of grain boundaries) in a structure, the lower the value of thermal conductivity. Looking at the simulation results (see Fig. 4.10a and b) and considering this effect it can be concluded that the thermal conductivity slope will increase. So, a better agreement with experimental work is obtained. That means, for small density the values of thermal conductivity calculated for $\text{TBR} = 0.01 \text{ mm}^2\text{K}/\text{W}$ will be in better agreement with experimental data as the one calculated for $\text{TBR} = 0.02 \text{ mm}^2\text{K}/\text{W}$. The same conclusion can be drawn for the stress influences. Taking into account that the stress will lower the thermal conductivity at high fractional densities, it can be observed that the slope will decrease, which means that a poor agreement between experiment and simulations is obtained.

Besides thermal properties also elastic moduli of Al_2O_3 ceramic have been calculated. Fig. 4.12 shows the comparison between experimental and simulated Young's moduli. It

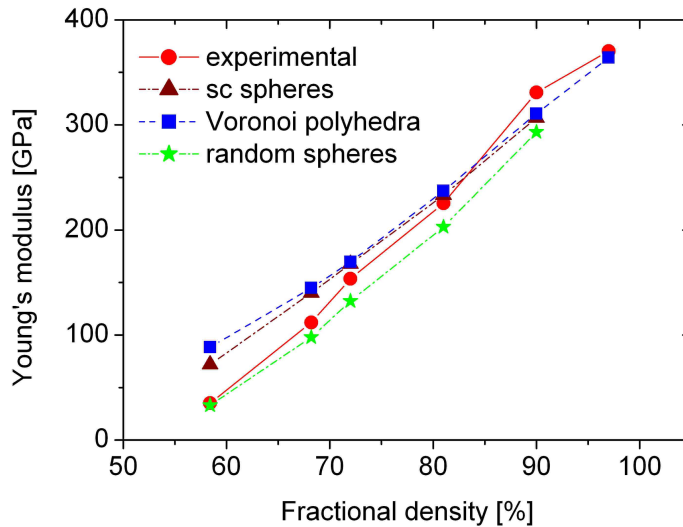


Figure 4.12: Experimental and simulated Young's modulus of Al_2O_3 ceramic using the Voronoi model and truncated spheres in simple cubic and random arrangement

can be recognized that the simulated Young's moduli are in good agreement with the experimental data for fractional densities larger than 70% when the Voronoi model is used. For a small Al_2O_3 volume fraction ($< 70\%$) a better agreement between experimental and simulated Young's moduli can be achieved by using a random arrangement of the truncated spheres instead of the simple cubic arrangement. In order to obtain a high

volume fraction (high density), for the random arrangement of the truncated spheres, the overlap of three and four spheres was allowed. It can be observed that for the case of simple cubic structures a higher Young's modulus obtained in the simulations. This can be explained on the basis of the load bearing capability of simple cubic structures due to the force transmission, which is most efficient along straight lines. In case of random arrangement of truncated spheres the force transmission is no more along a straight line, therefore the structures will have a lower Young's modulus.

Conclusions

The microstructure of porous Al_2O_3 could be adequately described in terms of interface areas and grain sizes. In the beginning stage of sintering the truncated spheres model describes better the microstructure, while, in the final stage, Voronoi polyhedra are more close to the real microstructures (see Fig. 3.20).

Comparing the experimental and simulated values of Young's modulus a good agreement can be seen (Fig. 4.12). In case of low Al_2O_3 volume fractions the agreement between experimental and simulated values was better for random arrangement of truncated spheres, because the force transmission is in this case not so efficient, as in case of simple cubic arrangement (along straight lines).

For the thermal conductivity the consideration of thermal boundary resistance was necessary. In this case the simulated and experimental values are in good agreement. It can be seen that for different values of thermal boundary resistance the thermal conductivities lie within the experimental data (see Fig. 4.10). Taking into account the effect of grain growth (see Fig. 4.11a), the slope of the simulated curve will increase, that means the experimental and simulated values will be in a better agreement. Therefore it can be concluded that a constant value of TBR can be used to describe adequately the thermal behavior of all Al_2O_3 microstructures.

Zirconia-alumina ceramic

The microstructures of the ZA ceramic are presented in section 3.3.2 (see Fig. 3.21). The scanning electron micrographs were evaluated using the mean intercept length technique and different geometrical properties could be derived.

Fig. 4.13 shows the different types of interface areas between grains. The grain boundaries were calculated for both experimental and theoretical microstructures and compared. The experimental and simulated results agree very well and thus the structures could be accurately represented in terms of interface areas. In Fig. 4.14 the ratios between the mean chord lengths of Al_2O_3 and ZrO_2 grains are illustrated. It can be observed that the experimental and simulated data are in good agreement except for the larger Al_2O_3 volume fractions. Concerning the volume fraction, the theoretical structures were always varied to fit to experimental ones within 0.1%. For the ZA ceramics only the Voronoi model was employed for simulations, as the microstructures can be better described by the Voronoi polyhedra than the truncated spheres (see Fig. 3.21).

In the following the thermal and mechanical properties of the ZA ceramics are presented. Thermal conductivity and Young's modulus were calculated using the bulk

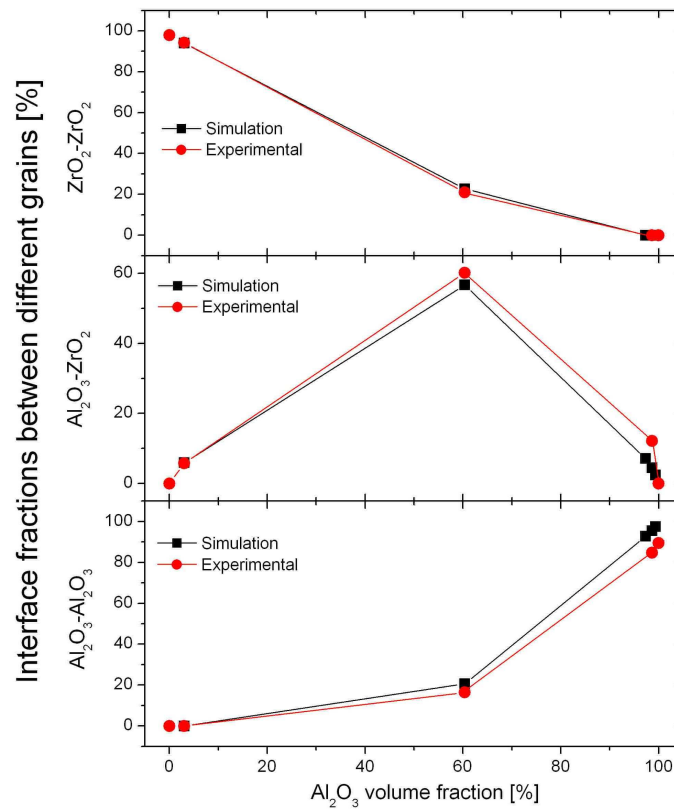


Figure 4.13: Geometrical properties of microstructures derived from experimental and model structures: (a) interfaces between Al_2O_3 grains, (b) interfaces between Al_2O_3 and ZrO_2 grains, (c) interfaces between ZrO_2 grains

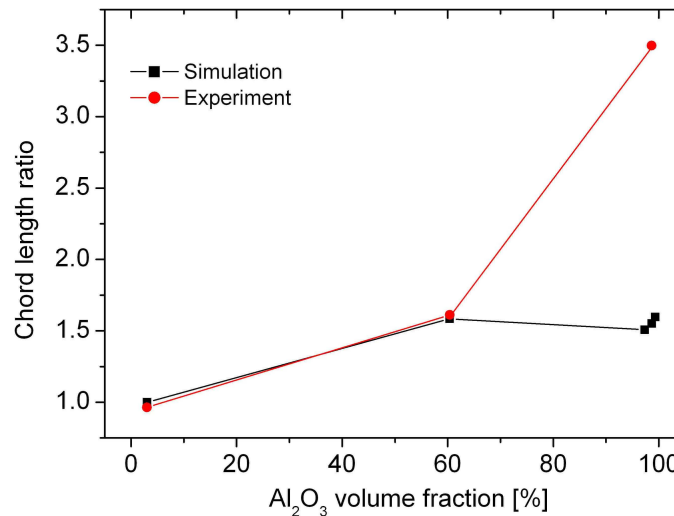


Figure 4.14: Ratio of mean chord lengths between Al_2O_3 and ZrO_2 grains

properties from Table 3.3. The simulated values were then scaled, i.e. the difference ($P_{sim} - P_{exp}$) calculated for 100% Al_2O_3 was added to every simulated value. Fig. 4.15 shows the comparison of both simulated properties with measured data. A good agree-

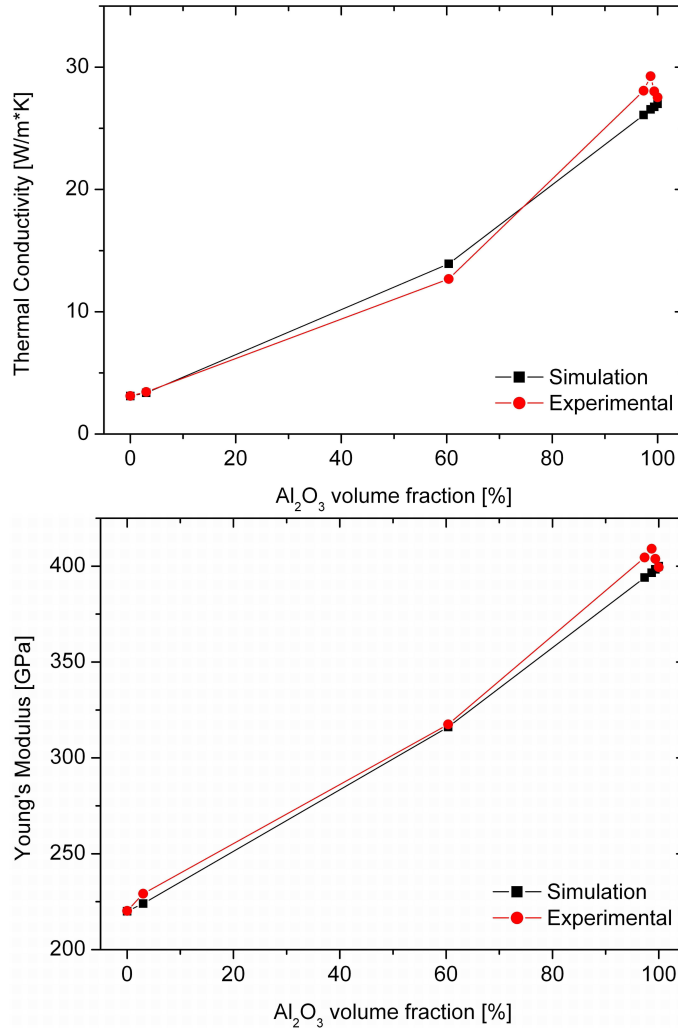


Figure 4.15: Thermal conductivity and Young's modulus for ZA ceramic

ment between experimental and simulated results is observed for both properties (thermal conductivity and Young's modulus), except for higher volume fractions of Al_2O_3 where a large discrepancy is observed (see the zoom on every picture). Therefore an explanation of the differences between experiment and theory data will be given in the next paragraphs.

Effect of stresses on thermoelastic properties of zirconia-alumina ceramic

It is well known that the tetragonal to monoclinic (t-m) crystallographic transformation, which is a natural polymorphism in zirconia, increase the fracture toughness of the material. The phenomenon is based on the volume increase occurring when a zirconia

particle changes the crystallographic cell from tetragonal to monoclinic; in absence of constraints the volume increases by about 5%, but when the transformation is opposed by the surrounding material, stresses build up and they tend to exert a closing pressure. As a normal consequence the zirconia particles with tetragonal symmetry are usually embedded in a suitable matrix. Alumina is a very good candidate, because its high elastic modulus makes it very effective in transmitting the stress to the transformable zirconia. During cooling, the tetragonal to monoclinic transformation of pure ZrO_2 begins at ≈ 1200 °C and proceeds over a wide temperature range (1200 °C to 600 °C) until completion of transformation. Additives like Y_2O_3 , CeO_2 , etc. lower the transformation temperature.

In the present study X-ray diffraction (XRD) has been used to determine the extent of the t-m transformation of zirconia in ZA samples. Only for the 2 wt% ZrO_2 sample this measurement could not be effectuated because the ZrO_2 quantity was too small to be detected. For the other samples, it was found that the largest part of zirconia (95%) remained tetragonal. Classical theory has shown that retention of the tetragonal structure depends on the magnitude of the strain energy arising from the elastic constraints imposed by surrounding material on shape and volume changes associated with the transformation. Constraint can arise from several sources: as an effect of the second-phase matrix and/or as a consequence of the residual stresses which can increase or decrease the strain energy and, thus influence the transformation temperature.

Fig. 4.16 presents the thermoelastic properties for volume fraction of Al_2O_3 higher than 97 vol%. The percentage differences between experimental and simulated data are calculated according to formula, $(P_{sim} - P_{exp})/P_{sim}$, where P_{sim} is the scaled simulated property and P_{exp} is the experimental data for the respective property (see Fig. 4.16a and b). In Fig. 4.16c the percentage change of thermal conductivity and Young's modulus is given. Averaging the ratio of the two values (first the ratio between the percentage change of thermal conductivity and Young's modulus is calculated for every experimental point and then the mean value was calculated) a value about 2.3 was determined. In order to verify the result, the same ratio is calculated in the following using the theory.

According to kinetic theory, thermal conductivity λ is given by Eq. (2.28). However this equation do not show a direct dependence of λ on pressure and therefore the commonly used equation for λ and P is [Tan01]:

$$\lambda(P) = \lambda_0 + \frac{g_0 \lambda_0}{B_0} \cdot P. \quad (4.1)$$

Here g_0 and B_0 are the Bridgeman parameter and bulk modulus, respectively. Subscript 0 stands for properties at normal state. These parameters are known for Al_2O_3 : $g_0 = 5.63$ [Tan01] and $B_0 = 254$ GPa. Using these values the change of thermal conductivity with pressure can be numerically calculated and is:

$$\frac{\partial \lambda}{\partial P} \frac{1}{\lambda_0} = 0.022 \frac{1}{\text{GPa}}$$

The elastic moduli of Al_2O_3 are also influenced by pressure. Duan [Dua99] has calculated the dependence of elastic constants on pressure using ab-initio simulations.

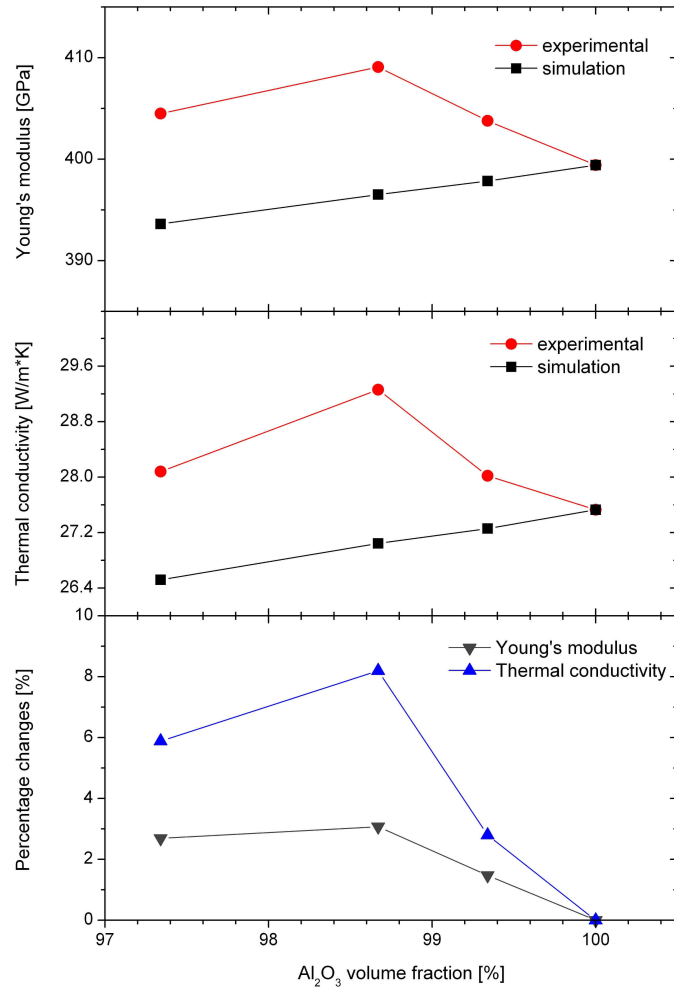


Figure 4.16: Thermal conductivity and Young's modulus for Al_2O_3 volume fractions above 97%

They have found that the change of bulk and shear modulus with pressure are 4.06 and 1.44 respectively. From Eq. (2.22) Young's modulus and its change with pressure could be calculated: $\partial E/\partial P = 3.95$. The dependence of Young's modulus on pressure can be described using a linear equation:

$$E(P) = E_0 + \frac{\partial E}{\partial P} \cdot P, \quad (4.2)$$

where E_0 is the Young's modulus at zero pressure (for Al_2O_3 $E_0 = 390$ GPa). Replacing the numerical values the following value was calculated:

$$\frac{\partial E}{\partial P} \frac{1}{E_0} = 0.010 \frac{1}{\text{GPa}}$$

Now, the ratio between the change of thermal conductivity and change of Young's modulus with pressure could be calculated and a value of approximately 2.2 was derived, which agrees well with the value of 2.3 calculated from experimental data.

Residual stresses in zirconia-alumina ceramic

Components made of alumina/zirconia are usually fired at high temperatures and residual stress results during cooling due to the mismatch in the coefficient of thermal expansion. Alumina shrinks less than zirconia and is in compression. The static equilibrium condition requires that zirconia is in tension. In order to measure these stresses two methods have been used: neutron diffraction [Kra90] and the optical fluorescence technique based on the piezospectroscopic effect [Ma93] and Raman spectroscopy [Ser95a].

In alumina based composites containing ceria-stabilized tetragonal zirconia ($\leq 40\%$) the internal stresses were measured using neutron diffraction by Alexander et al [Ale95]. The average internal stresses for alumina phase were in between -50 MPa and -300 MPa. Sergio et al. [Ser95] have measured the residual stresses in $\text{Al}_2\text{O}_3/\text{Ce-TZP}$ (12 mol% CeO_2) sintered composites containing 10, 20 and 40% zirconia using neutron diffraction and piezospectroscopy technique. The measured stresses in alumina phase are in between -100 MPa and -440 MPa. Using the indirect determination of piezospectroscopic coefficients Tomaszewski et al. [Tom02] have determined the stresses in ceria-stabilized tetragonal zirconia polycrystals. In this case zirconia-alumina composites having 0-90% alumina were measured and hydrostatic stresses between 0 MPa and -650 MPa were obtained. The residual thermoelastic stresses were studied in $\text{Al}_2\text{O}_3\text{-ZrO}_2$ (3.5 mol% Y_2O_3) directionally eutectics (produced via laser floating zone method) using piezospectroscopic effect by Pardo et al. [Par00]. For 34.5 mol% ZrO_2 an average stress of -360 MPa was measured. In this case also the longitudinal (parallel to c-axis of alumina) and transverse stresses (in the alumina basal plane) were determined, and values of -250 MPa and -420 MPa, respectively, have been found.

Further the internal stresses (introduced during post-sintering cooling as a result of the thermal expansion mismatch between alumina and tetragonal-zirconia) are discussed. Thermal expansion mismatch stresses using the properties listed in Table (3.3) were calculated. The simulations are compared with the results derived from an analytical model developed by Hsueh [Hsu86] and Taya [Tay90]. Hsueh used a composite

sphere model to analyze the stresses that develop during sintering due to the presence of heterogeneities. Taya et al. used a modified Eshelby-based model to predict stresses that develop in composites due to thermal stresses. For the case of fully dense composites the appropriate equations which were derived by Hsueh and Taya et al. can be rearranged to yield identical solutions [Ale95]:

$$\sigma_p = \frac{(\alpha_p - \alpha_m)\Delta T}{\left[\frac{1-2\nu_p}{E_p} + \frac{1+2f_s+\nu_m(1-4f_s)}{2E_m(1-f_s)}\right]}, \quad (4.3)$$

where α_p and α_m represent the coefficient of thermal expansion of particles and matrix, respectively. E_p , E_m are the Young's moduli of particles and matrix, and ν_p , ν_m refer to Poisson's ratio of particles and matrix. f_s represents the volume fraction. The average hydrostatic stresses in the matrix are related to those in the particle through the relation $f_s\sigma_p + (1 - f_s)\sigma_m = 0$. The stresses can be modeled using an isolated zirconia particle surrounded by a continuous alumina phase (matrix), or vice-versa (alumina particle is surrounded by zirconia phase) and are reflected in the choice of matrix (m) and particle (p) parameters in Eq. (4.3). The hydrostatic pressures in alumina and zirconia phases are presented in Fig. 4.17. The alumina phase is subjected, as expected, to a

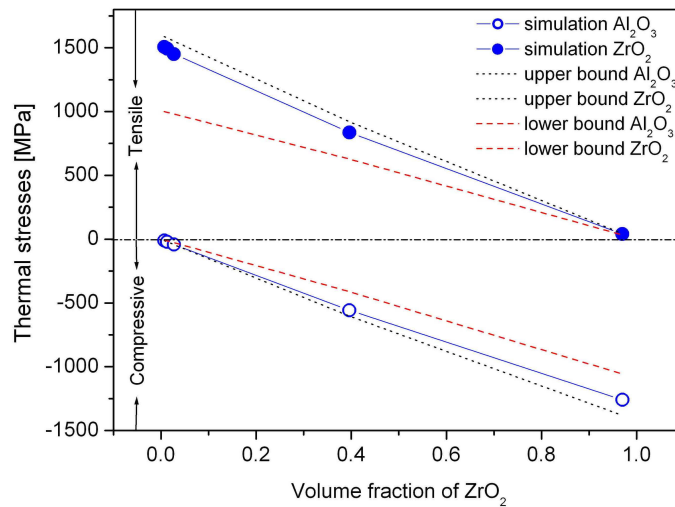


Figure 4.17: Thermal stresses in ZA ceramic simulated and calculated using an analytical formula. The calculated values are obtained from the analysis of Alexander et al. [Ale95]: when zirconia is an isolated phase (p) in alumina matrix (m) yields the lower bound for stress in alumina and the upper bound in zirconia and vice-versa, when alumina (p) is isolated in zirconia phase (m) yields the lower bound for stress in zirconia and the upper bound in alumina

compressive stress because it has the smaller coefficient of thermal expansion (see Table 3.3). Thermal stresses calculated with ANSYS and with Eq. (4.3) agree well and are also in the same range of values as in work presented before.

Calculation of stresses in alumina matrix with a ZrO_2 inclusion

From Fig. 4.16 it can be seen that the maximum in experimental thermal conductivity and Young's modulus deviations from simulated data is at 98.7 Al_2O_3 vol%. For this case, a spherical inclusion of 1.3 ZrO_2 vol% within an alumina matrix was considered. The thermal stresses were calculated, by cooling from a stress free state (1200°C). In Fig. 4.18 one can see the stresses developed in the ZA composite (Fig. 4.18a) as well as the stress in Al_2O_3 matrix due to the spherical inclusion (Fig. 4.18b). It can be seen

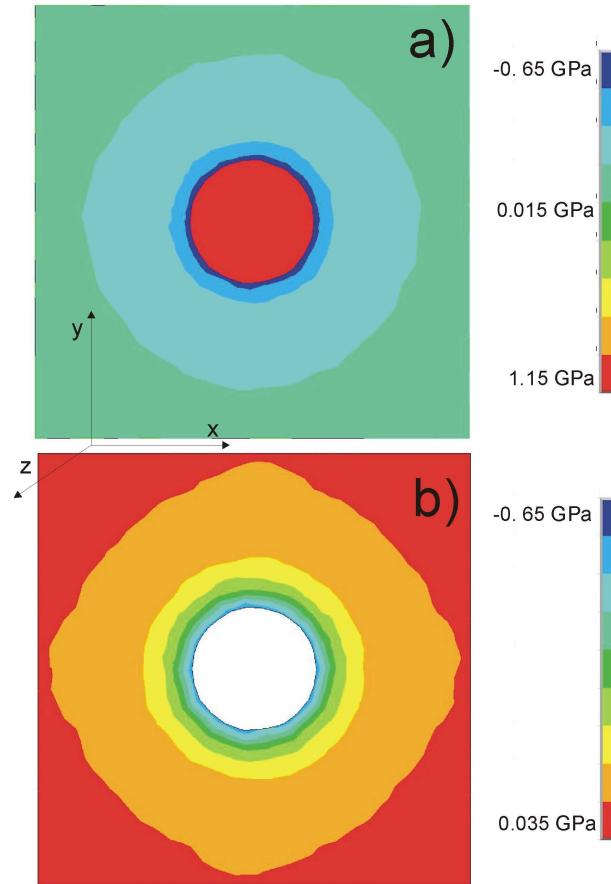


Figure 4.18: Thermal stresses (a) in the ZA composite and (b) around the ZrO_2 inclusion in Al_2O_3 matrix (98.7 vol%). The cube which represent alumina matrix is cut in the middle and the cutting plane is perpendicular on z axis (which points directly into the center of the view window)

that the stress around the spherical inclusion (in the radial direction) is compressive. Considering this distribution of the thermal stresses a further simulation was developed. An anisotropic element with different Young's moduli, Poisson's ratios and shear moduli on x , y and z directions was used. The respective properties in x , y and z directions were calculated by taking into account the effect of pressure on mechanical properties according to Eq. (4.2). The values of the hydrostatic pressure P have been taken from simulation of thermal stresses mentioned above. Finally the overall Young's modulus

and Poisson's ratio were simulated by imposing a displacement in x , y , or z direction. The difference between the Young's modulus calculated before (387 GPa) and the one calculated using the anisotropic distribution of stresses (389 GPa) was small. This indicates that the thermal stresses developed in Al_2O_3 phase during the cooling process are small and cannot explain the differences between the simulation and experimental measurements.

An hypothesis to explain these discrepancies could be that a "latent" pressure develops as a consequence of the untransformed zirconia which exert pressure on the alumina matrix. For this latent pressure a value of 3 GPa was estimated to explain for the difference in experimental and theoretical data. The effects of the pressure and temperature on the tetragonal zirconia have been addressed by a number of authors [Heu85], [Lan82], [Gar85], [Whi62], [Blo85]. By extrapolation of Whitney's pressure-temperature data, was it shown that at a pressure of 3.9 GPa the tetragonal phase of zirconia powder particles is retained at room temperature (see Fig. 4.19).

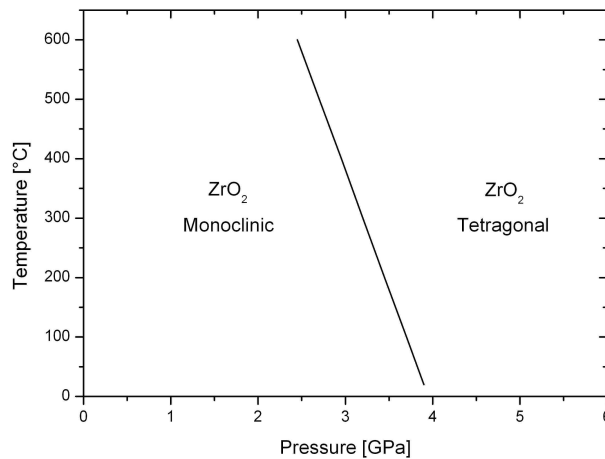


Figure 4.19: Pressure-temperature diagram of pure zirconia. After Block et al. [Blo85]

The pressure at which the tetragonal phase is stable (3.9 GPa) fits to the estimated latent pressure (3 GPa). However the values given in Fig. 4.19 correspond to pure zirconia and not to Y_2O_3 doped zirconia.

Conclusions

For the ZA composite the Voronoi polyhedra model offer a good description of the microstructure in terms of grain boundaries and grain sizes. The thermal conductivity and Young's modulus were numerically predicted using values reported in the literature as properties for the individual phases. The simulated properties have been compared with the measurements and, in general, a good agreement could be observed.

For 1 to 4 wt% ZrO_2 , larger differences between simulated and experimental values were observed. The discrepancies have been explained by taking into account the effect of pressure on ZA microstructures. Along this lines, the thermal stresses resulting from the cooling process were calculated and compared with other experimental work. The

simulation of the average stresses for both phases (alumina and zirconia) performed in the present study agree well with experimental data from other work.

The local anisotropy of the thermal stresses near a spherical zirconia inclusion in the alumina matrix was considered. The Young's modulus was calculated for this case but the value obtained was too small and did not agree with experimental data.

Taking into account the linear dependence of the thermomechanical properties on the pressure, it has been shown that the amount of the stress developed in microstructures was insufficient to explain the discrepancies between experimental and simulated thermoelastic properties.

In order to determine the causes for the large values of thermal conductivity and Young's modulus at high Al_2O_3 volume fractions, further work is in progress. New ZA samples, where the contain of ZrO_2 was varied from 0.01 to 1 wt% in small steps, have been produced. Also the contain of Y_2O_3 in ZrO_2 has been changed from 3 mol% to 8 mol% to obtain stable cubic zirconia without a phase transformation. Thermal stresses in all samples will be measured using the cathodoluminescence spectroscopy.

Appendix A

Example of stress calculation on a three-dimensional isoparametric element

Shape functions

Brick (or hexahedral) type linear with 8-node (and quadratic 20-nodes) three-dimensional elements are depicted in Figure A.1. The geometry and displacement field of elements are specified in parametric form and are interpolated with the same functions. Shape function used for interpolation are polynomials of the local coordinates ξ , η and ζ ($-1 \leq \xi, \eta, \zeta \leq 1$).

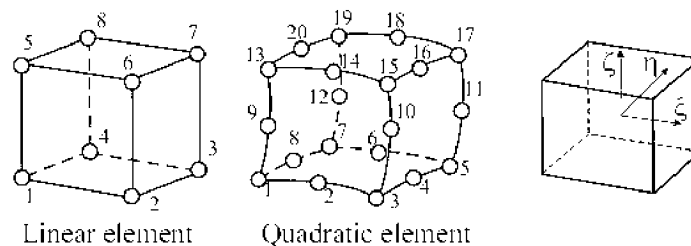


Figure A.1: Linear and quadratic three-dimensional finite element and their representation in the local coordinate system

Both, coordinates and displacements, are interpolated with the same shape function:

$$\begin{aligned}
 \{x\} &= [N]\{x^e\} \\
 \{x\} &= \{x \ y \ z\} \\
 \{x^e\} &= \{x_1 \ y_1 \ z_1 \ x_2 \ y_2 \ z_2 \ \dots\}
 \end{aligned}
 \tag{A.1}$$

$$\begin{aligned}
 \{u\} &= [N]\{q\} \\
 \{u\} &= \{u \ v \ w\} \\
 \{q\} &= \{u_1 \ v_1 \ w_1 \ u_2 \ v_2 \ w_2 \ \dots\}
 \end{aligned}
 \tag{A.2}$$

where x, y, z are point coordinates, x_i, y_i, z_i are coordinates of nodes, u, v, w are displacements at point with local coordinates ξ, η, ζ and u_i, v_i, w_i are displacement values at nodes.

The matrix of shape function is:

$$[N] = \begin{bmatrix} N_1 & 0 & 0 & N_2 & 0 & 0 & \dots \\ 0 & N_1 & 0 & 0 & N_2 & 0 & \dots \\ 0 & 0 & N_1 & 0 & 0 & N_2 & \dots \end{bmatrix} \quad (\text{A.3})$$

Shape functions of the linear element are equal to:

$$\begin{aligned} N_i &= \frac{1}{8}(1 + \xi_0)(1 + \eta_0)(1 + \zeta_0) \\ \xi_0 &= \xi\xi_i, \eta_0 = \eta\eta_i, \zeta_0 = \zeta\zeta_i \end{aligned} \quad (\text{A.4})$$

For the quadratic element with 20 nodes the shape functions can be written in the following form:

$$\begin{aligned} N_i &= \frac{1}{8}(1 + \xi_0)(1 + \eta_0)(1 + \zeta_0)(\xi_0 + \eta_0 + \zeta_0 - 2) \text{ vertices} \\ N_i &= \frac{1}{4}(1 - \xi^2)(1 + \eta_0)(1 + \zeta_0), \quad i = 2, 6, 14, 18 \\ N_i &= \frac{1}{4}(1 - \eta^2)(1 + \xi_0)(1 + \zeta_0), \quad i = 4, 8, 16, 20 \\ N_i &= \frac{1}{4}(1 - \zeta^2)(1 + \xi_0)(1 + \eta_0), \quad i = 9, 10, 11, 12 \end{aligned} \quad (\text{A.5})$$

In the above relations ξ_i, η_i, ζ_i are values of local coordinates ξ, η, ζ at nodes.

Strain-displacement matrix

The strain vector $\{\epsilon\}$ contains six different components of the strain tensor:

$$\{\epsilon\} = \{\epsilon_x \epsilon_y \epsilon_z \gamma_{xy} \gamma_{yz} \gamma_{zx}\} \quad (\text{A.6})$$

The strain-displacement matrix for three-dimensional elements has the following appearance:

$$[B] = [D][N] = [B_1 B_2 B_3 \dots] \quad (\text{A.7})$$

$$[B_i] = \begin{bmatrix} \frac{\partial N_i}{\partial x} & 0 & 0 \\ 0 & \frac{\partial N_i}{\partial y} & 0 \\ 0 & 0 & \frac{\partial N_i}{\partial z} \\ \frac{\partial N_i}{\partial y} & \frac{\partial N_i}{\partial x} & 0 \\ 0 & \frac{\partial N_i}{\partial z} & \frac{\partial N_i}{\partial y} \\ \frac{\partial N_i}{\partial z} & 0 & \frac{\partial N_i}{\partial x} \end{bmatrix} \quad (\text{A.8})$$

Derivatives of shape functions with respect to global coordinates are obtained as follows:

$$\left\{ \begin{array}{c} \frac{\partial N_i}{\partial x} \\ \frac{\partial N_i}{\partial y} \\ \frac{\partial N_i}{\partial z} \end{array} \right\} = [J]^{-1} \left\{ \begin{array}{c} \frac{\partial N_i}{\partial \xi} \\ \frac{\partial N_i}{\partial \eta} \\ \frac{\partial N_i}{\partial \zeta} \end{array} \right\} \quad (\text{A.9})$$

where the $[J]$ is the Jacobian matrix and has the following form:

$$[J] = \begin{bmatrix} \frac{\partial x}{\partial \xi} & \frac{\partial y}{\partial \xi} & \frac{\partial z}{\partial \xi} \\ \frac{\partial x}{\partial \eta} & \frac{\partial y}{\partial \eta} & \frac{\partial z}{\partial \eta} \\ \frac{\partial x}{\partial \zeta} & \frac{\partial y}{\partial \zeta} & \frac{\partial z}{\partial \zeta} \end{bmatrix} \quad (\text{A.10})$$

The partial derivatives of x, y, z with respect to ξ, η, ζ are found by differentiation of displacements expressed through shape functions and nodal displacements values:

$$\begin{aligned} \frac{\partial x}{\partial \xi} &= \sum \frac{\partial N_i}{\partial \xi} x_i, & \frac{\partial x}{\partial \eta} &= \sum \frac{\partial N_i}{\partial \eta} x_i, & \frac{\partial x}{\partial \zeta} &= \sum \frac{\partial N_i}{\partial \zeta} x_i \\ \frac{\partial y}{\partial \xi} &= \sum \frac{\partial N_i}{\partial \xi} y_i, & \frac{\partial y}{\partial \eta} &= \sum \frac{\partial N_i}{\partial \eta} y_i, & \frac{\partial y}{\partial \zeta} &= \sum \frac{\partial N_i}{\partial \zeta} y_i \\ \frac{\partial z}{\partial \xi} &= \sum \frac{\partial N_i}{\partial \xi} z_i, & \frac{\partial z}{\partial \eta} &= \sum \frac{\partial N_i}{\partial \eta} z_i, & \frac{\partial z}{\partial \zeta} &= \sum \frac{\partial N_i}{\partial \zeta} z_i \end{aligned} \quad (\text{A.11})$$

The transformation of integrals from the global coordinates system to the local coordinate system is performed with the use of determinant of the Jacobian matrix:

$$dD = dx dy dz = d\xi d\eta d\zeta |J| \quad (\text{A.12})$$

Element properties

Element equilibrium equation has the following form:

$$[k]\{q\} = \{f\}, \text{ where } \{f\} = \{p\} + \{h\} \quad (\text{A.13})$$

Element matrices and vectors are:

- stiffness matrix

$$[k] = \int_D [B]^T [E] [B] dD \quad (\text{A.14})$$

- force vector (volume and surface load)

$$\{p\} = \int_D [N]^T \{p^D\} dD + \int_S [N]^T \{p^S\} dS \quad (\text{A.15})$$

- thermal vector (fictitious forces to simulate thermal expansion)

$$\{h\} = \int_D [B]^T [E] \{\epsilon^T\} dD \quad (\text{A.16})$$

where $[E]$ is the elasticity matrix (see Eq. (2.8)).

Computation of the stiffness matrix

Calculation of the element stiffness matrix by multiplication of the three matrices involves many arithmetic operations with zeros. After performing multiplications in closed form, coefficients of the element stiffness matrix $[k]$ can be expressed as follows:

$$\begin{aligned} k_{ii}^{mn} &= \int_D \left[\beta \frac{\partial N_m}{\partial x_i} \frac{\partial N_n}{\partial x_i} + \mu \left(\frac{\partial N_m}{\partial x_{i+1}} \frac{\partial N_n}{\partial x_{i+1}} + \frac{\partial N_m}{\partial x_{i+2}} \frac{\partial N_n}{\partial x_{i+2}} \right) \right] dD \\ k_{ii}^{mn} &= \int_D \left(\lambda \frac{\partial N_m}{\partial x_i} \frac{\partial N_n}{\partial x_j} + \mu \frac{\partial N_m}{\partial x_j} \frac{\partial N_n}{\partial x_i} \right) \\ \beta &= \lambda + 2\mu \end{aligned} \quad (\text{A.17})$$

where m, n are local node numbers; i, j are indices related to coordinate axes (x_1, x_2, x_3). Cyclic rule is employed in the above equation if coordinate indices become greater than 3.

Integration of the stiffness matrix for three-dimensional elements is carried out in the local coordinate system ξ, η, ζ :

$$[k] = \int_{-1}^1 \int_{-1}^1 \int_{-1}^1 [B(\xi, \eta, \zeta)]^T [E] [B(\xi, \eta, \zeta)] |J| d\xi d\eta d\zeta \quad (\text{A.18})$$

Three-time application of the one-dimensional Gauss quadrature rule leads to the following numerical integration procedure:

$$I = \int_{-1}^1 \int_{-1}^1 \int_{-1}^1 f(\xi, \eta, \zeta) d\xi d\eta d\zeta = \sum_{i=1}^n \sum_{j=1}^n \sum_{k=1}^n f(\xi_i, \eta_j, \zeta_k) w_i w_j w_k \quad (\text{A.19})$$

Usually $2 \times 2 \times 2$ integration is used for linear elements and integration $3 \times 3 \times 3$ is applied to the evaluation of the stiffness matrix for quadratic elements. For more efficient integration, a special 14-point Gauss-type rule exists, which provides sufficient precision of integration for three-dimensional quadratic elements.

Calculation of strains and stresses

After computing matrices and vectors, the assembly process is used to compose the global equation system. Solution of the global equation system provides displacements at nodes of the finite element model. Using disassembly, nodal displacement for each element can be obtained.

Strains inside an element are determined with the use of the displacement differentiation matrix:

$$\{\epsilon\} = [B]\{q\} \quad (\text{A.20})$$

Stresses are calculated with the Hook's law (Eq. 2.8). The displacement gradients (and hence strains and stresses) have quite difference precision at different point inside finite elements. The highest precision for displacement gradients are at the geometric center for the linear element and at reduced integration points $2 \times 2 \times 2$ for the quadratic hexagonal element.

For quadratic elements, displacement derivatives have best precision at $2 \times 2 \times 2$ integration points with local coordinates $\xi, \eta, \zeta = \pm 1/\sqrt{3}$. In order to build a continuous field of strains or stresses, it is necessary to extrapolate results values from $2 \times 2 \times 2$ integration points to vertices of 20-node element (numbering of integration points and vertices is shown in Fig. A.1).

Results are calculated at 8 integration points, and trilinear extrapolation in the local coordinate system ξ, η, ζ is used:

$$f_i = L_{i(m)} f_{(m)} \quad (\text{A.21})$$

where $f_{(m)}$ are known function values at reduces integration points; f_i are function values at vertex nodes and $L_{i(m)}$ is the symmetric extrapolation matrix:

$$L_{i(m)} = \begin{bmatrix} A & B & C & B & B & C & D & C \\ & A & B & C & C & B & C & D \\ & & A & B & D & C & B & C \\ & & & A & C & D & C & B \\ & & & & A & B & C & B \\ & & & & & A & B & C \\ & & & & & & A & B \\ & & & & & & & A \end{bmatrix} \quad (\text{A.22})$$

$$A = \frac{5 + \sqrt{3}}{4}, \quad B = -\frac{\sqrt{3} + 1}{4}, \quad C = \frac{\sqrt{3} - 1}{4}, \quad D = \frac{5 - \sqrt{3}}{4}$$

Stresses are extrapolated from integration points to all nodes of elements. Values for midside nodes can be calculated as an average between values for two vertex nodal values. Then averaging of contributions from the neighboring finite element is performed for all nodes of the finite element model. Averaging produces a continuous field of secondary results specified at nodes of the model with quadratic variation inside finite elements. Later, the results can be interpolated to any point inside element or on its surface using quadratic shape functions.

Bibliography

- [Ale95] K.B. Alexander, P.F. Becher, X.-L. Wang, C.-H. Hsueh, *Internal Stresses and the Martensite Start Temperature in Alumina-Zirconia Composite: Effects of Composition Microstructure*, J. Am. Ceram. Soc. **78** (1995) 291-296
- [Ang93] R.J. Angel, *The High-Pressure, High-Temperature Equation of State of Calcium Fluoride, CaF₂*, J. Phys.: Condens. Matter **5** (1993) L141-L144
- [Arl00] T. Arlt, M. Bermejo, M.A. Blanco, L. Gerward, J.Z. Jiang, J. Staun Olsen, J. M. Recio, *High-Pressure Polymorphs of Anatase TiO₂*, Phys. Rev. B **61** (2000) 14414-14419
- [Ash71] N.W. Ashcroft, N.D. Mermin, *Solid State Physics*, Holt Saunders International Edition, Buttler and Tanned Ltd., London, 1971
- [Ber52] R. Berman, *The Thermal Conductivity of Some Polycrystalline Solids at Low Temperatures*, Proc. Phys. Soc. London **A65** (1952) 1029-1040
- [Bir52] F. Birch, *Elasticity and Constitution of the Earth Interior*, J. Geophys. Res. **57** (1952) 227-286
- [Bir01] A. Birnboim, T. Olorunyolemi, Y. Carmel, *Calculating the Thermal Conductivity of Heated Powder Compacts*, J. Am. Ceram. Soc. **84** (2001) 1315-1320
- [Bis97] R. Biswas, J.L. Hanshall, R.J. Wakeman, *Finite-Element Modeling of Elastic Stress Distributions in Composite Materials*, Mech. Compos. Mat. Struct. **4** (1997) 233-249
- [Blo85] S. Block, J.H.A. Da Jornada, G.J. Piermarini, *Pressure Temperature Diagram of Zirconia*, J. Am. Ceram. Soc. **68** (1985) 497-499
- [Boc93] A.R. Boccaccini, G. Ondracek, P. Mazilu, D. Windelberg, *On the Effective Young's Modulus of Elasticity for Porous Materials: Microstructure Modelling and Comparison Between Calculation and Experimental Values*, J. Mech. Behaviour Mat. **2** (1993) 119-128
- [Boc94] A.R. Boccacini, *Comment on "Effective Elastic Moduli of Porous Ceramic Materials"*, J. Am. Ceram. Soc. **77** (1994) 2779-2781

- [Boc97] A.R. Boccaccini, Z. Fan, *A New Approach for the Young's Modulus-Porosity Correlation of Ceramic Materials*, *Ceramics International* **23** (1997) 239-245
- [Bra92] K. Brakke, *The Surface Evolver*, *Experimental Mathematics* **1** (1992) 141-165
- [Cat78] C.R.A. Catlow, J.D. Comins, F.A. Germano, R. Tharley, W. Hayes, *Brillouin Scattering and Theoretical Studies of High-Temperature Disorder in Fluorite Crystals*, *J. Phys. C* **11** (1978) 3197-3212
- [Cep80] D.M. Ceperley, B.J. Alder, *Ground State of the Electron Gas by a Stochastic Method*, *Phys. Rev. Lett.* **45** (1980) 566-569
- [Cha57] F.R. Charvat, W.D. Kingery, *Thermal Conductivity: XIII, Effect of Microstructure on Conductivity of Single-Phase Ceramics*, *J. Am. Ceram. Soc.* **40** (1957) 306-315
- [Cha91] S.-C. Chan, Y. Fang, M. Grimsditch, Z. Li, M. Nevitt, W. Robertson, E.S. Zoubolis, *Temperature Dependence of Elastic Moduli of Monoclinic Zirconia*, *J. Am. Ceram. Soc.* **74** (1991) 1742-1744
- [Chu96] Y.C. Chu, S.I. Rokhlin, *Effective Elastic Moduli of Fiber-Matrix Interphases in High-Temperature Composites*, *Metallurgical and Materials Transactions* **27a** (1996) 165-182
- [Coo81] R.D. Cook, *Concepts and Application of Finite Element Analysis*, Second Edition, John Wiley and Sons, Inc., New York/Chichester/Brisbane/Toronto/Singapore, 1981
- [Dam78] H. d'Amour, D. Schiferl, W. Denner, H. Schulz, W.B. Holzapfel, *High-Pressure Single-Crystal Structure Determinations for Ruby up to 90 kbar Using an Automatic Diffractometer*, *J. Appl. Phys.* **49** (1978) 4411-4416
- [Dan93] D.P. Dandekar, D.C. Benfanti, *Strength of Titanium Diboride Under Shock Wave Loading*, *J. Appl. Phys.* **73** (1993) 673-679
- [Dea83] E.A. Dean, *Elastic Moduli of Porous Sintered Materials as Modeled by a Variable-Aspect-Ratio-Self-Consistent Oblate-Spheroidal-Inclusion Theory*, *J. Am. Ceram. Soc.* **12** (1983) 847-855
- [Dor84] E. Dörre, H. Hübner, *Alumina - Processing, Properties and Applications*, Material Research and Engineering, Springer-Verlag, 1984
- [Dua99] W. Duan, B.B. Karki, R.M. Wentzcovitch, *High-Pressure Elasticity of Alumina Studied by First Principles*, *Am. Mineralogist* **84** (1999) 1961-1966
- [Exn88] H.E. Exner, (Edit.), H.P. Hougardy, *Quantitative Image Analysis of Microstructures*, Oberursel: DGM Informationsgesellschaft Verlag, 1988

- [Fay00] S. Fayette, D.S. Smith, A. Smith, C. Martin, *Influence of the Grain Size on the Thermal Conductivity of Tin Oxide Ceramics*, J. Eur. Ceram. Soc. **20** (2000) 297-302
- [Foc30] V. Fock, *Näherungsmethoden zur Lösung des Quantenmechanischen Mehrkörperproblems*, Z. Phys. **61** (1930) 126; **62** (1930) 795
- [Gar85] R.C. Garvie, M.V. Swain, *Thermodynamics of the Tetragonal to Monoclinic Phase Transformation in Constrained Zirconia Microcrystals. I-II*, J. Mater. Sci. **20** (1985) 1193-1200, 3479-3486
- [Gel82] B.J. Gellatly, J.L. Finney, *Characterization of Models of Multicomponent Amorphous Metals: The Radical Alternative to the Voronoi Polyhedron*, J. Non-Cryst. Solids **50** (1982) 313-329
- [Ger96] R.M. German, *Sintering, Theory and Practice*, John Wiley & Sons, New York, 1996
- [Got89] T. Goto, O.L. Anderson, I. Ohno, S. Yamamoto, *High-Temperature Elasticity of Corundum*, J. Geophys. Res. **94** (1989) 7588-7602
- [Gou00] O.A. Goussev, P. Richner, M. Rozman, G. Michael, A.A. Gusev, *Void-Containing Materials with Tailored Poisson's Ratio*, J. Appl. Phys. **7** (2000) 4013-4016
- [Gre89] D.J. Green, R.H. Hannink, M.V. Swain, *Transformation Toughening of Ceramics*, CRC Press, Inc. 1989
- [Gri94] M. Grimsditch, E.S. Zouboulis, A. Polian, *Elastic Constants of Boron Nitride*, J. Appl. Phys. **76** (1994) 832-834
- [Gus00] A.A. Gusev, P.J. Hine, I.M. Ward, *Fiber Packing and Elastic Properties of a Transversely Random Unidirectional Glass/Epoxy Composite*, Composites Science and Technology **60** (2000) 535-541
- [Gus01] A.A. Gusev, H.R. Lusti, *Rational Design of Nanocomposites for Barrier Applications*, Advanced Materials **21** (2001) 1641-1643
- [Hah96] O. Hahn, *Models for the Heat Transport in Sintering Ceramic Powder Compacts*, PhD Thesis, University of Würzburg, Germany, 1996
- [Hal76] D.K. Hale, *The Physical Properties and Composite Materials*, J. Mat. Sci. **11** (1976) 2105-2141
- [Har28] D.R. Hartree, Proc. R. Soc. London A **113** (1928) 621
- [Has62] Z. Hashin, S. Shtrikman, *On some Variational Principles in Anisotropic and Nonhomogeneous Elasticity*, J. Mech. Phys. Solids **10** (1962) 335-342

- [Has62a] Z. Hashin, *The Elastic Moduli of Heterogeneous Materials*, J. Appl. Mech. **29** (1962) 143-150
- [Has63] Z. Hashin, S. Shtrikman, *A variational Approach to the Theory of the Elastic Behavior of Multiphase Materials*, J. Mech. Phys. Solids **11** (1963) 127-140
- [Hea84] R.F.S. Hearmon, *Numerical Data and Functional Relationships in Science and Technology*, Landolt-Bornstein, Springer-Verlag, Band 11/Vol. 11, 1984
- [Hed71] L. Hedin, B.I. Lundquist, *Explicit Local Exchange-Correlation Potentials*, J. Phys. C: Solid State Phys. **4** (1971) 2064-2083
- [Heu85] A.H. Heuer, N. Claussen, W.M. Kriven, M. Rühle, *Stability of Tetragonal ZrO₂ Particles in Ceramic Matrices*, J. Am. Ceram. Soc. **65** (1985) 642-650
- [Hil52] R. Hill, *The Elastic Behaviour of a Crystalline Aggregate*, Proc. Phys. Soc. (Lond.) **A65** (1952) 349-355
- [Hil63] R. Hill, *Elastic Properties of Reinforced Solids: Some Theoretical Principles*, J. Mech. Phys. Solids **11** (1963) 357-372
- [Hoh64] P. Hohenberg, W. Kohn, *Inhomogeneous Electron Gas*, Phys. Rev. **136** (1964) B846-B871
- [Hsu86] C.-H. Hsueh, *Sintering Behavior of Powder Compacts with Multiheterogeneities*, J. Mater. Sci. **21** (1986) 2067-2072
- [Isa98] D.G. Isaak, J.D. Carnes, O.L. Anderson, H. Cynn, E. Hake, *Elasticity of TiO₂ Rutile to 1800 K*, Phys. Chem. Minerals **26** (1998) 31-43
- [Jef02] G. Jefferson, G.K. Haritos, R.M. McMeeking, *The Elastic Response of a Cohesive Aggregate - a Discrete Element Model with Coupled Particle Interaction*, J. Mech. Phys. Solids **50** (2002) 2539-2575
- [Kae94] P. Kaeckell, B. Wenzien, F. Bechstedt, *Influence of Atomic Relaxations on the Structural Properties of SiC Polytypes from Ab Initio Calculations*, Phys. Rev. B **50** (1994) 17037-17046
- [Kam97] K. Kamitani, M. Grimsditch, J.C. Nipko, C.-K. Loong, M. Okada, I. Kimura, *The Elastic Constants of Silicon Carbide: A Brillouin-Scattering Study of 4H and 6H SiC Single Crystals*, J. Appl. Phys. **82** (1997) 3152-3154
- [Kar01] V.V. Kartuzov, K.E. Rotmistrovskii, A.V. Stepanenko, V.I. Trefilov, *A Method of Predicting the Elastic Characteristics of Diamond Composites*, Powder Metallurgy and Metal Ceramics, **40** 11-12 (2001) 612-617
- [Kav91] M. Kaviani, *Principles of Heat Transfer in Porous Media*, Mechanical Engineering Series, Springer-Verlag, 1991

- [Kim96] K. Kim, W.R. Lambrecht, B. Segall, *Elastic Constants and Related Properties of Tetrahedrally Bonded BN, AlN, GaN, and InN*, Phys. Rev. B **53** (1996) 16310-16326
- [Kit96] Ch. Kittel, *Einführung in die Festkörperphysik*, 11. Auflage, Oldenbourg Verlag München Wien 1996
- [Kle94] P.G. Klemens, *Phonon Scattering and Thermal Resistance Due to Grain Boundaries*, Int. J. Thermophys. **15** (1994) 1345-1351
- [Koh65] W. Kohn, L.J. Sham, *Self-Consistent Equations Including Exchange and Correlation Effects*, Phys. Rev. **140** (1965) A1133-A1138
- [Kov01] J. Kováčik, *Correlation between Shear Modulus and Porosity in Porous Materials*, J. Mat. Sci. Lett. **20** (2001) 1953-1955
- [Kra90] A.D. Kravitz, T.M. Holden, *The Measurement of Residual Stresses Using Neutron Diffraction*, MRS Bull. **11** (1990) 57-64
- [Kre06] A. Krell, J. Klimke, *Effects of Homogeneity of Particle Coordination on Solid-State Sintering of Transparent Alumina*, J. Am. Ceram. Soc. **89** (2006) 1985-1992
- [Kre96] G. Kresse, J. Furthmüller, *Efficient Iterative Schemes for Ab-Initio Total Energy Calculations Using a Plane-Wave Basis Set*, Phys. Rev. B **54** (1996) 169-186
- [Lan82] F.F. Lange, *Transformation Toughening. I-V*, J. Mater. Sci. **17** (1982) 225-262
- [Ma93] Q. Ma, D.R. Clarke, *Stress Measurement in Single-Crystal and Polycrystalline Ceramics Using Their Optical Fluorescence*, J. Am. Ceram. Soc. **76** (1993) 1433-1440
- [Man69] M.H. Manghni, J. Geophys. Res. **74** (1969) 4317
- [Mar71] B.R. Martin, R. Haynes, *Confirmation of Theoretical Relation between Stiffness and Porosity in Ceramics*, J. Am. Ceram. Soc. **54** (1971) 410-411
- [McN93] L.E. McNeil, M. Grimsditch, R.H. French, *Vibrational Spectroscopy of Aluminium Nitride*, J. Am. Ceram. Soc. **76** (1993) 1132-1136
- [Mer62] K.M. Merz, W.R. Brown, H.P. Kirchner, *Thermal-Expansion Anisotropy of Oxide Solid Solutions*, J. Am. Ceram. Soc. **45** (1962) 531-536
- [Mil88] T. Miloh, Y. Benevise, *A Generalized Self-Consistent Method for the Effective Conductivity of Composites with Ellipsoidal Inclusions and Cracked Bodies*, J. Appl. Phys. **63** (1988) 789-796
- [Mit71] A.R. Mitchell, *Variational Principle and the Finite-Element Method in Partial Differential Equations*, Proc. Roy. Soc. Lond. A **323** (1971) 211-217

- [Mon76] H.J. Monkhorst, J.D. Pack, *Special Points for Brillouin-Zone Integrations*, Phys. Rev. B **13** (1976) 5188-5192
- [Muk98] A.K. Mukhopadhyay, K.K. Phani, *Young's Modulus-Porosity Relations: An Analysis Based on a Minimum Contact Area Model*, J. Mat. Sci. **33** (1998) 69-72
- [Mun01] R.G. Munro, *Effective Medium Theory of the Porosity Dependence of Bulk Moduli*, J. Am. Ceram. Soc. **84** (2001) 1190-1192
- [Nye57] J.F. Nye, *Physical Properties of Crystals*, University Press Oxford, 1957
- [Ond74] G. Ondracek, *Zur Leitfähigkeit von mehrphasigen Werkstoffen - Vergleich zwischen experimentellen und berechneten Werten von Cermets*, Z. f. Werkstofftechnik/J. of Materials Technology **5** (1974) 416-428
- [Och03] A. Öchsner, *Experimentelle und numerische Untersuchung des elastoplastischen Verhaltens zellulärer Modellwerkstoffe*, Fortschritt-Berichte VDI, Reihe 18, Nr. 282, VDI Verlag, Düsseldorf, 2003
- [Pab03] W. Pabst, E. Gregorová, *Derivation of the Simplest Exponential and Power-Law Relations for the Effective Tensile Modulus of Porous Ceramics via Functional Equations*, J. Mat. Sci. Lett. **22** (2003) 1673-1675
- [Par00] J. Pardo, R.I. Merino, V.M. Orera, J.I. Pena, *Piezospectroscopic Study of Residual Stresses in $Al_2O_3 - ZrO_2$ Directionally Solidified Eutectics*, J. Am. Ceram. Soc. **83** 2745-2752
- [Par01] J.S. Park, C.T. Sun, *Micromechanical Modeling of Co-Continuous Ceramic Metal Composites*, Proc. Am. Soc. Composites, 16th Technical Conf. (2001) 123-134
- [Per92] J.P. Perdew, Y. Wang, *Accurate and Simple Analytic Representation of the Electron-Gas Correlation Energy*, Phys. Rev. B **45** (1992) 13244-13249
- [Per96] J.P. Perdew, K. Burke, Y. Wang, *Generalized Gradient Approximation for the Exchange-Correlation Hole of a Many-Electron System*, Phys. Rev. B **54** (1996) 16533 - 16539
- [Per96a] J.P. Perdew, K. Burke, M. Ernzerhof, *Generalized Gradient Approximation Made Simple*, Phys. Rev. Lett. **77** (1996) 3865-3868
- [Pet02] H.E. Pettermann, J.H. Böhm, J. Alcalá, *Normalized Diagrams for Micromechanical Estimates of the Elastic Response of Composite Materials*, Metallurgical and Materials Transactions A **33a** (2002) 3187-3199
- [Pre89] W.H. Press, B.P. Flannery, S.A. Teukolsky, W.T. Vetterling, *Numerical Recipes*, Cambridge University Press, Cambridge 1989

- [Rae98] F. Raether, G. Müller, *Novel Characterization of Process and Product for AlN Ceramics and Correlation with Thermal Conductivity*, International Symposium on Aluminium Nitride Ceramics, Tokyo, 1998
- [Rae98a] F. Raether, R. Hofmann, G. Müller, H.J. Sölter, *A Novel Thermo-Optical Measuring System for the In Situ Study of Sintering Processes*, J. Therm. Anal. 53 (1998) 717-735
- [Ram93] N. Ramakrishnan, V.S. Arunachalam, *Effective Elastic Moduli of Porous Ceramic Materials*, J. Am. Ceram. Soc. **76** (1993) 2745-2752
- [Reu29] A. Reuss, *Berechnung der Fließgrenze von Mischkristallen auf Grund der Plastizitätsbedingung für Einkristalle*, Z. Angew. Math. Mech. **9** (1929) 49-58
- [Ric89] R.W. Rice, *Relation of Tensile Strength-Porosity Effects in Ceramics to Porosity Dependence of Young's Modulus and Fracture Energy, Porosity Character and Grain Size*, Materials Science and Engineering A **112** (1989) 215-224
- [Ric94] R.W. Rice, *Comment on "Effective Elastic Moduli of Porous Ceramic Materials"*, J. Am. Ceram. Soc. **78** (1995) 1711
- [Rob00] A.P. Roberts, E.J. Garboczi, *Elastic Properties of Model Porous Ceramics*, J. Am. Ceram. Soc. **83** (2000) 3041-3048
- [Rob02] A.P. Roberts, E.J. Garboczi, *Elastic Properties of Model Random Three-Dimensional Open-Cell Solids*, J. Mech. Phys. Solids **50** (2002) 33-55
- [Sch98] G.W. Scherer, S. Calas, R. Sempéré, *Densification Kinetics and Structural Evolution During Sintering of Silica Aerogel*, J. Non-Cryst. Sol. **240** (1998) 118
- [Sch26] E. Schrödinger, *Quantisierung als Eigenwertproblem*, Ann. Physik **79** (1926) 361-376 and 489-527
- [Seg02] M.D. Segall, P.L.D. Lindan, M.J. Probert, C.J. Pickard, P.J. Hasnip, S.J. Clark, M.C. Payne, *First-Principles Simulation: Ideas, Illustrations and the CASTEP Code*, J. Phys.: Condens. Matter **14** (2002) 2717-2744
- [Ser95a] V. Sergo, X.-L. Wang, D.R. Clarke, P.F. Becher, *Residual Stresses in Alumina/Ceria-Stabilized Zirconia Composites*, J. Am. Ceram. Soc. **78** (1995) 2213-2214
- [Ser95] V. Sergo, D.R. Clarke, W. Pompe, *Deformation Band in Ceria-Stabilized Tetragonal Zirconia/Alumina: I, Measurement of Internal Stress*, J. Am. Ceram. Soc. **78** (1995) 633-640
- [She01] M.A. Sheikh, S.C. Taylor, D.R. Hayhurst, R. Taylor, *Microstructural Finite-Element Modelling of a Ceramic Matrix Composite to Predict Experimental Measurements of its Macro Thermal Properties*, Modelling Simul. Mater. Sci. **9** (2001) 7-23

- [Sla51] J.C. Slater, *A Simplification of the Hartree-Fock Method*, Phys. Rev. **81** (1951) 385-390
- [Smi03] D.S. Smith, S. Fayette, S. Grandjean, C. Martin, *Thermal Resistance of Grain Boundaries in Alumina Ceramics and Refractories*, J. Am. Ceram. Soc. **86** (2003) 105-111
- [Spo97] P.S. Spoor, J.D. Maynard, M.J. Pan, D.J. Green, J.R. Hellmann, T. Tanaka, *Elastic Constants and Crystal Anisotropy of Titanium Diboride*, Appl. Phys. Lett. **70** (1997) 1959-1961
- [Ste04] G. Steinle-Neumann, R.E. Cohen, *Comment on 'On the Importance of the Free Energy for Elasticity Under Pressure'*, J. Phys.: Condens. Matter **16** (2004) 8783-8786
- [Swa01] V. Swamy, L.S. Dubrovinsky, *Bulk Modulus of Anatase*, J. Phys. Chem. Solids **62** (2001) 673-675
- [Tan01] W. Tang, *A model for Estimation of Thermal Conductivity of Nonmetal Crystals*, J. Phys. Chem. Sol. **62** (2001) 1943-1948
- [Tay90] M. Taya, S. Hayashi, A.S. Kobayashi, H.S. Yoon, *Toughening of a Particulate-Reinforced Ceramic Matrix Composite by Thermal Residual Stresses*, J. Am. Ceram. Soc. **73** (1990) 1382-1391
- [Tob90] J. Tobochnik, D. Laing, G. Wilson, *Random-walk Calculation of Conductivity in Continuum Percolation*, Phys. Rev. A **41** (1990) 3052-58
- [Tom02] H. Tomaszewski, J. Strzeszewski, L. Adamowicz, V. Sergo, *Indirect Determination of the Piezospectroscopic Coefficients of Ceria-Stabilized Tetragonal Zirconia Polycrystals*, J. Am. Ceram. Soc. **85** (2002) 2855-2857
- [Tor91] S. Torquato, *Random Heterogeneous Media: Microstructure and Improved Bounds on Effective Properties*, Appl. Mech. Rev. **44** (1991) 37-46
- [Voi28] W. Voigt, *Lehrbuch der Kristallphysik*, Teubner, Leipzig, 1928; W. Voigt, *Über die Beziehung zwischen den beiden Elastizitätskonstanten isotroper Körper*, Wied. Ann. **38** (1889) 573-587.
- [Wal75] K. Walton, *The Effective Elastic Moduli of Model Sediments*, Geophys. J. R. Astr. Soc **43** (1975) 293-306
- [Wal87] K. Walton, *The Effective Elastic Moduli of a Random Packing of Spheres*, J. Mech. Phys. Solids, **32** (1987) 213-226
- [Whi62] E.D. Whitney, *Effects of Pressure on Monoclinic-Tetragonal Transition of Zirconia; Thermodynamics*, J. Am. Ceram. Soc. **45** (1962) 612-613
- [Zie71] O.C. Zienkiewicz, *The finite Element Method in Engineering Science*, McGraw-Hill, London 1971

List of Figures

1.1	Modeling of materials at different scales	2
2.1	Illustration of (a) bulk modulus, (b) shear modulus, (c) Young's modulus and Poisson's ratio	9
2.2	Thermal expansion can be explained using a typical potential energy. At temperature $T = 0$ K the energy of the system is E_{min} . At finite temperatures the finite energy is $E_{min} + k_B T$ corresponding to an atomic separation between d_2 and d_1 , i.e. d_0 : (a) harmonic potential; (b) anharmonic potential	12
2.3	Schematic representation of a pseudopotential	17
2.4	Principle of FEM	18
2.5	DOFs of various problems	19
2.6	Different element types	19
3.1	Flow diagram of quantum mechanics simulations	22
3.2	Unit cell of Al_2O_3 , CaF_2 , $\alpha - SiC$, TiO_2 rutile, TiO_2 anatase and BN . .	23
3.3	Convergence study for Al_2O_3 and TiO_2 rutile	26
3.4	Flow diagram of microstructure simulation	28
3.5	Simple cubic particles used in the FE simulations: (a) truncated sphere, (b) truncated octahedron and (c) overlapping sphere and cylinders. Grey lines indicate the unit cell	29
3.6	Extreme particle shapes used to describe microstructures with high solid volume fractions and small sintering neck areas: (a) cube with 6 cylindrical contacts and (b) cube with 24 cylindrical contacts	30
3.7	Particles formed by six truncated pyramids based on the sides of an enclosed cube with different opening angles Θ : (a) $\Theta = 60^\circ$ and (b) $\Theta = 120^\circ$	30
3.8	Particles formed by minimizing the interface energy at given ratio between neck radii r and edge length of the unit cell a : (a) $r/a = 0.5$, (b) $r/a = 0.6$, (c) $r/a = 0.7$	31
3.9	Cubic structures with truncated spheres shifted towards (a) the sides and (b) the center of the unit cell. Some particles were removed to get a better view of the microstructure and the contact areas are represented with the dark gray color	32
3.10	Cubic structures with (a) homogeneous and (b) inhomogeneous arrangement of small and large particles	32

3.11	Cubic structures with (a) 8 and (b) 12 nearest neighbors (bcc and fcc structures, respectively)	33
3.12	Random structures with periodic boundaries: (a) truncated spheres and (b) Voronoi polyhedra	34
3.13	Random structure of spherical particles with (a) 4.75 and (b) 7.5 contacts per particle. Here the solid particles are transparent and the contact areas are represented with the grey/red color	34
3.14	(a) The microstructure, (b) the mesh and (c) the temperature field as a result of simulation	36
3.15	Convergence of FE simulations determined by variation of material properties with number of nodes on line segments for simple cubic arrangement of truncated spheres ($f_s = 70\%$): (a) scaled thermal conductivity λ_s and Young's modulus, E_s and (b) inverse stress concentration factor $1/f_\sigma$ and Poisson's ratio ν_s	38
3.16	Convergence of FE simulations as a function of grid refinement, GR for random arrangement of truncated spheres ($f_s = 70\%$): scaled thermal conductivity λ_s and Young's modulus, E_s and Poisson's ratio ν_s	39
3.17	Comparison of material properties calculated by FE model and theoretical small radii solutions (srs): (a) scaled thermal conductivities for sc, bcc and fcc structures and (b) scaled Young's and shear moduli for simple cubic arrangement (srs) equation s from [Kav91], [Wal87], [Wal75]	40
3.18	Microstructure of a ZA ceramic. Parallel lines along the structure is analyzed are indicated with white color. The circles mark the interfaces between alumina and zirconia grains, the segments the interfaces between alumina grains and the filled rhombus the interfaces between zirconia grains	41
3.19	Flow chart describing experimental procedure of samples	42
3.20	Aluminium oxide microstructure at different sintering stages	43
3.21	Microstructure of ZA ceramic with different alumina and zirconia volume fractions	44
4.1	(a) Bulk and (b) shear moduli calculated from elastic constant tensor	49
4.2	(a) Longitudinal and (b) shear anisotropy ratios	50
4.3	Contour maps of: (a) heat flux and (b) first principal stress. Temperature gradient and strain were applied in the z -direction	52
4.4	Material properties of different particle shapes at constant solid volume fraction of 70%: (a) scaled thermal conductivity, (b) scaled Young's modulus, (c) scaled Poisson's ratio, (d) inverse stress concentration factor	53
4.5	Properties of cubic structures at different displacements of truncated spherical particles and constant solid volume fraction 70%: (a) scaled thermal conductivity λ_s , Young's modulus E_s and Poisson's ratio ν_s , (b) related inverse stress concentration factor $1/f_\sigma$ and minimum solid area MSA, (c) contacts per particle N/n , average squared solid chord length c_{s^2} , auto-correlation parameter c_a and ratio between total contact area and total interface area a_s	55

4.6	Properties of cubic structures at different size ratios of truncated spherical particles and constant solid volume fraction 70%: (a) scaled thermal conductivity λ_s , Young's modulus E_s and Poisson's ratio ν_s , (b) related inverse stress concentration factor $1/f_\sigma$ and minimum solid area MSA, (c) contacts per particle N/n , average squared solid chord length c_{s^2} , auto-correlation parameter c_a and ratio between total contact area and total interface area a_s , (d) material properties for particles arranged inhomogeneously, (e) related inverse stress concentration factor and MSA and (f) related geometric properties	56
4.7	Properties of cubic structures at different number of nearest neighbors: (a) scaled thermal conductivity λ_s , Young's modulus E_s and Poisson's ratio ν_s for constant solid volume fraction 80%, (b) related inverse stress concentration factor $1/f_\sigma$ and minimum solid area MSA, (c) related contacts per particle N/n , average squared solid chord length c_{s^2} , auto-correlation parameter c_a and ratio of total contact area and total interface area a_s , (d) material properties for particles with constant scaled contact area $a_s = 0.09$ at different solid volume fractions f_s , (e) related inverse stress concentration factor and MSA and (f) related geometric properties	58
4.8	Properties resulting from random arrangement of truncated spheres (solid volume fraction 70% and scaled contact area $a_s = 0.09$): (a) scaled thermal conductivity λ_s and Young's modulus E_s , (b) scaled Poisson's ratio ν_s , (c) average squared solid chord length c_{s^2} and auto-correlation parameter c_a for different coordination number, (d-f) corresponding quantities for different particle displacement, (g-i) corresponding quantities for different particle size ratios	59
4.9	Geometrical properties of microstructures derived from experimental and model structures: (a) interfaces between Al_2O_3 particles, (b) interfaces between Al_2O_3 and pores	61
4.10	Experimental and simulated thermal conductivity of Al_2O_3 ceramic using different thermal boundary resistances: (a) Voronoi model, (b) sc truncated spheres	63
4.11	(a) Al_2O_3 grains and (b) first principal stress (σ_1) in Al_2O_3 and the stress at Al_2O_3 grain boundaries	63
4.12	Experimental and simulated Young's modulus of Al_2O_3 ceramic using the Voronoi model and truncated spheres in simple cubic and random arrangement	64
4.13	Geometrical properties of microstructures derived from experimental and model structures: (a) interfaces between Al_2O_3 grains, (b) interfaces between Al_2O_3 and ZrO_2 grains, (c) interfaces between ZrO_2 grains	66
4.14	Ratio of mean chord lengths between Al_2O_3 and ZrO_2 grains	66
4.15	Thermal conductivity and Young's modulus for ZA ceramic	67
4.16	Thermal conductivity and Young's modulus for Al_2O_3 volume fractions above 97%	69

4.17	Thermal stresses in ZA ceramic simulated and calculated using an analytical formula. The calculated values are obtained from the analysis of Alexander et al. [Ale95]: when zirconia is an isolated phase (p) in alumina matrix (m) yields the lower bound for stress in alumina and the upper bound in zirconia and vice-versa, when alumina (p) is isolated in zirconia phase (m) yields the lower bound for stress in zirconia and the upper bound in alumina	71
4.18	Thermal stresses (a) in the ZA composite and (b) around the ZrO_2 inclusion in Al_2O_3 matrix (98.7 vol%). The cube which represent alumina matrix is cut in the middle and the cutting plane is perpendicular on z axis (which points directly into the center of the view window)	72
4.19	Pressure-temperature diagram of pure zirconia. After Block et al. [Blo85]	73
A.1	Linear and quadratic three-dimensional finite element and their representation in the local coordinate system	75

List of Tables

3.1	Crystal structures of the studied materials. Space group and lattice parameters are given in the first line for each material; the atomic positions in the following lines	25
3.2	Computational parameters used in simulations for the elastic constants. Given are the k -point sampling for reciprocal space integration, the cutoff energy for the basis set, the type of pseudopotential (PS) used (norm-conserving NC and ultrasoft US) and the range of cell volume for EOS	27
3.3	Experimental data for alumina and zirconia: density ρ , specific heat c_P , thermal conductivity λ , Young's modulus E , Poisson's ratio ν and coefficient of thermal expansion α	46
4.1	Equation of state parameters of the ceramic compounds. The first line of the table gives fit parameters for the computational results for the zero pressure volume (V_0), the bulk modulus (B_0) at this pressure and its pressure derivative (B'). Calculated results (given in the first line of respective material) are compared with experimental equation-of-state parameters (see the second line written with italic characters)	48
4.2	Elastic constants c_{ij} for studied ceramic materials. The first line of every material gives the computed data and the italic characters the experimental ones. The last two columns show the theoretical and experimental bulk and shear modulus	51

Acknowledgements

It is a pleasure for me to thank to the many people who helped me made this thesis possible.

I would like to express my deeply gratitude to my supervisor, **Dr. Friedrich Raether**, for suggesting this topic, his guidance during this work and for always being open to discussions. I have also appreciated all of the valuable time he spent reading and refining this thesis. My gratitude goes also to **Prof. Gerd Müller** for giving me the opportunity to work at Fraunhofer Institut für Silicatforschung (ISC) and for reading and correcting this thesis. I also want to offer my sincere thanks to **Dr. Gerd Steinle-Neumann** for proofreading this thesis and for his help and support concerning the quantum mechanics simulations. I am grateful to **Dr. Jurgen Meinhardt** for introducing me in the world of "Material Studio" and also for his kind assistance.

Many tanks are offered to my colleague **Hans Schömig** for providing the experimental measurements and for patiently answering all my questions about the experimental measurements. I would also like to thank to **Manfred Römer** for providing the scanning electron micrographs of the Al_2O_3 and ZA samples. I owe many tanks to **Alexandra-Maria Trendler** for providing the ZA samples. I am also grateful for her support during times of frustration and stress. For giving me wise advices, reading, correcting and translating manuscripts, helping with various applications, being pleasant talking partner, I wish to give a big thank-you to my colleagues, **Jens Baber**, **Karin Fischer**, **Andreas Klimera** and **Pay Schulze Horn**. A further tank-you to the *Sinterwerkstoffe* group for the nice atmosphere. A special thank to my office colleague and jogging partner, **Anke Dutschke**, for listening my lamentations over the years and for the sincere, pleasant and helpful discussions. For the IT related support provided throughout this years, I would like to thank to **Andreas Boguschewski**. Nevertheless I would like to acknowledge to all the people from the institute who contributed in a way to this thesis.

It is difficult to overstate my gratitude to my friend, Gheorghe Ardelean. He always believed in me, helped me to get through the difficult times and supported me emotionally. For all this and many other things, thank you! Last but not least he helped me proofreading, correcting L^AT_EX styles and adjusting the general layout of the L^AT_EX documents, converting between different graphic file formats, installing various software packages needed to write this work.

Last but not least, I would like to thank my family: my sister, Dori and my parents, whose encouragement and love has never been in doubt. *Vă mulțumesc că ați fost alături de mine mereu!*



This work has been supported financially by Fraunhofer Gesellschaft within the joint project "multiscale modeling". For this assistance I am very grateful.

Curriculum Vitae

Name: Maria Iuga
Date of Birth: August 19th 1973
Place of Birth: Viseu de Sus, Romania
Citizenship: romanian
Marital Status: single

Basic Education:

1979 - 1984 Primary School, "Sc. Generala cu clasele I-X",
Salistea de Sus, Maramures, Romania
1987 - 1991 Theoretical High School "Gheorghe Sincai",
Baia Mare, Romania
June 1991 High School Diploma

Study:

1991 - 1995 Study of Marketing at Spiru Haret University,
Faculty of Economics, Craiova, Romania
1996 - 2000 Study of Physics at University of the West,
Faculty of Physics, Timisoara, Romania
2000 - 2003 Master Degree Study in
Theoretical and Computational Physics,
University of the West, Timisoara, Romania
2001 - 2003 Erasmus - Socrates Scholarship at Friedrich-Alexander
University, Erlangen-Nürnberg, Germany
2002 - 2003 Master Diploma Thesis at Friedrich-Alexander
University, Erlangen-Nürnberg, Germany
2003 - 2006 Doctorate at Bavarian Julius-Maximilians
University Würzburg, Germany

Professional Occupation:

2001 - 2003 Scientific Assistant Student at
Fraunhofer Institut fuer Integrierte Schaltungen,
in Crystal Growth Laboratory, Erlangen, Germany
2003 - present Scientific Assistant at
Fraunhofer Institut für Silicatforschung in Business Unit
Glass and Ceramics - Components and Processing,
Würzburg, Germany

11.02.2007, Würzburg

Erklärung

Hiermit erkläre ich ehrenwörtlich, dass ich die Dissertation "Ab Initio and Finite Element Simulations of Material Properties in Multiphase Ceramics" selbstständig angefertigt und keine anderen als die von mir angegebenen Quellen und Hilfsmittel benutzt habe.

Ich erkläre ausserdem, dass diese Dissertation weder in gleicher oder anderer Form bereits in einem anderen Prüfungsverfahren vorgelegen hat.

Ich habe früher ausser den mit dem Zulassungsgesuch urkundlich vorgelegten Graden keine weiteren akademischen Grade erworben oder zu erwerben versucht.

Wuerzburg, den

.....

(Maria Iuga)